2012-01-01

Investigation Of A Water Desalination Method Via A Humidification-Dehumidification Process Using Hvac Technology

Juan A. Cornejo
University of Texas at El Paso, jcornejo@miners.utep.edu

INVESTIGATION OF A WATER DESALINATION METHOD VIA A HUMIDIFICATION-DEHUMIDIFICATION PROCESS USING HVAC TECHNOLOGY

JUAN ANTONIO CORNEJO

Department of Mechanical Engineering

APPROVED:

Jack A. Dowdy, Ph.D., Chair

Barry A. Benedict, Ph.D.

Arturo Bronson, Ph.D

Anthony J. Tarquin, Ph.D.

Benjamin C. Flores, Ph.D.
Interim Dean of the Graduate School

Dedication

To Dr. Jack Dowdy, Dr. Gary Hawkins, Dr. Art Bronson and my mother Mae:
The four pillars

INVESTIGATION OF A WATER DESALINATION METHOD VIA A HUMIDIFICATION-DEHUMIDIFICATION PROCESS USING HVAC TECHNOLOGY

by

JUAN ANTONIO CORNEJO, B.S.M.E.

THESIS

Presented to the Faculty of the Graduate School of

The University of Texas at El Paso

in Partial Fulfillment

of the Requirements

for the Degree of

MASTER OF SCIENCE

Department of Mechanical Engineering

THE UNIVERSITY OF TEXAS AT EL PASO

August 2012

Acknowledgements

I dedicate this thesis to the many people who contributed in various forms and never lost faith in me. First I thank the Lord for the life, intelligence and for the wonderful individuals who accompanied me on this journey. I proceed to dedicate this work to my mother Mae Valentina Saldaña, whose unending support, maternal love and patience were with me always. Her life is truly an inspiration. This thesis is also dedicated to my close friend and adviser – Dr. Jack A. Dowdy. Words will never express the gratitude I have for his many years of mentorship inside and outside the classroom. His unwavering faith in me, words of encouragement and fatherly counsel were invaluable for my professional and personal development. Dr. Gary Hawkins, professor, mentor and father figure – thank you. Dr. Hawkins always believed in me and was there to gently guide me through some of my life's greatest challenges. Very special thanks to Dr. Art Bronson for his many years of mentorship, both academic and personal. Dr. Bronson rigorously guided my unfocused efforts when I was a young undergraduate. He always strived to keep me on the correct path and I owe much of my academic success to his teachings and solid guidance. I also would like to extend my deepest appreciation to Dr. Dennis L. O'Neal, my doctoral adviser. He has patiently guided my efforts through my doctoral degree, the completion of this thesis and my formation as a professional researcher.

Great appreciation goes to my dear friends and research team: Cesar "Olympia" Terrazas, Marco "Magain" Magaña and Emmanuel Gurrola. They tirelessly worked with me day and night for three months in order to build, calibrate, and run the experimental facility. They did this on a completely voluntary basis and a great amount of their ingenuity, technical knowledge and manual labor was invested in this research. I dedicate this study to them as well, for this research is also the fruit of their labors. This study would not have been possible without their vast amount of assistance, humor and unconditional support.

I am grateful to my father Antonio Cornejo for his motivation and support. I thank Miss Elizabeth Pardo for all her support and financial assistance. Very special thanks to Miss Jami Tullius for her counsel and motivation through the writing phase of this thesis. Thanks to Rev. Will Stratten for the spiritual direction which kept me focused and to my best friend, Rev. Jairo Sandoval-Pliego O.P., for his prayers, friendship and sound advice. I would also like to express my deepest gratitude to Mr. Alfredo Rivera whose assistance and many years of friendship were invaluable in making this research and thesis defense possible. Last, I thank my godmother Consuelo Escutia and my aunt Mary Cardona for their love, continual support and for being with me at the culmination of this study.

I am deeply appreciative to those individuals, businesses and institutions that at any particular point supported my research financially or by donations. I am extremely grateful to Dr. Louis Everett for his research funding support and Dr. Connie Gomez for financially supporting me during the experimental portion of this study. I would like to thank local businesses who supported this research: Mr. Xavier Fuentes at Mechanical Representatives Inc. for the donated industrial air movement equipment and Garick Electrical and Mechanical for all the customized ductwork and technical consulting. Special thanks to the UTEP Graduate School for funding a part of my investigation through a research grant.

Finally, I would like to thank Dr. Barry Benedict and Dr. Anthony Tarquin for serving on my committee and reviewing my manuscript within a very small lead time. Thanks to Dr. Jack Chessa for assisting with my academic reinstatement and especially Dr. Ahsan Choudhuri for his patience, support, and for allowing me to use his laboratory facilities for my experimental work. Special thanks to Miss Laura L. Orozco for her outstanding assistance with my graduation and defense procedures. Finally, I thank my friends, associates and university staff for all their support & assistance during this investigation.

Abstract

Potable water is becoming a scarce resource in many arid regions of the world. An experimental unit was designed and constructed to examine and characterize the production capabilities of a humidification-dehumidification (HDH) desalination process. An HDH cycle offers a viable, technologically light, alternative for producing fresh water from brackish water because the low relative humidity air is infused with water vapor through evaporation by means of conventional heating, ventilation and air conditioning (HVAC) components. The evaporation process effectively separates salts and suspended solids from the brackish feed-water. Desalinated water is subsequently recovered by extracting the water vapor from the moist air through condensation.

The study used CELdek™ cellulose evaporative media (CEM) varied from 4.0" to 16.0" for air flow rates of 400, 600, 800 and 1000 CFM. Two system configurations were tested, single and two-stage, where each stage was comprised of a heating and humidification process. Water production for single stage experiments varied from 0 – 10.82 lb_w/hr for 4.0" and 16.0" CEM thicknesses, respectively, at 1000 CFM. Similarly, at 1000 CFM, two-stage experiments' water production varied from 4.22 – 17.94 lb_w/hr, for 4.0" and 16.0" CEM thicknesses, respectively. Analyses of the data indicate that the HVAC-HDH process investigated is highly inefficient because the system's values of performance (PR) and gained output ratios (GOR) are below 1.0. Moreover, the experimental system would require a solar pond size of 0.27 acre to adequately provide all thermal energy requirements, mitigating the need for conventional power sources. Water samples from the prototype unit's production had a mean conductivity of 19±2 μS/cm, establishing the system's effectiveness for desalinating water.

Table of Contents

List of Tables

List of Figures

Chapter 1: Introduction

Potable water is becoming a scarce resource in many arid regions of the world. Growing population presents an increase in water consumption in these areas. Conservation efforts in conjunction with water purification methods are employed in locations where the levels of naturally available drinking water are diminishing. Multi-stage flash desalination and reverse-osmosis are widely used for the treatment of high-salinity water. These methods are highly effective for desalinating water. Though efficient and capable of high production volumes, elevated construction, operational and maintenance costs are associated with these desalination technologies. Research is ongoing, however, to refine or develop new technology to address the varying needs and constraints of water-scarce regions. Other water desalination options may be implemented in cases where capital and technical personnel may be limited.

Water desalination methods that operate at local atmospheric pressure and conditions are widely investigated. Humidification-dehumidification (HDH) processes can be used for this end. The process is based on the concept that water vapor in humid air can be extracted by the removal of latent heat, i.e. condensation. This occurs when humid air comes into contact with a surface that is at or below the ambient dew-point temperature. Condensation can be observed in nature when dew collects on the leaves of plants in the early mornings or on a chilled glass sitting outside on a humid day. This condensate is typically low in dissolved solids, assuming no contamination from surface contact. This process can possibly be exploited for water desalination at larger scales. The concept of dehumidification of air to obtain water is not a new concept. Solar desalination produces rain when solar radiation causes seawater to evaporate and be absorbed by the atmosphere to form clouds. When the atmospheric temperature reaches the ambient dew-point temperature, the clouds dehumidify as rain

[1, 2][1]. Legoff [3] states that in the Sahara Desert before sunrise, people collected fresh water from the atmosphere in plastic lined funnel-shaped holes in the ground. This condensate recovery method helped both engineers and scientists recognize its potential and begin developing technology to replicate this process. The earliest HDH solar distillation plant on record was designed and built in 1872 by Corrols Wilson in Chile [4]. The still was in operation 36 years after its construction. Solar stills and HDH desalination processes of different kinds are still researched today in an effort to make them more efficient and cost effective for implementation at larger scales.

Analytical and experimental studies dedicated to the development or modeling of desalination processes are abundant. Historically the majority of this research has been directed towards the development of new or existing large scale operations, often involving complex technology. Desalination of seawater, for example, is generally performed by large scale processes involving evaporation or semi-permeable membrane separation. The most important thermal energy based large-scale desalination processes include multi-stage flash (MSF) desalination, multiple effect distillation (MED) and vapor compression (VC) [1]. Widely used industrial scale desalination membrane technologies include reverse osmosis (RO) and electrodialysis (ED). Large production capabilities, on the order of 1,000,000 m^3/day for some MSF plants, [1] make these technologies commercially successful and attractive. However, smaller scale desalination methods have not been developed to larger scales and merit further research. Expanding our knowledge of these alternative technologies can help make them more efficient, cost effective and possibly commercially successful in small to medium scales.

There is a need to examine methods that employ technology that is less operationally complex and adaptable for decentralized water production. Desalination processes operating at ambient atmospheric conditions, though simpler in operation and implementation, have lower desalination

[1] Citation style follows the standards of the American Society of Mechanical Engineers (ASME)

capabilities and higher production cost when compared to industrial scale processes. It stands to reason that this type of process is overlooked in favor of those with the potential to solve larger scale water shortages at a lower cost. HDH desalination using HVAC technology is an alternative to these large scale processes. The HVAC-HDH desalination plant designed for this investigation is technologically light, has relatively lower maintenance and construction costs and does not require highly skilled personnel to operate it. Not as compact or easy to implement as solar stills, this investigation demonstrated that the HVAC-HDH desalination unit has higher production capabilities than a solar still. Its modular design facilitates its placement in arid regions that are far removed from large urban power grids or potable water sources. Though thermal energy intensive, this process can be coupled with a salinity gradient solar pond to provide the thermal loads necessary for the heating processes. In the absence of a solar pond, the system is fully operational without an industrial scale power grid. Brine disposal is not an issue with this system. Most solids in the brackish feed-water will be deposited in the evaporative media used for the humidification processes. Brine evaporation lakes, both costly and potentially hazardous for the environment, are not necessary with this system. Additionally, any sodium chloride in the water can potentially be removed, treated and reused for the maintenance or construction of a larger salinity gradient solar pond. Most importantly, this investigation sets the groundwork to further explore a novel application of HVAC systems – water desalination.

The purpose of this research was to evaluate the performance and production capabilities of a desalination plant based on a previous theoretical study by the author, Enriquez and Love [5]. To satisfy this objective, an experimental desalination unit was designed and constructed to replicate the HDH process of the theoretical study. The desalination method tested is based on a series of simple psychrometric processes. The pilot plant is an operational HVAC system designed to exploit these processes. Air humidification is accomplished by interfacial contact with a large wetted surface area provided by commercially available corrugated cellulose evaporative media (CEM). The experimental

unit's design is modular, expandable, easily modifiable and technologically less complex in comparison to other advanced desalination methods. Plant operation and production were evaluated at different testing conditions in a closed laboratory setting. Conductivity testing of the produced water was performed to evaluate the desalination efficacy, and ultimately the success, of the desalination process.

Studies on an HDH system with this configuration were not found in the open literature. Collectively, this research will contribute new knowledge to better understand HDH processes and the use of HVAC equipment for water desalination. It is anticipated that this work will be used as a basis for future studies to improve plant design, energy efficiency and production capabilities.

This thesis is organized into seven chapters. Chapter 2 is a review of the pertinent scholarly literature for this investigation. Chapter 3 is a discussion of the supporting theory and technical background for this study. Chapter 4 describes the pilot plant setup, operating procedures and test matrices used for the experimental portion of the study. Chapter 5 outlines the data reduction and analysis methodology implemented. Chapter 6 presents the results and accompanying analysis of the thermal-fluid and psychrometric processes as well as a discussion of the pilot plant performance. Finally, chapter 7 finishes this investigation with the overall conclusions and recommendations for related future work.

Chapter 2: Literature Review

Published desalination research dates back over 100 years producing various models and a plethora of data leading to the development and construction of several successful desalination units. The scholarly literature review that comprises this chapter is primarily focused on HDH thermal desalination research. Membrane desalination, such as reverse osmosis, thermal desalination technologies such multi-stage flash desalination and other topics of interest will be discussed as needed in this chapter.

2.1 Review of Selected Desalination Topics

The following main areas were considered in the selection of scholarly literature for this thesis:

2.1.1 The need for water desalination – a brief discussion

2.1.2 Overview of conventional desalination technology

2.1.3 Environmental impact of desalination plants

2.1.4 HDH desalination technology

2.1.5 General economic implications of desalination operations

2.1.1 The need for water desalination - a brief discussion

Historically, major human civilizations have developed near sources of potable water, most notably the ancient Egyptian civilization at the Nile River, Mesopotamia (i.e. the "cradle of civilization") between the Tigris and the Euphrates River and Constantinople (modern day Istanbul) built on the Bosphorous Strait along the Golden Horn natural harbor. Ancient Rome, though built around various natural springs, engineered its famous system of aqueducts for water transport as increasing population growth depleted its potable water sources. The importance of this resource has

driven engineering science to develop methods or technology to supply the growing demand for potable water. Water desalination is widely researched and implemented for this purpose.

Water desalination is investigated as world population increases and potable water resources diminish. The World Health Organization reports that over one billion people lack access to purified drinking water [2], most of them in areas where the construction of large scale desalination operations are not feasible due to poor infrastructure or lack of accessibility to municipal power grids. Another vast majority of people reside in highly urbanized areas where population density strains the available water resources. The average amount of drinking water needed daily by humans is 5 L (1.32 US gal) but can vary from 2 L to 8 L (0.53 – 2.11 US gal) [2]. It is also estimated that nearly 80% of the world's diseases are attributable to inadequate water supplies, sanitation and water treatment [6]. Growing populations worldwide are coupled with growing infrastructure and agricultural activity, further straining water supplies. Tourism and worldwide industrialization due to the global market are causing population shifts which require potable water availability in previously underdeveloped regions. The United Nations suggests that 1500 m^3/year/capita of renewable fresh water is required to support economic development [4, 7]. It is evident that potable water is necessary for human health and for urban and economic development, [4].

2.1.2 Overview of conventional desalination technology

Desalination research has been actively pursued in the United States and internationally since the end of World War II in response to rapid increases in urban population, infrastructure development and industrial activity. The now retired U.S. Office of Saline Water (OSW) and several international symposia sponsored by the OSW and European Working Party (EWP) on "Fresh Water from the Sea" (eventually transforming into the International Desalination Association –IDA) fueled worldwide research. The effort led to the development of reverse osmosis, multistage flash and vapor compression desalination technologies, among others [8]. In recent years desalination research has largely been

undertaken by private companies or academic institutions. The international engineering community continues to innovate and develop desalination technology, making it more efficient and economically attractive.

As previously discussed, the need for dependable and efficient desalination technology grows with increasing world population and expansion of urban development. Engineering's response to this demand has been the development of several desalination technologies ranging from simple solar stills to commercial units capable of producing vast quantities of potable water. Today, over 15,000 desalination facilities operate in more than 120 countries worldwide with a combined potable water production in excess of 500 million gallons per day (gpd) [7]. Presently, of the water produced by desalination technologies, treated water accounts for 5%, brackish water (≈2000-10000 parts per million, i.e. ppm) for 22% and seawater (≈10000-35000 ppm) for 58% [9]. These numbers are expected to increase as research in this field and new technology make desalination more attainable and cost effective.

Phase change desalination methods apply thermal energy to evaporate saline water, leaving salts and suspended solids behind. Clean water vapor is recovered through condensation, collected and further treated if needed. Narayan et al. [1] list solar stills, multi-stage flash desalination, multiple effect distillation and vapor compression systems as the main thermal desalination processes. Solar stills are a basic and technologically "light" desalination whose operation depends purely on solar energy. Conventional stills are among the oldest of the desalination technologies, some dating back to 1872 [4]. Solar still technology has been widely investigated and their functional capabilities are well documented in literature. Though still technology varies from single effect, wick and diffusion stills, among others, their most attractive features are their simplicity and robustness [10, 11]. This facilitates their implementation in areas far removed from urbanized locations [1, 2, 10] as they are self-sustaining, requiring only solar energy. Stills require a small capital investment for their construction and minimal

technical expertise to operate and maintain [2, 10, 11]. Though attractive for these reasons, solar stills have some major drawbacks rooted in their thermal inefficiency and low production capabilities. State of the art solar stills have thermal efficiencies in the range of 30-40% with production capabilities ranging from 4-5 $L/m^2/day$ [1, 2]. As a result they can only be used in areas where freshwater demand is low. Technologies such as salinity gradient solar ponds, flat plate, evacuated tube or parabolic trough collectors are indirectly used to harness solar energy to provide thermal heat loads or electricity for other desalination systems. Quiblawey et al. [2] present a survey of these technologies, their use and capabilities.

Solar desalination, driven by thermal energy, is a variant of the phase-change (thermal desalination) processes. With the exception of solar stills, these technologies are suited for large scale or commercial implementation. Continual research in phase-change desalination methods aims at improving their overall effectiveness and cost competitiveness. MSF and MED desalination plants are often coupled with solar technology to provide the thermal energy and/or electric power in an effort to make them more efficient and environmentally conscious [2, 6]. Solar driven MSF units, for example, have production capacities in the range of 6-100 m^3/day [2], depending on the solar technology used. The latter production rate is from an MSF plant in Kuwait using parabolic trough collectors. However, commercial scale MSF plants powered by conventional means, such as fossil fuels, have production levels ranging from 100,000 to 1,000,000 m^3/day [1]. Predominant between 1980 and the late 1990s, MSF desalination (presently accounting for only 25% of the worldwide share of desalinated water) has decreased as RO technology becomes more efficient and cost competitive [12]. Along with MSF desalination, MED is also capable of commercial scale production volumes. MED, with average production capabilities between 16,000 m^3/day and 22,500 m^3/day, accounts for only 8% of worldwide desalinated water [12, 13]. Despite its modest production capacities and widespread use in various

process industries [12], MED has failed to compete with MSF and RO technologies [12, 13]. RO and MSF remain the most commercially successful methods of large scale water desalination [1, 14].

Reverse osmosis is the most widely used membrane technology for both seawater and brackish water desalination. Membrane processes function by either prohibiting or permitting the passage of certain salt ions through a filter or membrane [12]. RO functions by pressurizing saline water against a membrane in a closed vessel, allowing pure water to permeate and leaving a concentrated brine solution behind. Depending on the type of RO process, brine solution may be passed through another stage (or series of stages) to further extract pure water [15]. Reject brine from the desalination process is then discharged into the ocean, deposited in evaporation ponds for further processing or disposed of [15-18]. Though highly efficient and largely automated, skilled technical personnel are required to operate and maintain the equipment comprising a typical RO system [19, 20]. Heavy power consumption and elevated construction and maintenance costs are inherent of a basic commercial sized RO plant [14, 15] . Despite these drawbacks, RO technology currently dominates desalination processes in the US, Spain and Japan [21]. With water production capabilities reaching 330,000 m^3/day and an average cost of \$0.53- 3 USD/ m^3 [1, 12], RO is currently the most cost competitive commercial level option for water desalination.

2.1.3 Environmental impact of desalination plants

The negative environmental impact of commercial desalination technologies such as RO and MSF is a growing concern. Large scale desalination plants can generate concentrated brine discharge that can contaminate aquifers or ecosystems [12]. Additionally, industrial grade RO and MSF systems, responsible for 78% of the worldwide desalination production [12], are highly energy intensive processes [20]. This elevated energy demand is one of the reasons why these technologies are ill suited for decentralized water production removed from municipal power grids [1, 2]. Moreover, these technology-intensive systems are heavily reliant on conventional fuel sources, including fossil fuels and

nuclear energy, for their electrical and thermal energy demands [1, 3]. Therefore, these technologies are feasible for economically developed and technologically advanced regions of the world [19]. Quiblawey et al. reported in 2008 that an estimated 10,000 tons of oil per year are needed for 1,000 m^3 of fresh water production per day [2]. Though desalination technology continually improves in efficiency, the amount of fuel consumption by commercial scale technologies is considerable. In addition to the large carbon footprint of these plants, they are also sensitive to the price of oil – causing the average water production cost to fluctuate [1, 12]. Reliable, environmentally and cost conscious desalination alternatives are necessary, particularly for underdeveloped regions.

The byproducts of large scale desalination operations are detrimental to the environment if not managed properly. Brine discharge with elevated salinity and temperature levels is toxic or fatal if released in large quantities into marine ecosystems balanced by ocean temperature and chemistry [9]. Mezher et al.'s survey [12] reports that brine discharge of a typical MSF plant is 7-15 °C hotter and 15-20% more saline than the feed water. It also reports that on average, the total dissolved solids (TDS) of RO reject discharge are 50% to 80% higher than the feed water's. Moreover, concentrated brine and chemical discharges from desalination operations are often mixed with different pretreatment chemicals or even nuclear contaminants if coupled to a nuclear power plant [9]. RO membranes' high susceptibility to fouling [11] makes it necessary to pretreat feed water in order to avoid malfunction, decreased efficiency and elevated maintenance costs. The whole effluent from different desalination operations, usually a mixture of biocides (e.g. chlorine), coagulants, antiscalants, heavy metals (e.g. iron, nickel, copper) and antifoaming agents (particular to thermal desalination processes), is hazardous if not managed properly [9]. Latteman and Höpner [9] present a comprehensive review of the environmental impacts of large scale desalination. They review the effects of chemical and brine discharges on marine ecosystems and the effects of plant construction on coastal sea beds. Their discussion also stipulates

recommendations to evaluate, manage and reduce the negative environmental impacts of commercial desalination operations.

Mass scale desalination, though alleviating the growing problem of worldwide potable water depletion, is not without its caveats. Research is ongoing to minimize the negative effect of these processes or to develop environmentally conscious desalination technology. Scholarly literature on renewable energy source (RES) based desalination technology is abundant. Solar stills, for example, are a simple RES technology driven by solar energy. However, if the production capabilities of a RES powered desalination plant are to be maximized the energy source must complement the technology it is coupled with. Mathioulakis [11] presents a comprehensive review of technologies compatible with RES and suggests general guidelines to pair the correct technology to the adequate energy source. HDH desalination is one form of technology that can potentially use solar energy in an effective manner.

2.1.4 HDH desalination technology

The HDH cycle is a phase-change desalination processes. Like the solar still, MSF and MED desalination processes, its function is based on providing a heat load to saline water and using evaporation to separate salts and suspended solids. This type of desalination technology is widely investigated as it can be adapted to use solar technology, directly or indirectly. Unlike MSF and MED It is potentially well suited for low to medium volume decentralized desalination. RO systems, can also be used for low production volumes but require continuous power and expensive equipment [22, 23]. These conventional systems can be retrofitted to use solar energy; however, it may not be economically feasible due to elevated solar equipment and maintenance costs [23].

HDH systems can feature technologically light designs that may require less power than conventional systems and can be adapted to take advantage of solar energy. As environmental concerns escalate, there is also a need for desalination units that can operate successfully with RES or solar power while minimizing energy expenditure, carbon footprint and potentially hazardous by-products. For

example, low-grade heat from a solar pond can be used to provide thermal energy or electricity for air driven HDH cycles. Salts left behind from the evaporation process of the HDH cycle can be used to recharge or expand a salinity gradient solar pond, and create a "zero discharge desalination system" as described by Lu et al. [24]. While HDH desalination has not been proven commercially successful, it offers a viable, low capacity (1-100 m^3/day) option for use in water-scarce, arid locations with abundant solar energy. Moreover, reduced equipment, maintenance and operation costs make these systems a good fit for use in solar rich, developing regions which suffer from water scarcity and underdeveloped infrastructure.

HDH desalination processes mimic the natural rain cycle [23] to produce fresh water. The process uses atmospheric air as a carrier gas for water vapor. Process air, typically moved through the system by a mechanical blower, is heated and subsequently subjected to a humidification process. This process uses saline water as the source for air humidification. The water vapor gained by the air through the evaporation process is recovered as a highly pure liquid through condensation. Though there are several variations of HDH desalination systems, they are all comprised of three main subsystems: air and/or water heaters, humidifiers or evaporators and dehumidifiers or condenser [22, 23]. These subsystems can be readily designed or retrofitted to take advantage of solar energy directly or indirectly.

HDH systems are typically categorized as closed water-open air (CWOA) and closed air-open water (CAOW) configurations. CWOA systems cycle the water for the cooling or preheating processes through a closed circuit while process air is released into the surroundings. Conversely, CAOW systems cycle air through a closed circuit while system cooling water is not reused. A study conducted by Narayan et al. [23]determined that closed air and closed water cycles have similar thermodynamic characteristics and thus comparable performance. The configuration used is largely dependent on space, equipment, cost factors and design parameters. CAOW systems usually have a larger physical footprint, require more ducting and air drying equipment and thus have elevated costs. This type of system offers

other opportunities not available in open air systems; mainly the possibility for heat recovery from the air, air treatment or preheating. These processes can be implemented to improve overall system efficiency. Both system configurations offer several unique design options which must be evaluated to better suit financial, infrastructure, geographical or energy constraints.

Several studies have been conducted to evaluate the effect of different operational parameters on system production capacity and efficiency. Investigations of this type are highly system specific as HDH systems vary greatly in design. However, the nature of the HDH cycle presents some common parameters irrespective of the system configuration. System air flow, feed and cooling water characteristics, for example, are commonly studied to assess their effects on system performance. Data on the effect of system air flow on productivity is varied in the literature. Parekh et al.'s review [20] states that many authors conclude that air flow rate has minimal or insignificant effect on HDH system productivity. Dai and Zhang's [25] investigation of an CWOA, multiple effect humidity (MEH) system using cellulose honeycomb packed media for air humidification indicates that air flow rate does improve system productivity. Their data show that production will peak at a maximum value before decreasing with increasing system air flow. Another study by Al-Hallaj et al. [19] observes that increased air velocities can offset diminished water evaporation rates at low temperatures. The authors conclude that moderate forced air circulation at low operating temperatures can be advantageous for system fresh water production. El-Agouz's investigation of an HD desalination unit using air bubbles passing through brackish water [26] cited a 3.9-4.2% increase in system productivity by increasing air flow rate. Narayan et al. [1, 23] state that air preheating and volume flow rate have a small effect on system production at atmospheric operating pressures. These authors postulate that air preheating will have a more significant effect on a unit operating at sub-atmospheric pressures [23]. Increased humidity ratios at low pressures would translate to improved HDH system productivity and overall performance [1]. A different study by Kassim et al. [27] investigated air humidity effects on a system using a parallel-plate

channel humidifier. The data indicated that air humidity affects airflow characteristics in addition to heat and mass transfer. Elevated air humidity levels at the evaporator entrance results in diminished system performance. Kassim et al. recommend low evaporator inlet humidity to augment system performance.

Investigators seem to be in far more accord with regards to feed water preheating and flow rate. Several studies deduce that feed water preheating has a notable effect on system productivity. Al-Hallaj et al. state that there is a strong effect of the temperature of the feed water sprayed in the humidifier of their HD unit; as much as 80% increase in the system's performance factor with a 20°C increase of the feed water temperature [19]. The authors cite the non-linear increase in the water vapor pressure as the dominating factor for the performance increase. Kassim et al.'s [27] numerical study on a parallel-plate channel humidifier recommends feed water preheating to improve overall system performance. Several studies in open literature suggest that using recovered latent heat from the condensation process or solar energy to preheat the feed-water will significantly improve system performance.

Moreover, Parekh et al.'s review of HDH technology [20]states that a majority of authors agree that in addition to feed-water preheating, increasing its flow rate in the evaporator is far more effective for improving system efficiency and production capacity. A study conducted by Yamali and Solmuş [28] on a solar powered HDH system demonstrated that while increased air flow had a marginal effect on system productivity, a 0.04 kg/s increase in feed-water flow rate incremented fresh water production by as much as 49%. Their data also indicated that increased cooling water flow rate in the condenser improves overall system performance. The condenser's enhanced ability to remove heat from the air decreases coil surface temperature, effectively lowering the apparatus dew-point and enhancing the condensation process. Narayan et al. [23] make a similar claim stating that in conventional systems operating at atmospheric pressures, the condenser unit is of more importance for improving productivity than the evaporator.

While there are several methods used to humidify process air in the evaporator (e.g. fine mist sprayers, air washers) closely packed evaporative media seems to be extremely effective for this end. Several studies reviewed (e.g. [22, 25]) cite the use of media packing, whether cellulose or metal (as in cooling towers) for enhancing air saturation. Packed evaporative media provides a large amount of wetted surface area and extended air-to-water interfacial contact time [1]. Increased pressure drop through the system, inherent in the use of close packed media, must be carefully considered. Enhanced evaporative efficiency should not be offset with increased power input to the system for effective air movement. Parekh et al. suggest that packing material should be selected as to provide high contact surface area while minimizing pressure drop [20].

2.1.5 General economic implications of desalination operations

Establishing a definitive economic analysis of different desalination operations is difficult due to the wide scatter of economic data. The various parameters affecting the average cost of water directly affect production cost data; most notably plant size, feed-water type, fuel and maintenance and construction costs. The last two factors are due primarily to the variation in desalination system configuration. Review of the open literature reveals that there is just about every variation and size of desalination systems in operation, from prototype models with new technology to be field tested or RES-fossil fuel hybrid systems. As previously discussed, large scale desalination processes are easily swayed by fuel costs, particularly fossil fuel dependent technologies. While alternative energy based processes have are not yet commercially successful and profitable, they may still be a competitive option for smaller scale, decentralized, potable water production.

Karagiannis and Soldatos [29] presented a concise review of water desalination cost literature spanning various technologies from RES to conventional fuel powered. Type of feed water and plant production capacity are two important factors in determining the cost of water production. According to the authors, RO systems, predominantly employed in brackish water desalination, produce water at an

average cost of \$0.78 - \$1.33 USD/m^3 for plants with production capacities between 20-1,200 m^3/day. For larger RO plants with average capacities between 40,000 – 46,000 m^3/day, costs can vary from \$0.26 to \$0.54 USD/m^3. Seawater contains ten times the number of contaminates and salt than brackish water [29]. RO membranes' sensitivity to the feed water's level of suspended solids and chemical composition make it less suited for seawater desalination; partly due to elevated membrane replacement costs. Yet in recent years, according to the authors, improved RO technology is gaining widespread use for highly saline water treatment. They report RO desalination costs of seawater to vary between \$0.70 - \$0.66 USD/m^3 for plant capacities of 1,000-320,000 m^3/day. Narayan et al. [1] and Mezher et al. [12] report seawater RO desalination costs between \$0.53- 3.00 USD/m^3 for operations with similar production levels.

Higher desalination costs are associated with RES powered RO desalination plants. Al-Hallaj et al., for example, [30] report costs of desalinated water using various RES based RO systems to be within \$0.86 – \$12.05 USD/m^3. Karagiannis and Soldatos [29] state that solar based RO desalination can reach \$10.32 USD/m^3, depending on the technology implemented. Advancements in solar and RES technologies continue to improve the overall efficiency of desalination methods employing them. Though promising, these desalination processes are far from being competitive alternatives to conventional processes. Conventional processes offer a superior advantage in terms of cost and production capabilities.

MSF and MED are high capacity processes that are more commonly used for desalinating seawater. The elevated energy requirements inherent to these particular thermal processes make them highly dependent on conventional fuel such as oil and are thus sensitive to fluctuating oil prices. However, these processes are predominant in oil-rich Middle Eastern countries [9] where seawater desalination is essential for sustaining the needs of the growing population and fuel demands can be met. Karagiannis and Soldatos [29]report a cost of \$0.52-\$1.75 USD/m^3 of desalinated seawater for MSF

facilities with production capacities between 23,000-528,000 m^3/day. The authors also report that desalinated seawater from MED plants with average production capacities of 12,000-55,000 m^3/day has a cost of \$0.95-\$1.95 USD/m^3, according to other published literature. Fresh water from larger MED operations with production volumes exceeding 91,000 m^3 /day has a cost between \$0.52-\$1.01 USD/m^3.

Solar powered phase change desalination methods are heavily investigated since solar energy can be used directly or indirectly by these processes; e.g. solar stills or HDH methods. The price per cubic meter of fresh water produced by a solar driven process is highly dependent on the desalination and solar technology used. Most cost data in the open literature is primarily case specific, though some authors do report some conservative estimates. Al-Hallaj et al [30], for example, reported that water desalinated with solar-MED had an average cost between \$0.67-\$4.70 USD/m^3, depending on the type of solar technology employed (e.g. solar ponds, parabolic troughs and hybrid systems, among others). Additionally, solar-MSF desalinated water costs were within \$1.79-\$2.84 USD/m^3 according to these investigators.

Economic data for water desalination processes vary greatly among different scholarly publications due to the extensive number of parameters that can influence cost. Economic analysis methods and continually changing cost data for fuel, materials and research directly affect reported fresh water production costs. The author selected references [29, 30] as a basis for this brief economics review due to their wide scope and relevance to the investigation. The reader is referred to these publications for specific economic and analysis details as well as a complete list of references.

2.2 Conclusions

Scholarly and technical literature on the subject of water desalination is vast and continually growing as research in this area advances. The articles for this literature review were carefully selected in an effort to sample the wide spectrum of scholarly literature with relevance to this investigation. The following conclusions were reached following this review:

1. A great variety of desalinations methods are in operation and continual research in this field produces several variants. Studies demonstrate that preheating feed water improves plant desalination efficiency irrespective of the desalination technology used, feed water type (i.e. brackish or seawater), fuel source or plant production capacity.
2. Conventional fuel powered RO, MSF and MED desalination plants are very efficient and cost competitive for commercial scale desalination. These technologies are primarily used in economically developed regions capable of supporting their elevated energy demands and fuel consumption levels. The negative environmental impacts of these conventional technologies can be severe and need to be carefully evaluated, monitored and minimized.
3. Environmentally conscious, RES based desalination is not yet commercially successful and is applicable for low and medium capacity decentralized desalination. This type of desalination technology is a promising alternative for said application if coupled with the correct RES and merits further research.
4. Phase change desalination systems can more readily be modified to use RES including solar energy (e.g. salinity gradient solar ponds, solar panels, parabolic troughs) wind energy or geothermal energy, among others. HDH systems are especially well suited for direct or indirect use of solar energy for their desalination processes.
5. Closed or open air HDH desalination system efficiency and production capacity is improved with higher air mass flow rates and feed water preheating. Elevated air humidity is detrimental to the system's performance and efficiency.
6. Economic analysis of desalination technology is difficult due to the various factors influencing production costs and the vast configuration options of desalination units. Thus, cost analysis is best performed on a case by case basis and evaluated against established, conventional desalination methods.

Though HDH systems typically incorporate HVAC components such as heat exchangers or cooling towers, there is limited published research on multi stage, CWOA, HVAC based HDH systems using corrugated cellulose evaporative media and solar ponds. The prototype system developed is a modular and fully functional HVAC system which can be expanded to accommodate multiple heating and humidification stages. Therefore, the objectives of the present study are:

1. Evaluate the production capacity of a two-stage HDH desalination system and compare it to theoretical results of a previously performed feasibility study.
2. Develop empirical relationships based on the obtained experimental data to predict the freshwater production capabilities of the prototype system.
3. Evaluate the effect of air volumetric flow rate and thickness of evaporative media on pilot plant production capacity.
4. Determine if a solar pond can provide the necessary thermal energy to drive the HDH process; if feasible, compute the size of the solar pond to achieve this end.
5. Evaluate the quality, i.e. salt concentration, of the desalinated water produced by the unit.

Chapter 3: Background Theory of the HDH Cycle

There is a predominance of research on large-scale desalination processes in an attempt to optimize their performance while minimizing cost. Desalination units that operate at atmospheric conditions have more moderate power consumptions and can potentially be driven by solar power, mitigating the need for fossil fuels. These technologically simpler units merit further investigation. The HVAC-based HDH desalination pilot plant in this study is a modular, functional unit with modest production capabilities. The experimental facility has the potential for optimization, integration to a solar pond and expansion to a large scale. The pertinent background theory necessary for understanding the basic HVAC-HDH cycle is presented in this chapter.

3.1 Overview of the HVAC-based HDH Process

Water desalination with the HDH process is based on a basic heat and mass transfer process that takes place in most ordinary evaporative coolers. Many owners of evaporative coolers are well aware of a problem that has them rushing to the local home supply warehouse every summer – fouled aspen pads or rigid cellulose media. Even when water in evaporative coolers is treated with a chemical softener, calcium and salt deposits on the evaporative media renders it useless (usually within a couple of summers of continual air conditioning use, based on personal experience). This phenomenon is part of a process that can be exploited for desalination of brackish water and possibly seawater. Let us briefly describe this process. Heat and mass transfer occur simultaneously when non-saturated air comes into contact with a body of water. Latent and sensible heats are exchanged between the air and water until the air is fully saturated and thermal equilibrium is reached between both species. When dry (i.e. low humidity) unsaturated air comes into contact with brackish water, the process just described takes place. However, brackish water contains elevated amounts of salts, on the order of 0.5-30 ppt. [10], and other suspended solids. The sensible heat from the air is enough to evaporate the water only, effectively

separating the various suspended solids from the brackish water. While the water vapor diffuses into the moving air, salts and other solids will be deposited on the evaporative media or in the water sump containing the brackish water. This water vapor can be recovered from the air through condensation if the air temperature is lowered below the ambient dew-point temperature. The water from this condensation process should contain only trace amounts of salt, as most dissolved solids are left behind during the evaporation process.

The amount of desalinated water recovered from the air is dependent on the number of humidification cycles. Therefore, this procedure can be used to desalinate brackish water if the process air has low relative humidity. Highly humid air will not be effective in this process as water vapor diffusion will be limited by its elevated moisture content. The open-air (does not recirculate process air) desalination unit of this investigation was designed to take advantage of this basic process. Its fundamental parameters and governing equations will be discussed in detail in the theory and background section that follows.

3.2 Fundamental Psychrometric Parameters

Knowledge of fundamental psychrometric parameters is important for a proper understanding of the processes involved in the HDH desalination cycle. This is instrumental for accurate computation of system parameters and production capabilities. Thus, every available effort will be employed in this thesis to make all theory and analysis tractable and practical. Let us proceed then to review some of these parameters before continuing with the governing equations of this HDH desalination process.

Atmospheric air contains water vapor, contaminants and other gases in its composition. Dry air, by definition, contains trace amounts of other gases and is free from contaminants and water vapor [31]. The standard composition of dry air was established in 1949 by the International Committee on Psychrometric Data [32]. Well accepted modifications to this standard made by Harrison (1965) and Hyland and Wexler (1983) are briefly discussed in reference [31]. The term moist air refers to the

gaseous mixture of water vapor, dry air and its constituents. The amount of water vapor in the air can vary from zero to saturation, a stable maximum that is dependent on pressure and temperature of an air sample [32]. It is important to note as well that psychrometric chart data, such as enthalpy, humidity ratio and specific volume, are all based on a unit mass of dry air [31, 32].

Moist air processes are at the heart of most practical HVAC processes and design procedures [33, 34]. Knowledge of moist air parameters and their relationship to concentration, partial pressure and enthalpy is central to the proper understanding of the psychrometric processes of this desalination method. Conservation and heat transfer relationships will be discussed in following sections. The parameters which define the humidity content in a sample of air will be discussed first. Humidity parameters are important as they are intimately related with nearly every other psychrometric or thermodynamic property of moist air. The humidity ratio, ω, of a moist air sample is a key property in psychrometric analysis as it quantifies the mass of low- pressure, superheated water vapor per unit-mass of dry air. The humidity ratio is defined as[2]:

$$\omega = \frac{m_w}{m_{da}} \tag{3.1}$$

Considering the partial densities and molar concentrations of these two species equation (3.1) is used to define the following relationship between humidity ratio and mole fraction of water vapor and dry air:

$$\omega = 0.621945 \frac{x_w}{x_{da}} \tag{3.2}$$

Assuming ideal gas behavior and employing the relationship between mole fraction and partial pressure we arrive at:

$$\omega = 0.621945 \frac{p_w}{p - p_w} \tag{3.3}$$

[2] ASHRAE conventions for subscripts will be used in this thesis. e.g. subscripts for water vapor and dry air are denoted by *w* and *da*, respectively. cf. 2009 ASHRAE Handbook: Fundamentals, I-P Ed. [31]

A review of basic relationships for concentration of species and details pertaining to the above referenced equations are found in Appendix A. Related to humidity ratio is the property called relative humidity. Relative humidity is important since it serves as a "reference point" for humidity measurements of ambient air. Recall that the saturation point of an air sample is dependent on its temperature and pressure. Relative humidity quantifies the water vapor concentration (i.e. the mole fraction) of a moist air sample compared to the mole fraction of a saturated sample at the same temperature and pressure [31, 32, 35]. Thus, relative humidity is defined in terms of mole concentrations and partial pressures of water vapor:

$$\phi = \left.\frac{x_w}{x_{w_{sat}}}\right|_{T,P} = \left.\frac{P_w}{P_{w_{sat}}}\right|_{T,P} \tag{3.4}$$

A parameter similar in function to the relative humidity is the degree of saturation, μ. This parameter, analogous to ϕ, is the ratio of ω to ω_{sat}, the humidity ratio of saturated moist air at the same temperature and pressure, i.e.:

$$\mu = \left.\frac{\omega}{\omega_{sat}}\right|_{T,P} \tag{3.5}$$

Using the definition of ϕ, ω and the molecular weights of dry air and water[3] (3.5) is rewritten in the following form:

$$\mu = \frac{\phi}{1 + \frac{(1-\phi)\omega_{sat}}{0.621945}} \tag{3.6}$$

Equation (3.6), though containing more terms than its basic definition, allows for direct computation of the degree of saturation from properties that can be read directly from a psychrometric chart, assuming ω is unknown.

[3] M_{water}=18.015268 kg·kmol^{-1}, M_{da}= 28.966 kg·kmol^{-1}cf. [31]

A frequently heard word on weather reports is the term "dew-point" or "dew-point temperature". This is a significant condition that is of particular interest to this desalination process. Let us put this term into perspective. A graduate student living in a particularly humid location (e.g. College Station, Texas, $47\% < \overline{\phi} < 92\%$) decides to purchase a chilled soft-drink on a typically warm and humid day. Walking across the street to another building, the student's hand is wet from a condensate film that has formed on the surface of the cold bottle. This occurred because the bottle's surface temperature was at or below the ambient dew-point temperature. Air in contact with the bottle was locally cooled to the surface temperature, resulting in drop wise or film condensation on the surface. In general, the ambient dew-point temperature, T_d, is that temperature at which water vapor begins to condense out of moist air. There is, however, a more technical definition of the dew-point temperature that merits discussion. The dew-point temperature is the temperature of moist air saturated at pressure P with the same humidity ratio ω_i of an arbitrary moist air sample *i* [31, 35]. It is mathematically defined as the solution $T_d(P,\omega)$ of the following:

$$\omega_{sat}(T_d, P) = \omega_i \tag{3.7}$$

Substitution of key conservation relationships into the following energy balance [31] (enthalpy balance for a saturated moist air[4]):

$$h + (\omega^*_{sat} - \omega)h^*_{water} = h^*_{sat} \tag{3.8}$$

leads to a more explicit representation of equation (3.7):

$$\omega_{sat}(T_d, P) = \omega_i = \frac{(1093 - 0.556T^*)\omega^*_{sat} - 0.240(T - T^*)}{1093 + 0.444T - T^*} \tag{3.9}$$

[4] Properties at a saturation state will be denoted by a superscripted asterisk (*). e.g. humidity ratio at saturation, ω_{sat} is denoted ω^* or ω^*_{sat}

There is also an analogous and useful relationship between dew-point temperature, pressure and vapor pressure.For perfect gases, the following relationship applies [31]

$$P_{w_{sat}}(T_d) = P_w = \frac{P\omega}{(0.621945 + \omega)} \tag{3.10}$$

where P_w is the partial pressure of water vapor for a moist air sample and $P_{wsat}(T_d)$ is the vapor pressure at the dew-point temperature, easily obtained from standard steam tables.

Dew-point temperature and its physical implications merit further substantiation. However, before discussing why air at the dew-point is indeed at a saturation state, as the condition of equation (3.7) imposes, the property of specific volume will be defined. In general, the specific volume of a pure substance is defined as the ratio of its physical volume to its mass:

$$v \equiv \frac{V}{m} \tag{3.11}$$

Assuming a dry air sample behaves as a perfect gas that obeys Dalton's Law with constituent partial pressures of water vapor and moist air:

$$v_{da} \equiv \frac{V}{m_{da}} = \frac{R_{da}T}{P - P_w} \tag{3.12}$$

Now consider a typical temperature-specific volume (T-*v*) diagram for water as shown in Figure 3.2.1. Points *f* and *g*, marking the limits of the mixture region on the diagram, are called saturation points because water vapor is at the saturation temperature at the particular pressure. Now, an air sample is said to be saturated once it reaches a temperature where its water vapor has reached the saturated vapor state, *g*, and begins phase change from superheated vapor to liquid – i.e. condensation. Therefore air at the ambient dew-point temperature is considered saturated because this is the "threshold" condition before it begins to lose water vapor through condensation. It can thus be stated that at this saturation point for an arbitrary pressure, air will hold the maximum amount of water vapor.

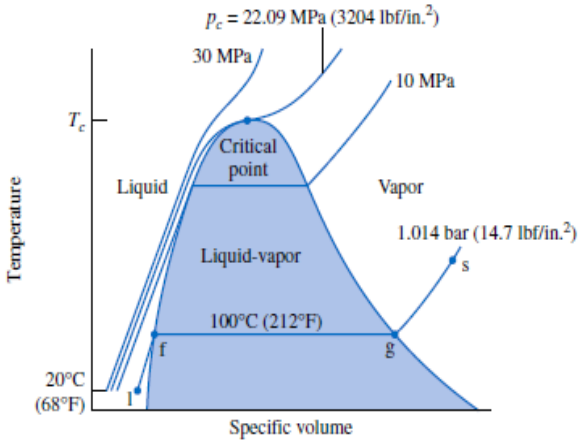

Figure 3.2.1: Typical T-*v* diagram for water [36]

Several parameters and properties that characterize an air sample have been thoroughly discussed. One of the most important properties of any pure substance is its enthalpy. Recall the following thermodynamic relation [37]:

$$c_p = \frac{\partial h}{\partial T}\bigg)_P \tag{3.13}$$

The enthalpy of moist air is solely dependent on temperature, assuming dry air and water vapor behave as perfect gases [37], therefore:

$$dh = c_p dT \tag{3.14}$$

Using this relationship the enthalpy of a moist air sample is defined. The total enthalpy for a mixture of gases is the sum of the enthalpies of each constituent component. Therefore, the specific enthalpy of moist air is defined as:

$$h = h_{da} + \omega h_{wg} \tag{3.15}$$

where h_{da} is the enthalpy of dry air and ωh_{wg} is the enthalpy of water vapor at the mixture temperature. The following approximations for dry air and water vapor[5] [32]:

[5] The following specific heat values are used: c_{pda} = 0.240 Btu·(lb$_m$°R)$^{-1}$and c_{pw} = 0.444 Btu·(lb$_m$°R)$^{-1}$; cf. [31]

$$h_{da} \approx 0.240T \tag{3.16}$$

$$h_{wg} \approx 1061 + 0.444T \tag{3.17}$$

provide temperature dependent expressions for the energy of both constituent gases. Please note that the water vapor enthalpy term, h_{wg}, includes the latent heat of vaporization, 1061 $\frac{\text{Btu}}{\text{lb}_\text{m}}$ plus the enthalpy of superheated water vapor. Substitution of these two approximations into equation (3.15) yields the following:

$$h(T) = 0.240T + \omega(1061 + 0.444T) \tag{3.18}$$

resulting in a temperature dependent expression for the total enthalpy of moist air.

Examining these different relationships begs the question of why there are several representations of the same relationship – other than elegant mathematical and engineering manipulation. It is important to understand that many of the relationships were developed as definitions serving to model and quantify a particular property or system characteristic. Unlike those relationships that were developed from experimental work and empirical data (e.g. specific heats, specific volume, etc.), there is no practical way of quantifying properties defined *a priori*. Mathematical manipulation is employed to circumvent this dilemma by recasting these property definitions in terms of measurable entities such as temperature and pressure.

3.3 Governing Thermodynamic and Psychrometric Relations

Air humidification is instrumental to the HDH desalination technique that was investigated. Humidification was done by direct contact with CELdek® 7060-15 rigid cellulose evaporative media (CEM), manufactured by Munters Inc. The humidification process attempted to mimic ideal adiabatic saturation. It is prudent to carefully revisit the fundamental notions of the adiabatic saturation equation. Specifying all moist air properties at a particular pressure and dry-bulb temperature requires the definition of a third property. Moist air enthalpy, specific or relative humidity or wet bulb temperature can all be used for this purpose. Direct practical measurement of these properties is difficult or not possible, as previously discussed. The adiabatic saturation process circumvents this difficulty by defining a relationship between measurable moist air properties. Consider an ideal adiabatic saturator of undefined length diagrammatically shown in Figure 3.3.1. By definition, the air exiting the adiabatic saturator has reached its saturation state, i.e. 100% relative humidity at the thermodynamic wet-bulb temperature ($\phi_2 = 1.0$ and $T_2 = T^*$).

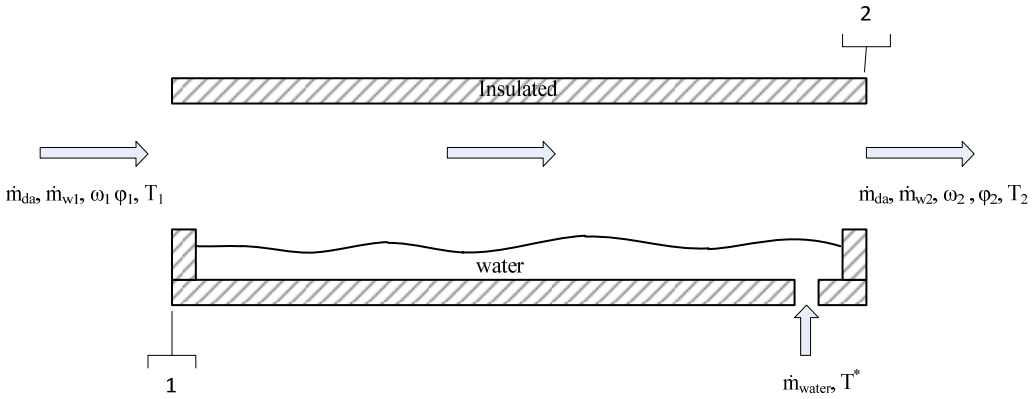

Figure 3.3.1: Schematic representation of the ideal adiabatic saturator.

The saturator is assumed to be of enough length for the air to exit at the desired saturation conditions. Proceeding to define the entering specific humidity for this process we recall the first law of thermodynamics [37] for an open system:

$$\sum \dot{m}_i (h_i + \frac{V_i^2}{2} + gZ_i) - \sum \dot{m}_e (h_e + \frac{V_e^2}{2} + gZ_e) + \dot{Q}_{c.v.} - \dot{W}_{c.v.} = \frac{dE}{dt}_{c.v} \tag{3.19}$$

Assuming a steady-state system with negligible changes in kinetic and potential energy, no heat transfer and power generation [23] the energy equation reduces to:

$$\sum \dot{m}_i h_i - \sum \dot{m}_e h_e = 0 \tag{3.20}$$

Conservation of mass for the system is dictated by:

$$\sum \dot{m}_e - \sum \dot{m}_i = \frac{dm}{dt}_{c.v.} \tag{3.21}$$

Steady-flow operation of the system reduces the conservation of mass equation to:

$$\sum \dot{m}_i = \sum \dot{m}_e \tag{3.22}$$

In this case, the two species flowing through the adiabatic saturator are air and water vapor with a constant flow of makeup water in the sump. Air in this analysis is considered to be dry air. Water vapor is treated as a separate species for analysis of the adiabatic saturator. If the mass flow rate of dry air is considered constant, i.e. $\dot{m}_{da1} = \dot{m}_{da2} = \dot{m}_{da}$, the conservation of mass equation for the system is expressed as:

$$\dot{m}_{da} + \dot{m}_{w1} + \dot{m}_{water} = \dot{m}_{da} + \dot{m}_{w2} \tag{3.23}$$

normalizing with respect to mass flow rate of dry air and recalling equation (3.1), the conservation of mass equation is expressed as:

$$\frac{\dot{m}_{water}}{\dot{m}_{da}} = \omega_2 - \omega_1 \tag{3.24}$$

This equation relates the total amount of water vapor transferred to the air during the adiabatic saturation process to the mass flow of the make-up water per pound of dry air. The net gain of water vapor by the air ($\Delta\omega$) is dependent on the mass flow of water at the thermodynamic wet bulb temperature in the sump. If the air is to gain the maximum amount of water vapor during the humidification process, the water distribution systems in the experimental unit's humidification chambers must keep the evaporative media completely wet.

Next, the system energy equation is rewritten to account for the enthalpies and mass flow rates of all species interacting with the control volume. Normalizing with respect to the mass flow rate of dry air yields:

$$h_{da1} + \frac{\dot{m}_{w1}}{\dot{m}_{da}} h_{w1} + \frac{\dot{m}_{water}}{\dot{m}_{da}} h_{f(T_{water})} = h_{da2} + \frac{\dot{m}_{w2}}{\dot{m}_{da}} h_{w2} \tag{3.25}$$

Substituting (3.24) into (3.25) and solving for ω_1 results in:

$$\omega_1 = \frac{(h_{da2} - h_{da1}) + \omega^*_{2sat}(h^*_{w2} - h_{f(T_2)})}{h_{w1} - h_{f(T_2)}} \tag{3.26}$$

Assuming dry air behaves as a perfect gas and realizing that $(h^*_{v2} - h_{f(T_2)})$ is the latent heat of vaporization at the thermodynamic saturation temperature T^*_2, equation (3.26) is recast as:

$$\omega_1 = \frac{c_{p_{da}}(T^*_2 - T_1) + \omega^*_{2sat} h_{fg(T^*_2)}}{h_{v1} - h_{f(T^*_2)}} \tag{3.27}$$

3.4 Fundamental Heat Transfer Relationships

This section will review the heat transfer background related to the primary heat exchange processes of the HDH desalination method studied. Three main heat transfer processes central to the desalination method will be discussed:

a. constant humidity ratio (ω) heating
b. latent heat transfer during humidification
c. heat transfer during condensation

Heat transfer to the surroundings will not be considered in this analysis. The experimental setup was not designed to record any heat losses via heat conduction through the walls or extraneous heat losses from components such as motors, pumps and fans. It will be assumed that any heat surrendered to the environment as a result of normal system operation is negligible when compared to the primary heat exchange processes.

Consider an arbitrary, single stage HDH sequence, i.e. one that is comprised of a single heating and humidification stage followed by a condensation process as shown in Figure 3.4.1. The air heating process, represented by the horizontal line from Point 1 to Point 2, is ideally only a sensible heat process with no change in the humidity ratio of the process air. Therefore, operational point of the air is shifted further to the right on the psychrometric chart's abscissa along a line of constant ω. This change of state of the air decreases its relative humidity; ergo, its water vapor concentration (relative to saturation at the same temperature and pressure) also diminishes – essentially amplifying the air's water vapor carrying capacity. The constant ω heating phase is executed in each stage of the HDH cycle to diminish the process air's relative humidity before entering a humidification phase. The present experimental unit incorporated a maximum of two heating and humidification stages. Test matrix details are discussed in the following chapter of this thesis.

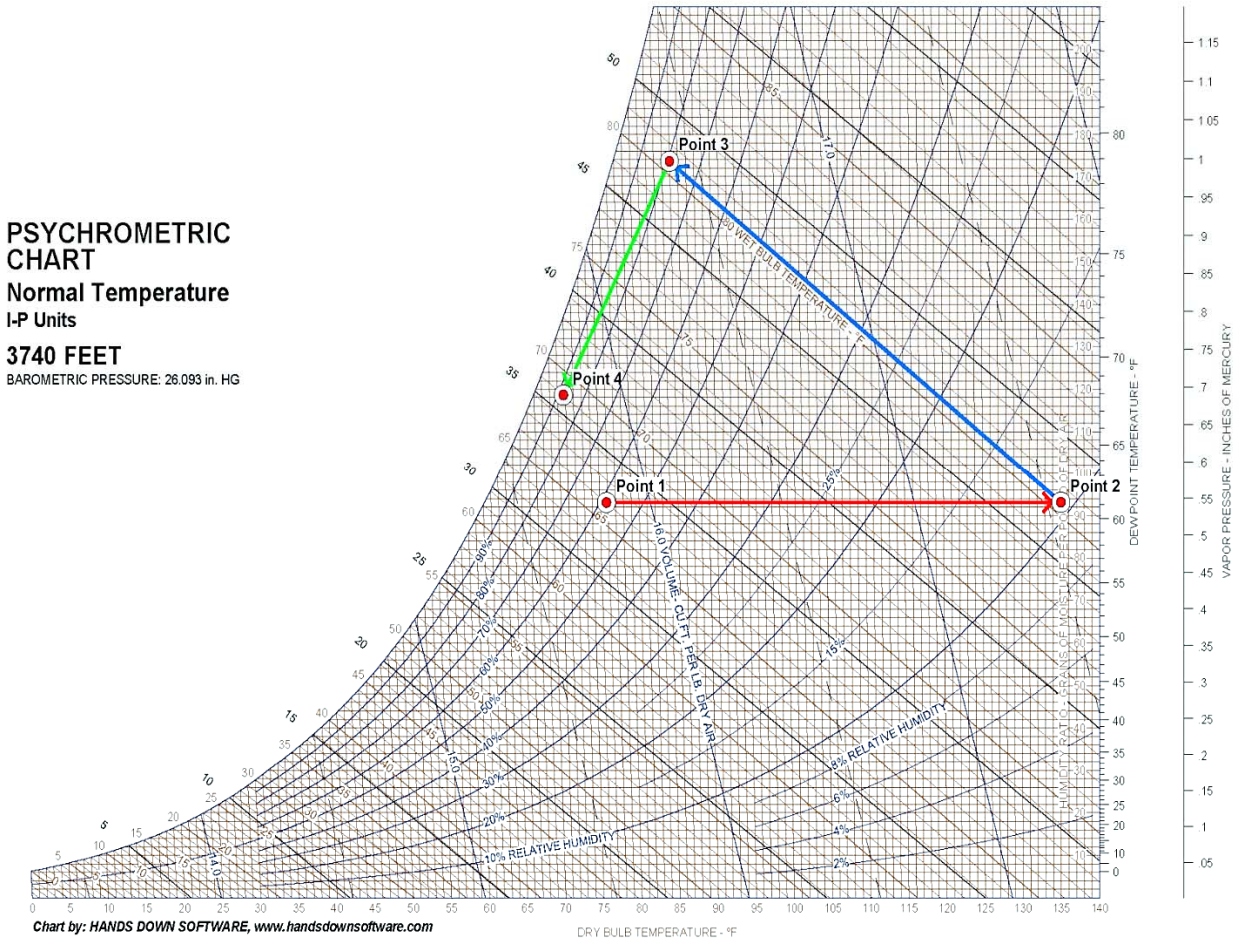

Figure 3.4.1: Psychrometric diagram of an arbitrary single stage HDH desalination process

The heating phase discussed requires a large thermal load whose magnitude monotonically increases with escalating values of air volumetric flow rate. As a result it is responsible for the majority of the thermal energy requirements of the HDH desalination process investigated. Thus, for the process from Point 1 to Point 2 the sensible heat transfer is calculated with the following equation [32]:

$$\dot{Q}_{sens} = \dot{Q}_{1-2} = \dot{m}_a c_{p_a} (T_2 - T_1) \tag{3.28}$$

Even with no change in the humidity ratio during this heating process, the moist air does contain superheated water vapor, in addition to its other constituent gases. Technically, the dry bulb temperature is an average value of the multicomponent air. However, it is assumed that this is known *a priori* and no

additional temperature calculations are necessary. The dry bulb temperature used with another psychrometric property will effectively fix the thermodynamic state of a particular process point.

Now in this case, air is assumed to be comprised only of dry air and water vapor (cf. §3.2, 3.3). Therefore, its specific heat must include both species and is defined as [32]:

$$c_{p_a} = c_{p_{da}} + \omega c_{p_w} \tag{3.29}$$

One of the most useful features of the psychrometric chart, as shown in Figure 3.4.1, is that properties for all pertinent species (e.g. dry air, water vapor) are incorporated into the calculations used to generate the chart itself. Enthalpy values extracted from the psychrometric chart, for example, facilitate accurate energy and heat transfer calculations. Cognizant that accuracy may be compromised when visually evaluating terms from a chart or nomograph, process calculations were executed with specialized HVAC software. HD PsyChart Suite Professional 7.3™ [38], a software package with the ability to generate detailed process reports and psychrometric diagrams (e.g. Figure 3.4.1), was used for this purpose.

The simultaneous heat and mass transfer exchange between air and water during the humidification process is represented from Points 2 -3 on Figure 3.4.1. This process is of particular importance since the actual desalination occurs during this part of the HDH cycle. Process air in the humidification chambers comes into direct contact with a thin film of water as it is forced through the wet evaporative media (Figure 3.4.2). The two different interacting species, each at a particular thermodynamic state, will seek to establish thermodynamic and chemical equilibrium. Non-saturated air at a higher temperature than the water film on the CEM will attempt to establish thermal equilibrium and a saturation state, i.e. $\phi = 100\%$ (cf. §3.2). The large wetted surface area of the CELdek® media, analogous to having a very long water sump in the adiabatic saturator, facilitates air saturation and cooling. This process is discussed in greater detail in the following paragraphs.

There are several methods to analyze and explain the mass transfer mechanics of the air and water interaction diagrammatically illustrated in Figure 3.4.2. Let us examine the relationship between

concentration, e.g. mole fraction of water vapor x_w, and its partial pressure. Heat energy from the process air is transferred to the water upon direct contact. The low vapor pressure water on the surface evaporates into the moving air stream. In general, the direction of mass diffusion occurs from regions of high to low concentration or partial pressure. In this case, air that is further detached from the wet evaporative media will not contain as much water vapor as air that is in close proximity or infinitesimally near the water film. Thus, the concentration of water vapor is greater near the surface of the water film ($y = surf^+$) and decreases in the positive y-direction, e.g. $x_{w,\infty} < x_{w,surf^+}$. This concentration difference establishes a gradient that drives the transfer of water vapor into the moving air stream.

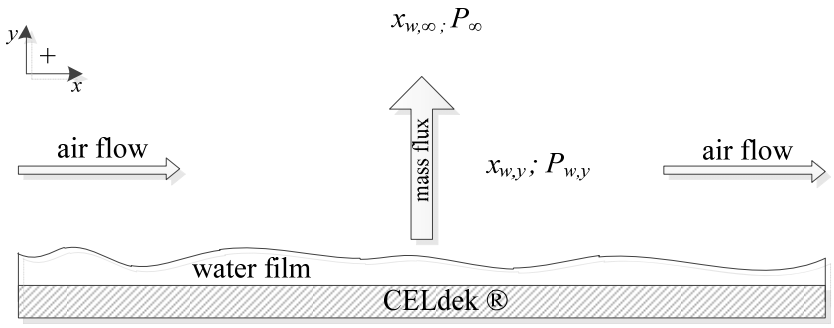

Figure 3.4.2: Air flow and water vapor concentration over wetted CELdek® surface.

Let us also consider the principle that mass transfer occurs in the direction of decreasing partial pressure. The ratio of partial to total pressure of a species is directly related to its mole fraction via the following relationship (details of this and other concentration relationships are found in Appendix A):

$$\frac{P_i}{P} = x_i \tag{A.26}$$

Solving for the partial pressure yields:

$$P_i = x_i P \tag{3.30}$$

Examination of these relationships reveals that the partial pressure is proportional to its mole fraction, assuming the total pressure P remains constant - a reasonable assumption. The region of interest is in close proximity to the air-water interface. Hence, the total pressure will exhibit a negligible change with respect to elevation. Since the value of x_w decreases in the positive y direction, so will the partial pressure of the water vapor in the same direction:

$$P_{w,\infty} < P_{w,y<\infty} \tag{3.31}$$

Consequently, water vapor mass transport will be directed into the moving air stream, i.e. in the direction of decreasing water vapor partial pressure.

We have established that concentration and partial pressure gradients will drive water vapor mass transport into the moving air. The heat transfer process will now be examined in more detail. Consider the control volume shown in Figure 3.4.3, illustrating the heat and mass transfer interactions during the humidification process. The total heat transfer between the air and water film includes a sensible and evaporative (latent) component. The evaporative component is due to the mass exchange of water vapor to the air. Sensible heat transfer is due to changes in dry-bulb temperature only – there is no humidity or vaporization term in its equation.

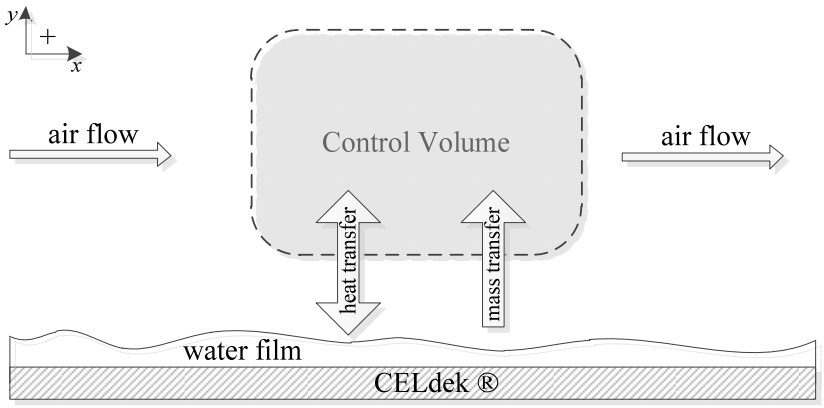

Figure 3.4.3: Thermodynamic control volume for air flow over wetted surface.

Sensible heat is converted to latent heat by virtue of water evaporation during the simultaneous heat-mass exchange in the humidification chambers. As a result, some of the sensible heat is transported back into the air stream as latent heat in the water vapor. Also, the energy transfer due to the enthalpy exchange is of greater magnitude than the radiative heat transfer from the electrical heating elements in the system. Hence, radiation heat transfer effects are not considered.

The total, sensible and latent heat transfer equations, summarized by (3.32)-(3.34) respectively, are defined via the conservation of energy and mass governing equations, (3.19) and (3.21). The subscripts of the following equations coincide with the process shown in Figure 3.4.1:

$$\dot{Q}_{total} = \dot{Q}_{sensible} + \dot{Q}_{latent} \tag{3.32}$$

$$\dot{Q}_{sensible} = \dot{m}_a c_{p_a} (T_2 - T_1) \tag{3.33}$$

$$\dot{Q}_{latent} = \dot{m}_a (\omega_3 - \omega_2) h_{fg_{2-3}} \tag{3.34}$$

All heat load and psychrometric calculations were done with the specialized software used for the constant humidity heating phase. It is prudent, however, to review the fundamental energy equations of the HDH process.

The dehumidification stage of the HDH cycle follows similar heat transfer mechanics as its previously discussed counterpart. Condensate recovery from the air occurs by cooling the air to the ambient dew-point temperature or below. A finned, cross-flow heat exchanger used as a condenser is supplied with low temperature water by a cooling tower. Air is dehumidified as it flows through the heat exchanger and the extracted condensate is collected in this final stage. Thermal heat load calculations for the heat exchanger were done with proprietary software supplied by the manufacturer, USA Coil and Air [39]. Use of the software facilitated, expedited and improved the accuracy of heat transfer calculations for the heat exchanger/condenser. Technical details and schematics of all the experimental system's components are found in the following chapter.

Chapter 4: Experimental Facility and Procedure

An experimental test unit was constructed to examine the HDH desalination process of a previous feasibility study by the author. To characterize the desalination process, a series of experiments were conducted in a facility that closely simulated the theoretical process. To accomplish this task, an experimental facility was designed to study the production capabilities of an HVAC based HDH desalination plant. Air volumetric flow rate, the thickness of the evaporative media and salt content of the desalinated water were the main factors of interest. This chapter focuses on the experimental setup and procedures used in this investigation.

4.1 Experimental Setup

The experimental facility was composed of the following main components:

1. centrifugal fan
2. ducting system
3. electric heaters
4. humidification chamber
5. cooling tower-pump circuit
6. condenser
7. data acquisition system

The experimental unit was designed to be employed in a water-scarce, decentralized location limited in technical personnel. It features a modular design that allows easy system modification, particularly when incorporating additional heating and humidification stages. This type of design also facilitates inspections and any repairs to system components as needed. The experimental setup is

diagrammatically shown in Figure 4.1.1. The following sections will be used to describe the design, functionality and features of each of the system's main components.

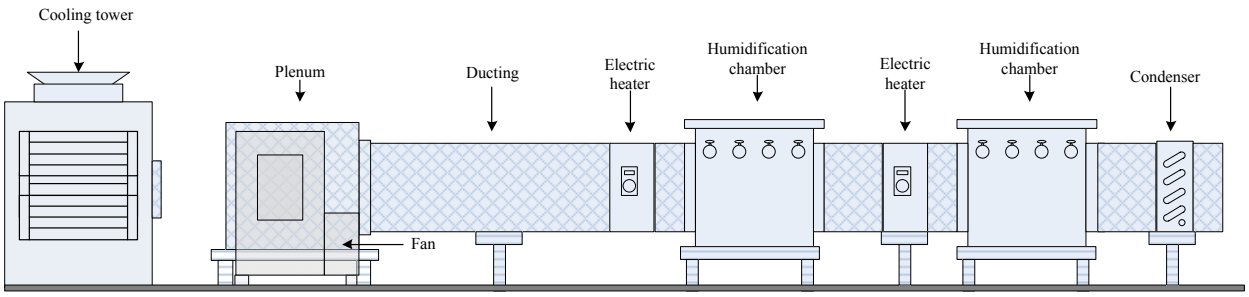

Figure 4.1.1: Profile view of experimental setup

THE REST OF THIS PAGE LEFT INTENTIONALLY BLANK

4.1.1 Centrifugal fan

A Greenheck BISW Series 21 Class II industrial centrifugal fan (cf. Figure 4.1.1.1) was used to provide the air volume flow for the process. The fan was belt driven by a three phase, 460 V, 3.0 HP motor. Fan speed was controlled to vary the volumetric flow rate through the system using a Dayton GS2-43P0 variable frequency drive. A variable frequency drive provided superior control over the air flow in the system by minimizing variation in the flow once the desired frequency was selected and inputted into the controller.

The volume flow rates for the system were calibrated with a hot-wire anemometer and a manometer. The discharge duct was subdivided into a grid of 81, 2.0" x 2.0" squares using thin wire. The fan speed was then varied by using the variable frequency drive in 5.0 Hz increments. A hot-wire anemometer was used to probe the center of each grid square and determine the local air velocity corresponding to a particular frequency. Next, the pressure drop across the condenser was measured with a Dwyer manometer. The condenser also measured the pressure drop located at the discharge end of the system. A correlation between volume flow rate and pressure drop independent of any obstructions upstream of the condenser (such as evaporative media in the humidification chambers) was developed and a calibration curve generated. The variable frequency drive could be adjusted during an experiment until the pressure drop across the condenser corresponded to the desired air volume flow rate. The fan calibration curve is shown in Figure 4.1.1.2.

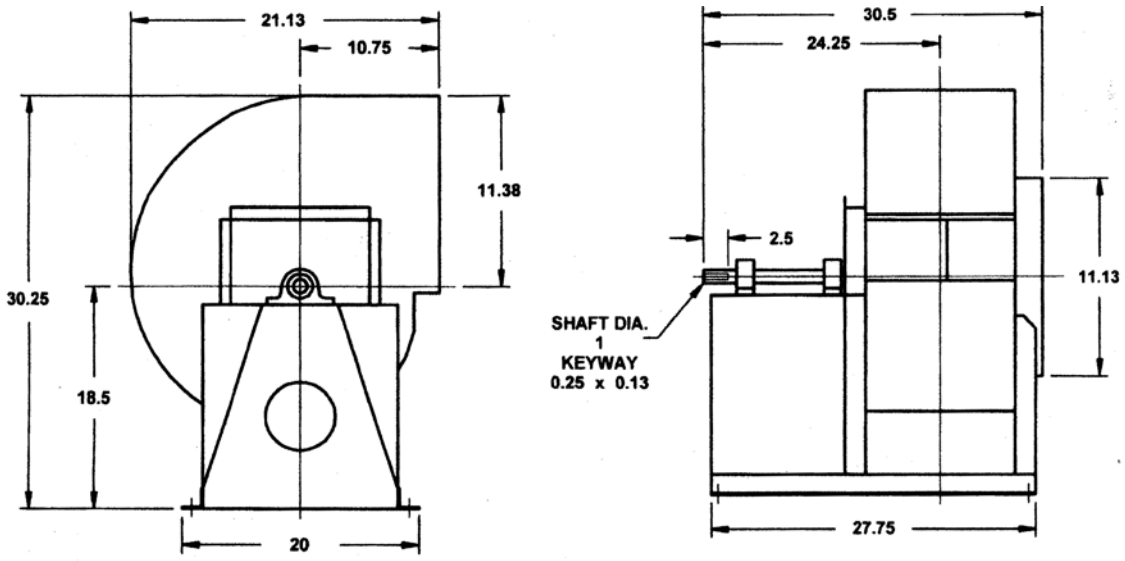

Figure 4.1.1.1: Lateral & rear views system centrifugal fan (© Greenheck Inc.)

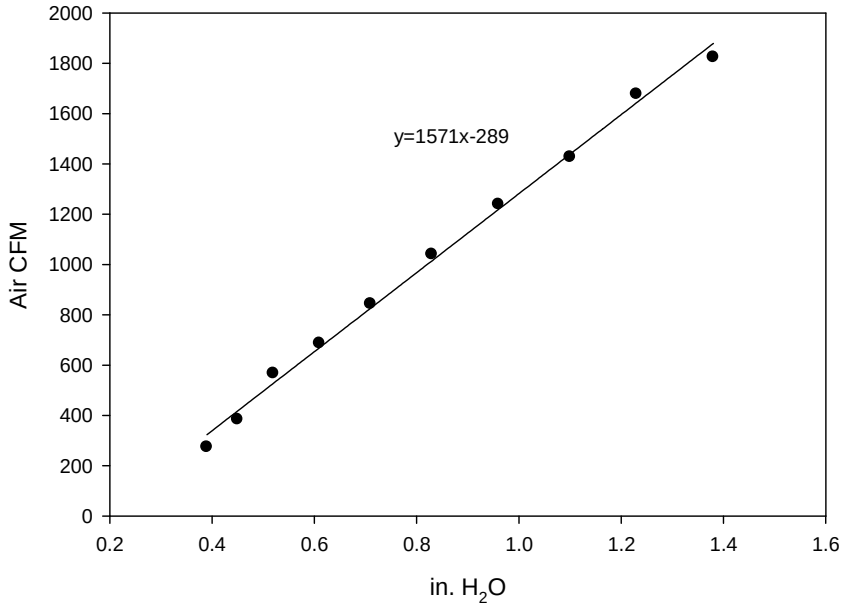

Figure 4.1.1.2: Condenser air side pressure drop versus volume flow rate

4.1.2 Ducting system

The ducting system for the test facility was comprised of several 18.0” x 18.0” ducting sections with 1.0” flanges and a plenum located at the discharge side of the centrifugal fan. The ducting and the plenum was made of 16-gauge aluminum sheet metal. The high internal static pressures required that heavier gage sheet metal be used to prevent any deformation of the ducting during system operation.

Installation of a plenum between the discharge side of the fan and the air delivery system was necessary to obtain fully developed flow while avoiding complications inherent to a long expansion section. This was the most cost effective and viable option for distributing air into the ducting system. The air from the centrifugal fan was discharged directly into the plenum constructed from the same gauge sheet metal as the rest of the ducts. The air was pressurized and released directly into an 18.0” x 18.0” ducting section three hydraulic diameters long to allow the flow to fully develop before passing through the initial heating stage.

Rectangular 2.0” x 3.0” baffles were installed on the interior of the ducting system in locations upstream of the electric heaters. Thermocouples were situated behind the baffles to provide shielding thus mitigating radiation effects on temperature measurements. Moreover, the baffles provided a convenient means of mixing the air, improving heat distribution, after each of the heating stages. All sections of the ducting system were bolted and sealed with Ductmate™ to minimize leaks.

4.1.3 Electric heaters

The heat load for each heating process was supplied by a Trane™ 460 V, three-phase, 18 kW electric duct heater. Temperature for the duct heaters was controlled by a TE-6000 temperature element and a System 350 ™ A-350P electronic proportional plus integral temperature control – both manufactured by Johnson Controls Inc. The duct heaters were manufactured to the same dimensions as the system ducting (18.0” x 18.0”) and were secured to the ducts with flanged connections.

The theoretical plant design used cross-flow heat exchangers to provide the heat loads as opposed to the electric duct heaters. Conceivably the heat stored by a salinity-gradient solar pond could be used to provide the heat loads used to increase air temperature. The stored energy would be used to heat water on the liquid side of the cross-flow heat exchanger. Air could then be preheated before entering the humidification phase using this thermal energy (cf. §3.4). However, laboratory setup and the lack of a readily available source of hot water (to simulate a solar pond) restricted the experiment setup to the use of electric heaters to provide the necessary thermal loads.

4.1.4 Humidification Chambers

The humidification processes were carried out in custom designed humidification chambers, or evaporators[6], completely enclosing the evaporative media, water lines, support beams, sump and temperature sensors. Access to the interior of each chamber was done by removing a top cover that included a weather seal that would minimize air leaks during system operation. The chambers were designed of the same gauge sheet metal as the rest of the ducting system and painted with a corrosion deterrent paint. Each humidification chamber accommodated up to 16.0" of CELdek® 7060-15 evaporative media. The media was supported above a sump by removable horizontal beams. Each chamber was fitted with four individually regulated water lines situated directly above each section of evaporative media as well as a drain at the bottom of the 3.0" deep sump. A hose connected each humidification chamber to a dedicated PVC drainage pipe system, preventing sump overflow and, more importantly, any water from reaching the electric heating coils. The desalination pilot plant PVC drain system emptied into the laboratory drainage system.

The humidification chamber internal water lines were made of 20.0" long, 0.5" diameter PVC pipe with 1/16" diameter holes spaced 0.5" apart and running along the length of each line in three parallel rows. Each water line was individually regulated by a PVC ball valve situated on the outside

[6] The terms *humidification chamber* and *evaporator* are used synonymously in this context.

wall of the evaporator. Each chamber was connected to a PVC water distribution manifold by 0.5" diameter flexible hose. The water supply could also be regulated by a series of PVC ball valves integrated into the manifold itself. The system of redundant valves permitted excellent water flow control to the humidification chambers and immediate water supply shut-off in case of a water leak or pipe damage

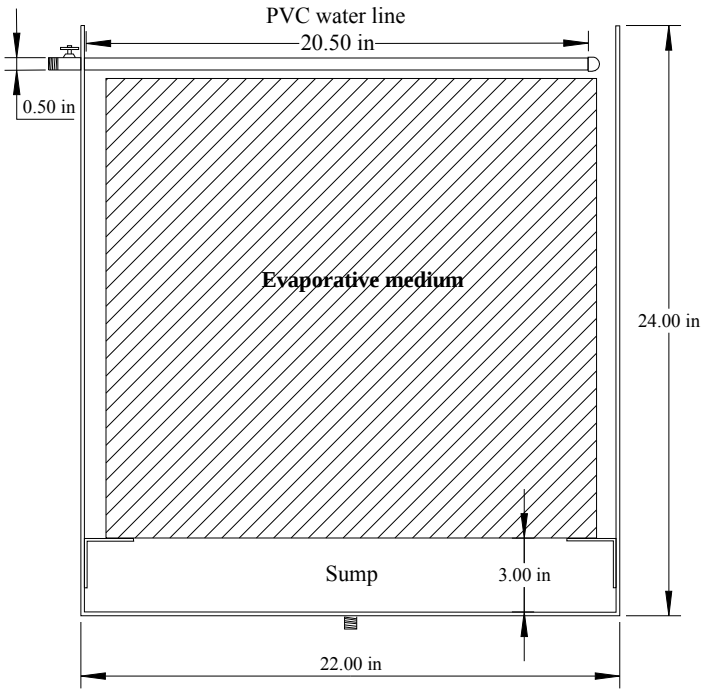

Figure 4.1.4.1: Cross section view of humidification chamber

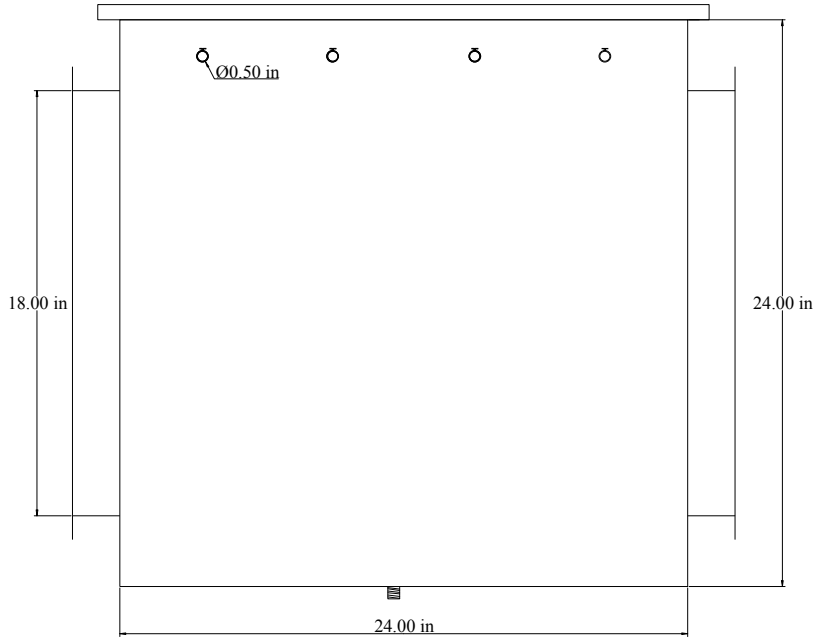

(a)

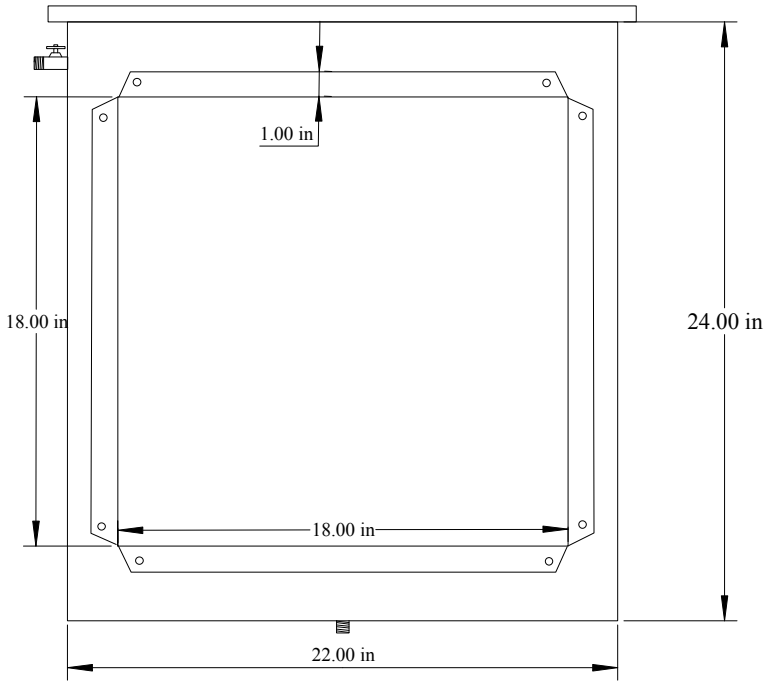

(b)

Figure 4.1.4.2: (a) Lateral and (b) front views of humidification chamber

4.1.5 Cooling tower-pump circuit

A closed-loop cooling tower-pump circuit circulated cooling water through the condenser. A Baltimore Air Coil cooling tower supplied the condenser with water at a sufficiently low temperature to cool the air to the ambient dew-point temperature. The water at the condenser inlet was extracted from the cooling tower sump. The return water from the condenser, now at a higher temperature after the condensation process, was recirculated to the cooling tower's gravity-fed basin for cooling. A Bell & Gossett Series 1535 close coupled centrifugal pump maintained an average of 12.9 gpm circulating through the condenser-cooling tower circuit. The flow rate was adjusted with an inline threaded brass globe valve and measured with a venturi meter. The necessary cooling water flow rate was determined using proprietary software from the heat exchanger manufacturer by specifying air inlet and exit temperatures and volumetric flow rate. To minimize experimental variables, the water flow rate selected corresponded to the maximum experiment air volume flow and kept constant for all experiments. Further details pertaining to experimental procedures will be provided in §4.2.

4.1.6 Condenser

The water vapor in the air was removed from the air through condensation. Cooling the air to the ambient dew-point temperature initiated the necessary condensation process. A USA Coil & Air (model number CW58DN01801800000R) fin-tube water to air heat exchanger was used as the condenser for the system. This component had a flanged, galvanized steel casing and was secured to the rest of the ducting system by the flanges and sealed with DuctMate™ to minimize air leaks. The heat exchanger tubes and fins were made of copper and aluminum, respectively, four rows deep, 13 fins per inch (fpi) with fin height and length of 18.0". Six 0.25" holes were drilled at the bottom of the heat exchanger to allow the condensate forming on the fins and tubes to drain. The condensate was collected by a tank placed directly beneath the condenser which was emptied during or at the conclusion of an

experiment run, as necessary. The total condensate collected was measured and a sample from each run was collected and used for conductivity testing. More details will follow in the section discussing experimental procedures.

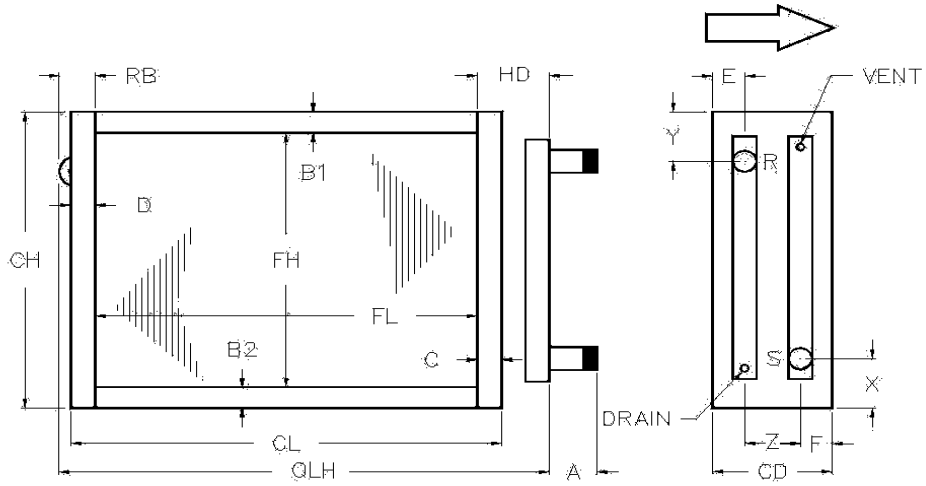

Figure 4.1.6.1: Front and lateral views of finned, cross-flow heat exchanger/condenser [39]

4.1.7 Data acquisition system

A National Instruments model NI™ SCXI-1000 chassis and two eight-channel NI™ SCXI-1112 thermocouple input modules comprised the data acquisition system. The chassis provided a shielded enclosure for the input module and was compatible with LabVIEW™ software. The input module provided instrument amplification, onboard calibration reference and cold-junction compensation per channel. A Virtual Instrument (VI) was created for use in LabVIEW™ to simultaneously monitor and record temperature data.

Twelve channels, six per module, collected temperature data at different system locations. Type K (chromel-alumel) thermocouples were used for all temperature measurements in the experiment facility. Six thermopiles collected average dry-bulb temperature data at selected system locations. Each thermopile was composed of eight parallel connected thermocouples, evenly distributed around the

perimeter of the duct. The parallel connection provided an average temperature measurement at each designated location while occupying a single input channel. Two thermocouples were situated in the cooling tower. One thermocouple was placed in the sump, measuring the inlet water temperature into the condenser. The cooling tower's gravity feed basin received the return water from the condenser. A second thermocouple was placed at the feed basin to measure the exit water temperature from the condenser. Finally, a thermocouple measuring wet-bulb temperature was placed at the inlet and exit of both humidification chambers. The thermocouple beads were wrapped with a 100% cotton mesh. The mesh self-saturated with water from an 8.0 fl. oz. open plastic container secured to the inlet and exit of each humidification chamber. A 1/8" flexible plastic tube connected to each chamber's main water supply line provided a constant flow of water to each container. Each container was modified with an overflow tube that routed excess water into the chamber's water sump.

4.2 Experimental Procedure

The purpose of this investigation was to examine the functional and desalination capabilities of an HVAC based HDH test unit. The experimental unit was designed to replicate an ideal HDH cycle as described in Cornejo at al. [5]. Different system parameters believed to affect the desalination process as a whole, were varied and examined. In order investigate the actual HVAC-HDH desalination process, a set of experiments were designed and executed. The following sections outline the rationale behind the design of the test matrices implemented in this investigation.

4.2.1 Test Matrices

The types of experiments conducted in this investigation were dictated by the parameters that were believed to have the most significant effect on the system's capacity to desalinate water. The system parameters of interest that could be varied with the test unit included the maximum target air temperature, air volume flow rate, water flow rate to the condenser, evaporative media thickness and

number of heating-humidification stages. There were a total of five parameters that were included into the experiments developed.

When considering experimental variables of this investigation, the heating process target air temperature and the water volume flow rate to the condenser were kept constant. The target air temperature was kept constant for all experiments to establish a common metric and more readily compare the system desalination capabilities amongst the two main types of experiments. Cooling water flow rate to the condenser was kept constant to eliminate a variable parameter. Furthermore:

- The air target air temperature of 132° F was constrained by the electric heater capacity. The air temperature in the feasibility study by Cornejo et al. [5] ranged from 155 – 165 °F. However, the theoretical unit assumed thermal energy would be supplied by a salinity gradient solar pond; the lower convective zone at a nominal 185°F [24] for summer operation. Moreover, the theoretical study used water to air fin-tube heat exchangers allowing higher heat transfer rates.
- Cooling water volume flow rate was constrained by condenser's capacity to lower the process air temperature to the ambient dew-point with the specified system operating parameters. The fin-tube water to air heat exchanger capacity was calculated with software from the heat exchanger manufacturer [39].
- Water flow rate into the humidification chambers was not measured. The evaporators were not instrumented to measure flow or temperature. Water flow to the evaporators was kept constant. The estimated flow rate, evaluated by visual inspection before each test run, was assumed to keep the evaporative media fully wetted throughout each experiment.
- Each experiment lasted an average of 3.5 hours. Transient system operation was not in the temporal window of interest. Therefore, startup and shutdown times were not considered in this window. The recorded experiment time was within the system's steady-state operation.

Two different types of experiments were conducted. Type I, or single stage, experiments were characterized by a single heating- humidification and dehumidification process. Type II, or two-stage, experiments consisted of two heating-humidification processes and a final stage of air dehumidification. Both of these experiments were designed to collect quantitative data to be used for examining the desalination process in more detail. System operational parameters were kept uniform for both types of experiments. The key difference between the two is the number of heating-humidification stages. The experimental procedures will be substantiated upon in the following sections.

Type I Experiments

Type I experiments comprised half of the experimental work done in this study. These tests were designed to collect data in order to characterize the actual HDH desalination process. Type I experiments employed the most basic experimental system configuration, thus serving to establish a baseline with which Type II experiments could be compared. The air was subjected to only one heating-humidification process (i.e. one stage) followed by the condensation process. Tests were conducted at volume flow rates of 400, 600, 800 and 1000 CFM all with a heated target air temperature of 132 °F. Cooling water volume flow rate through the condenser was kept at 12.9 gpm at 66 °F. The evaporative medium in the humidification chamber was varied at 4.0", 8.0", 12.0" and 16.0" thicknesses for each tested air volumetric flow rate. The overall Type I experiment matrix is shown in Table 4.2.1.1.

Type II Experiments

The Type II experiments, which included an additional stage, comprised the rest of the experimental work of this investigation. A second heater and humidification chamber were used to accommodate for this additional stage. This second heating-humidification process allowed further water vapor mass transport to the air. The additional extracted condensate would increase the experimental system's desalination capacity. System output was compared to that generated by the

baseline Type I configuration. The 16.0" CEM thickness was not tested in Type II experiments due to time and laboratory constraints. However, system desalination capacity was predicted based on the experimental data acquired. All system operational and experimental parameters remained unchanged for Type II experiments (cf. §4.2.1, *Type I Experiments*). The experiment matrix for Type II experiments is shown in Table 4.2.1.2.

Table 4.2.1.1: Test matrix for Type I experiments

Air Volume Flow Rate $\dot{V}_{air}$ (CFM)	CEM Thickness (in.)	Test Number
400	4.0	1
	8.0	2
	12.0	3
	16.0	4
600	4.0	5
	8.0	6
	12.0	7
	16.0	8
800	4.0	9
	8.0	10
	12.0	11
	16.0	12
1000	4.0	13
	8.0	14
	12.0	15
	16.0	16

Table 4.2.1.2: Test matrix for Type II experiments

Air Volume Flow Rate $\dot{V}_{air}$ (CFM)	CEM Thickness (in.)	Test Number
400	4.0	1
	8.0	2
	12.0	3
600	4.0	4
	8.0	5
	12.0	6
800	4.0	7
	8.0	8
	12.0	9
1000	4.0	10
	8.0	11
	12.0	12

4.2.2 Experiment Procedures

The operating procedure for all the experiments was the same for all the experiments conducted. The standard operating procedures followed for each one of the experiments performed are detailed in the sections that follow.

System Setup

1. Ambient air temperature conditions are measured using a sling psychrometer. Deionized water is used to saturate the wick on the thermometer to be used for measurement of the wet-bulb temperature.
2. The system set up procedure begins with a routine visual inspection of all the pilot plant's components. The cooling tower is checked for proper functioning of the fan and for any leaks from the sump.
3. The centrifugal pump driving the condenser-cooling tower circuit is checked for proper operation by allowing it to run briefly. Verify that the return water from the condenser is feeding correctly into the cooling tower reservoir. Adjustments are made to ensure proper amount of flow.

4. Both humidification chambers are inspected by removing the top covers. All the external feed hoses to each chamber and the drain hose are checked for leaks. Internal water lines are inspected for leaks and clots. The miniature sump and wet-bulb thermocouple arrangement in each chamber is inspected for damage. Finally, the chamber drain and sump are inspected for any debris that may have dislodged from the evaporative medium from a previous test run. The sump and drain are cleared if any is found.
5. The glass collection tank below the condenser is emptied of any contents and thoroughly cleaned. The tank is then placed below the condenser for condensate collection during the experiment. An alternate storage tank is kept on hand in the event that the tank in use fills to capacity during a test run. The empty tank is exchanged immediately with the full one during an experiment, if necessary, to minimize any condensate loss. Last, the condenser is checked for any leaks from the hose fittings.

System Startup

System startup begins after all visual inspection of the pilot plant has been completed and any necessary adjustments or repairs have been made. The following procedure is also standard for both types of experiments.

1. The computer terminal and data acquisition system are turned on. The LabVIEW™ virtual instrument panel is accessed and a data file where all temperature measurements will be recorded is created. The air temperature readings from the thermocouples and thermopiles are compared against the sling psychrometer measurement. This is done to verify that the sensors are functioning properly.
2. Evaporative media is loaded into the humidification chamber(s) in accordance with the experiment type and thickness being tested. Any internal water lines in the humidification chambers not being used are completely closed with their bypass valves. If a humidification

chamber is not used (i.e. Type II experiments) then its water supply is cut off by closing the bypass valve at the chamber manifold. This prevents extra moisture from entering the air as it passes the second, inactive evaporator.

3. The main water supply for the humidification chambers is opened. The valve for the water line above the evaporative medium is then opened to allow the medium to be fully wetted before starting the experiment. Since the flow rate to each of these lines is not measured, saturation of the media is done by visual and tactile inspection. The water is allowed to saturate the CELdek® for fifteen minutes as a standard. This amount of time was estimated to be enough for complete saturation. This time is also used to verify that the draining system in each humidification chamber is functioning properly. Once this step has been completed, the humidification chamber is sealed and a counter weight is placed on top of the cover to ensure it stays in place through the duration of the experiment. A counter weight is also placed on the cover of the inactive humidification chamber for the same purpose.
4. The supply fan is activated once the system has been sealed. The manometer installed on the condenser is used to determine the air volume flow rate of the system using the calibration curve in Figure 4.1.1.2. The variable frequency drive is used to adjust the speed of the supply fan as needed in order to obtain the designated flow rate for the experiment. The manometer is observed closely until there is no fluctuation in the pressure drop, ensuring a steady flow.
5. One or both electric heaters are activated for Type I or Type II experiments, respectively. The electric power supply for each heater is turned on. Next, the target air temperature is dialed in on the PID control module on each heater. All experiments used a common heating phase target air temperature of 132 °F. The actual air temperature is then monitored on the computer terminal. The air is allowed to reach its steady state temperature (approx. 30-45 min) before the experiment is begun. Transient system operation was not of interest in this investigation.

6. The cooling tower-condenser circuit is the last system component that is engaged. Both the cooling tower fan and the centrifugal pump are turned on. A globe valve on the discharge side of the pump is used to regulate the water volume flow rate, measured by a venturi meter. The valve is set to allow 12.9 gpm of water to flow in the circuit. However, the pressure drop across the venturi is always checked to ensure a constant value of water flow rate. Any adjustments can be made using the globe valve.
7. Temperature readings are examined briefly on the computer terminal to verify that all thermopiles and thermocouples are functional before data recording begins. Once this has been verified, the experiment is begun by initiating the data logger on the VI designed for use in LabVIEW™. Data is recorded for the duration of the experiment.

System Shutdown

1. Once the experiment runs for the designated amount of time, the data logger is turned off to stop recording. The file is saved once more to ensure all data was captured.
2. The water collection bin below the condenser is removed and set to one side. A second collection bin is set in its place to collect additional condensate while the system is shut and cooled down. This additional condensate is not considered in the results as it is collected outside the temporal domain of interest. This condensate is disposed of once the system has been completely shut down.
3. The electric heaters are turned off. The control module is set to zero for each of the heaters used. It is important to note that the heaters must be turned off while the supply fan is still on. Turning off the supply fan while the heaters are still on can possibly cause a thermal overload on the heating elements and damage them permanently. The electric power supply for each heater is shut off. It is essential that the high voltage power supplies are off at the end of each experiment.
4. The cooling tower fan and centrifugal pump are shut off.

5. The supply fan is turned off by dialing down the VFD to zero hertz and shutting down the main electric power supply to the fan.
6. The bypass valves to the humidification chambers are closed and the water in the sump is allowed to drain out. The main water supply valve for the humidification chambers is also closed.
7. The amount of water in the collection bin is recorded. A 30 mL sample of this water is taken and stored for conductivity testing. The conductivity of the water will be the metric used for evaluating the salt content of the desalinated water.
8. The conductance of the 30 mL sample collected at the completion of each experiment is measured with an OMEGA™ model CDH-5022, conductivity meter and the results recorded

The standard operating procedure is repeated for each of the experiments conducted. It is essential that the experiment setup be inspected thoroughly before the beginning of a new experiment. Each experiment conducted subjected the pilot plant and its components to high air volumetric flow rates at high temperatures for relatively extended time periods. The cooling-tower-pump circuit operated at a modest flow rate in order to cool the air below its ambient dew point temperature. As a result, the entire system needs to be inspected before each test run to ensure proper functionality of all components.

Chapter 5: Data Reduction and Analysis Methodology

This study explored the functional and production capabilities of a two stage, HVAC based HDH desalination system. The experiments conducted were limited in their scope. They were strictly aimed at assessing the experimental system's production capacity with varying configurations. Psychrometric and operational parameters of the experimental setup were quantified by air and water temperature measurements at predetermined system locations. Process airflow and water volume flow on the fluid side of the cooling circuit were used in conjunction with temperature data to establish system operational settings. This chapter will discuss the data reduction process, the logic upon which the analysis is based and outline the analysis undertaken to develop the results and empirical relationships presented in the following chapter. Parametric analysis for system optimization is beyond the scope of this investigation. System modifications based on the open literature will certainly be recommended, though they will not be developed in this study.

As discussed in the previous chapter, the experimental work was divided into two main categories, Types I and II, both aimed at exploring the relationship between system performance and variation of selected operating parameters. Understanding the functional characteristics of the experimental unit was fundamental in establishing a range of operational conditions at which the system will perform satisfactorily in its current configuration. The reduced data and analysis are used to define empirical equations describing system production capability and overall performance.

5.1 Temperature data reduction procedure

Air temperature data accounted for the largest portion of all experimental data collected. Temperature data were used to generate (a) psychrometric and thermodynamic property values at each principal state of the HDH process, (b) heat load magnitudes, (c) performance ratios and

(d) psychrometric process diagrams for each experiment. Evidently, reducing this data to tractable levels was essential for the analysis of each experiment. The temperature data reduction procedure is explained in this section

The data acquisition module and virtual instrument (VI) for use in LabView™ were configured to record temperature measurements in time intervals of 0.01 seconds, i.e. $\Delta t = 0.01\text{s}$. An experiment for each system configuration, as described by the test matrices in Chapter 4, had a collective run time of approximately 3.5 hours. The temporal window of interest, however, is limited to the thermodynamic steady-state configuration of the system. Inspection of the raw data reveals small transient temperature fluctuations during steady state system operation. The mean value of the temperature is insensitive to these small fluctuations, thus, discretization of temperature data to such a small time interval was not necessary. Each large data file was filtered to include temperature measurements at five minute intervals (Δt=300s) considerably reducing each experiment data set to 45 samples at a maximum. Frequency distributions generated with samples taken from the parent populations for each experiment type were used to determine the data distribution type. Figure 5.1.1 shows histograms for temperature data from a Type I and II experiment; frequency distributions for temperature measurements from all experiments conducted were similar to those shown in Figure 5.1.1. The histograms shown reflect air dry-bulb temperature entering the condenser – i.e. the final condensation process before air is exhausted into the atmosphere (cf. Figure 5.1.1).

Air temperature measurements during steady state operation produced highly localized values. Suitable bin widths within a selected temperature range reveal that the data follow a normal trend. Because type K thermocouples have a maximum accuracy of 0.1°F at these temperatures, statistical analysis results were rounded to the nearest degree for all system calculations. The accuracy of this thermocouple type is well suited for macro-scale, steady-state analysis of the system. Moreover, at 0.1°F accuracy, the histograms imply that the measurements are highly repeatable with the instrumentation.

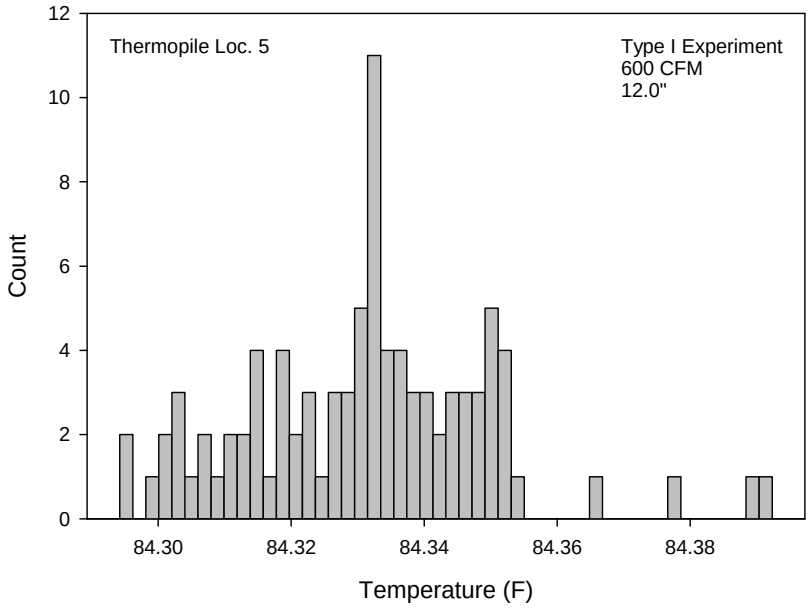

(a)

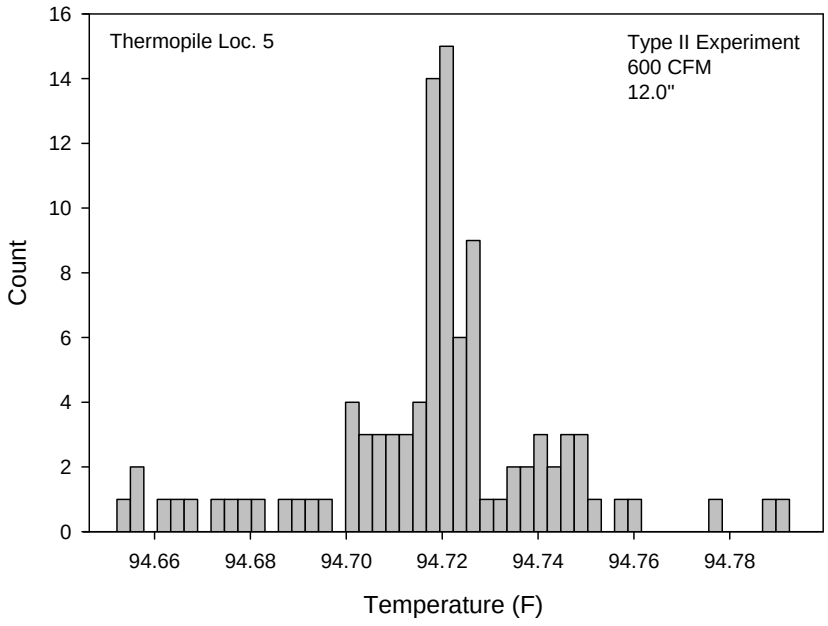

(b)

Figure 5.1.1: Histograms of sample temperature data from (a) Type I and (b) Type II experiments

Assuming the data follow a Gaussian profile within the steady-state temporal window, the random component of the uncertainty corresponding to the temperature was computed with the standard error of the sample, or standard deviation of the mean SDOM, as defined by:

$$\sigma_{\bar{T}} = \frac{\sigma_T}{\sqrt{N}} \tag{5.1}$$

where σ_T defines the sample standard deviation and N is the number of measured values. The standard deviation is expressed as:

$$\sigma_T = \sqrt{\frac{1}{N-1}\sum\left(T_i - \bar{T}\right)^2} \tag{5.2}$$

where $T_i - \bar{T}$ represents the difference between a measured value of temperature T_i and the sample mean defined by:

$$\bar{T} = \frac{1}{N}\sum_{i=1}^{N} T_i \tag{5.3}$$

For a 95% confidence interval about the sample mean, the corresponding bounds of uncertainty can be expressed in terms of the standard error as $u_p = \pm 2\sigma_{\bar{T}}$ [40]. In this particular example, $\bar{T}$ can be interpreted as the expected mean value of the temperature at a specified system location, while u_p represents a precision estimate associated with the average temperature.

5.2 Analysis Methods for Type I and Type II Experiments

As previously mentioned, Type I and II experiments share the same end purpose – to determine the production and performance capabilities with both configurations of the test unit. The difference between both types of experiments lies in the system configuration employed. Type I experiments use a single stage configuration, i.e. a single heating and humidification process, as opposed to two stages used for Type II experiments. The experimental variables for both experiment types are identical as is explained in §4.2.1. Type I experiment results establish a baseline reference for Type II

experimentation. Ideally, a multiple stage system with three or more stages would have been tested in order to gain better insight on multi- stage system performance. Much can still be learned about multi-stage system performance from the Type II experiments.

This section will be divided into five parts, each one dedicated to the discussion of a specific area of analysis. Collectively, this analysis will allow us to understand the HDH process investigated by providing insight about its (a) production capacity, (b) performance efficiency and (c) basic entropic characteristics.

5.2.1 Desalinated water production

One of the primary quantities of interest for this, and any desalination system, is the amount of fresh water production. Considering that this is an experimental prototype unit, desalinated water production data is especially important as it establishes a baseline for the system's production capacity in its most basic configurations. The amount of desalinated water produced by any particular system is synchronously reported with the amount of energy expended to produce it – and this HVAC-HDH system is no exception. Energy expenditure and performance measures for this experimental unit will be discussed in another section.

As discussed in the previous chapter, water was collected in a glass storage tank and measured after the completion of each experiment. Water collection data was recorded for each experiment configuration defined in the test matrices (cf. §4.2.1). Empirical relationships for predicting system water production for various configurations were defined. These empirical relationships not only served as practical predictive tools but were versatile for defining numerical routines for system analysis, as discussed in the following section.

The production capacity of a desalination system is irrelevant if the water produced is of poor quality. Thus, water quality is of paramount importance in desalination operations. Along with turbidity measurements, specific conductance is a common metric used for evaluating the quality of

water. The specific conductance (μS/cm or S/m) measures the ability of water to conduct an electrical current [41]. Elevated amounts of salts and suspended solids in a water sample will make it electrolytic in nature. Saline water thus exhibits high conductance values as opposed to highly pure water with low electrical conductivity. Table 5.2.1.1 lists conductance values for selected grades of water [42-44]. Conductivity measurements of samples collected from the test unit's water production were recorded after each experiment. A plot was generated using the recorded values.

Table 5.2.1.1: Specific conductance of different water types

Water grade	Specific Conductance (μS/cm)
Distilled water	0.5 - 3.0
Potable water	30 - 1500
Inland fresh water	150 - 500
Industrial water	≤ 10000
Brackish water	≈ 20000
Seawater	≥ 50000

5.2.2 CEM and the humidification process

The humidification process is of particular interest in this study due to the use of CEM in the evaporation chambers. A study by Dai and Zhang [25] uses honeycomb packing material in the humidifier of its single-stage solar desalination unit. Chafik [45] tested a CAOW, multiple stage HDH solar desalination system using CELdek® or GLASdek® with satisfactory results. However, studies varying the thickness of CELdek® 7060-15 in the evaporators of a CWOA, multiple stage, HDH desalination system were not found in the open literature. Investigating the effect of CEM thickness on fresh water production and overall system efficiency were main objectives of this study.

Frequently used in high efficiency evaporative cooling equipment, CEM is created by bonding together thin, chemically treated[7] corrugated sheets in vertical laminations. Airflow through the CEM generates low pressure drops due to the high intersection angle of the corrugations of adjacent sheets.

[7] The corrugated sheets are chemically treated to resist decay and enhance wicking [34]

Moreover, the 15° upward slope of the sheet corrugations in the direction of airflow promotes downward water flow, keeping more water at the air entry side, while preventing it from blowing out the exit side. This relatively small angle allows the air to run nearly parallel to the counter-flowing water film, enhancing water to air interfacial contact. Furthermore, the closely packed sheets of this evaporative medium provide a large amount of surface area – nearly 123 ft^2 of surface area per cubic foot - while delivering high saturation efficiency in the range of 65% to 100% for thicknesses of 6.0" to 24.0" respectively. Watt and Brown [34], the source of the preceding information, provide an extensive discussion of this evaporative media and its applications.

Water production was plotted against (a) air volumetric flow rate for varying thickness of corrugated evaporative media (CEM) and (b) evaporative media thickness for varying values of air volume flow rate. Two families of water production curves providing insight to the test system's production characteristics were generated. The plotted curves were examined in order to identify any trends or relationships between CEM thickness, water production and system air flow rate. A region where the system operates more satisfactorily was readily identified upon inspection of the plots and a set of operational parameters demarcating the preferred system operational region (PSOR) were defined. It is important to note that a parametric analysis of the humidification process was beyond the scope of this investigation. Therefore, a *preferred* system operational region was defined as opposed to a region of *optimum* operation.

A quadrilateral boundary enclosing the PSOR was defined on the water production curves by identifying the operating conditions where the system exhibits no appreciable change in water production. Visually inspecting the production curves to establish a preliminary "boundary" of satisfactory system operation was the initial step in defining the PSOR. System parameter values bounding the PSOR were determined by computing the water production at discrete values of CEM

thickness and air volume flow for system configurations within the preliminary boundary. A Mathcad™ routine employing the empirical correlations for system water output was used for this end.

The humidifier efficiency was computed as a means to determine the overall effectiveness of the humidification process without the need to explicitly calculate the saturation efficiency of the evaporative media. For air going through a humidification chamber, humidifier efficiency, as defined by several investigators [1, 26, 45], is expressed as:

$$\eta_h = 100\left(\frac{\omega_{out} - \omega_{in}}{\omega_{out,sat} - \omega_{in}}\right) \tag{5.4}$$

Nonetheless, in the interest of performing a comprehensive analysis, the saturation efficiency of the CEM was computed using the following equation defined in Watts and Brown [34]:

$$\varepsilon_{sat} = \frac{T_{in,db} - T_{exit,db}}{T_{in,db} - T_{in,wb}} \tag{5.5}$$

for air flow though the humidification chamber. The results of the calculations were compared against manufacturer provided saturation efficiency curves for CELdek® 7060-15.

No considerable deviations of calculated efficiency values from the manufacturer reported values were evident from the analysis. Moreover, the computed value of the saturation efficiency was a practical reference for understanding the experimental system's production trends and behavior. More specifically, it was useful for examining the relationship between actual and computed values[8] of water collection for a particular experiment.

[8] Water production values were computed with HD Psychart Suite Professional 7.3™ [38] using collected temperature data.

5.2.3 System Energy Calculations

Temperature and pressure data were recorded at selected system locations for every experiment configuration. Average values of the dry and wet bulb temperature measurements (cf. §5.1) were used with HD Psychart Suite Professional ™ 7.3 [38] to:

(a) calculate the psychrometric properties of the air

(b) calculate sensible and latent heat loads for each process

(c) compute fresh water production rates

(d) generate psychrometric process diagrams (e.g. Figure 3.4.1)

(e) compute the pressure drop & electrical output of the electric heaters

The psychrometric software uses the most current ASHRAE standards for computation of moist air properties and processes. The program required two moist air properties at a selected point to fully define the air's psychrometric properties. The software's psychrometric process calculator was used for accurately quantifying air sensible and latent heat loads, sensible heat ratios (SHR), changes in humidity ratio and water production rates for each experiment configuration. Computed water production values were compared against the actual experimental water collection data. Both values of water production compared favorably– within 0.1 – 0.5 lb_w/hr. Moreover, the psychrometric diagrams generated for each experiment were useful for identifying differences in the water production trends between both experiment types. System water production trends and their predictive empirical relationships will be substantiated upon in the following chapter.

Air side pressure drops from the primary system components were determined in order to compute an approximate value of the mechanical blower's energy expenditure. HD Psychart ™ software was used to compute both the pressure drop and electrical power consumption of each electrical heater. CEM pressure drop was determined using CELdek® 7060-15 performance curves

while USA Coil and Air's coil selection program and electronic catalogue [39] was used to compute condenser air-and fluid side pressure drops. Ducting major losses were approximated using a frictional loss nomograph [32]. The mechanical blower's power consumption was calculated with:

$$\dot{W}_{fan} = \dot{V}_{air} \gamma h \tag{5.6}$$

Conduit frictional losses and condenser fluid-side pressure drop were the main losses considered for pump shaft power calculations. Assuming 75% operational efficiency for the pump, the shaft power was computed with:

$$\dot{W}_{shaft} = \frac{\dot{W}_{hyd}}{\eta_{pump}} = \frac{\dot{V}_{water} \gamma h}{\eta_{pump}} \tag{5.7}$$

Technical information about the motor powering the cooling tower fan was not available. As a result, cooling tower power consumption was not considered in the analysis.

Component mechanical power consumption was small in comparison to the thermal loads required for air preheating - even with the system's most basic configuration. For this reason, emphasis was placed on thermal heat load computation while loss calculations were only intended for a conservative estimate of the unit's mechanical power requirements. However, the system's mechanical power consumption was loosely calculated in the interest of presenting a more comprehensive system analysis.

5.2.4 Assessment of System Performance Metrics

When it comes to defining the overall performance of a desalination system, there are several options. There is no real "gold" standard when it comes to defining a measure of performance for a water desalination system. This is primarily because each desalination system is different in configuration and efficiency parameters are generally very system specific. Two main efficiency parameters are commonly used in the open literature. The performance ratio, PR[9], used by Lu et al. [24], among other investigators, for assessing the "economy" of desalination is defined as the pounds of distillate per 1000 Btu of heat input [46, 47], i.e.:

$$PR \equiv 1{,}000\left(\frac{\dot{m}_{pw}}{\sum \dot{Q}_{in}}\right) \tag{5.8}$$

where $\sum \dot{Q}_{in}$, the sum of all "useful" heat input, is in Btu. Only the heat used for air preheating is considered in the $\sum \dot{Q}_{in}$ term, as this thermal load is used directly in the desalination process. The performance ratio was computed for each configuration of the experimental unit.

The gained output ratio (GOR) is another performance metric for water desalination systems that is widely used by several investigators in scholarly literature. The parameter can be interpreted as the effectiveness of water production and an index of the amount of system heat recovery [23]. The GOR is defined as:

$$GOR \equiv \frac{\dot{m}_{pw} h_{fg}}{\sum \dot{Q}_{in}} \tag{5.9}$$

where h_{fg} is calculated with the system operating pressure at saturation pressure. A GOR value of 1 means the system requires enough heat input to directly vaporize all produced water – i.e. no energy recovery - while GORs below 1.0, inherent of solar stills, are unfavorable and usually indicative of

[9] The subscript *pw* in the context of performance metrics refers to produced water, i.e. fresh water production of a system.

elevated system losses [48]. On average, typical solar stills have GORs below 0.5 [1] while values for air HDH cycles vary between 0.78 and 3.5 [23]. Conventional desalination processes such as MSF or MED have minimum GORs of 8 [1] while an ideal reversible HDH cycle has a GOR of 122 [23].

El-Agouz [26] defines a thermal efficiency parameter for his desalination unit which uses an air compressor for diffusing air bubbles through brackish water. The thermal efficiency used is defined almost identically to the GOR. The difference is found in the denominator, which sums the compressor power to the system heat input. An analogous term was defined for this investigation's test unit, the adjusted desalination thermal efficiency (ADTE; the term "adjusted" is due to the inclusion of the power input):

$$ADTE = \eta_{d,adj} \equiv 100\left(\frac{\dot{m}_{pw} h_{fg}}{\sum \dot{Q}_{in} + \sum \dot{W}_i}\right) \tag{5.10}$$

where the term $\sum \dot{W}_i$ includes the power required by the centrifugal pump and mechanical blower for overcoming system losses, as explained in §5.2.3.

The PR and GOR performance parameters were computed in order to have a basis for comparison with other desalination systems which may use either one. The thermal efficiency is strictly defined for the test unit in this study, though it can well be applied to other desalination systems.

5.2.5 General Entropic Analysis of the HVAC-HDH Cycle

The final segment of the system analysis is a general entropic analysis of the HDH cycle being investigated. The entropy analysis will include the air preheating, humidification and condensation process – for both one and two stages. It is important to note that the entropy analysis undertaken is not extensive in nature, particularly since the experimental setup was not properly instrumented to quantify all parameters needed for an accurate analysis; namely the evaporator feed-water mass flows and temperatures. These quantities will be estimated to the investigator's best knowledge. The entropy

analysis is intended for establishing a liberal estimate of the system entropy generation to identify highly entropic system processes. Overall system performance can thus be improved, in part, by reducing the entropy generation of these processes. Figure 5.2.5.1 shows the three system components and their respective thermodynamic control volume, the boundary represented by dotted lines, used in the entropy analysis.

The entropy generation for the air preheating process is defined by the air's entropy change due to the thermal loading. Moist air specific entropy values were obtained from the 2009 ASHRAE

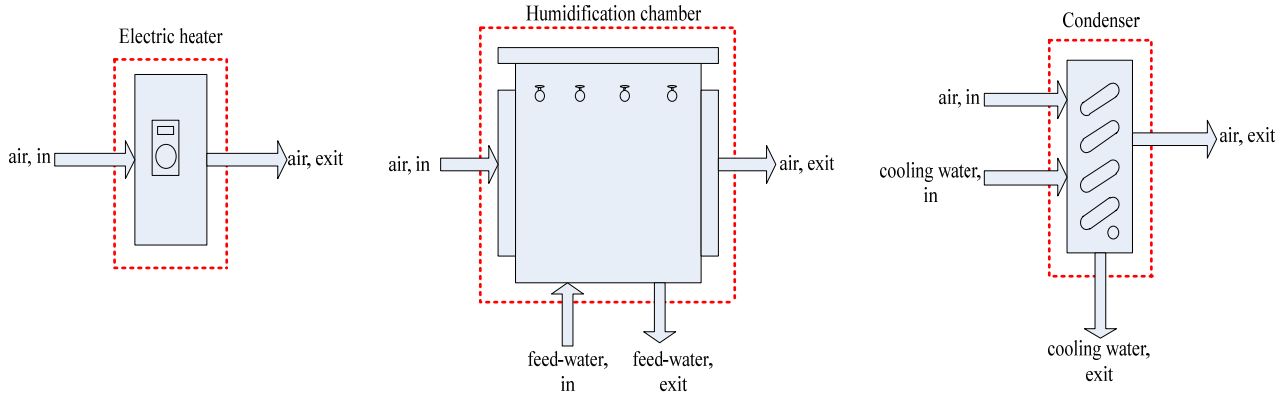

Figure 5.2.5.1: System components and their control volumes for entropy analysis

Fundamentals Handbook [31]. Any other entropy generating terms, e.g. due to turbulent mixing, are considered internal to the control volume enclosing the electric heater and are not considered. The entropy generation for the electric heater is expressed as:

$$\dot{S}_{gen,ht} = \dot{m}_a (s_{a,exit} - s_{a,in}) \tag{5.11}$$

The entropy generation for the humidification process considers the entropy changes in the air and the feed-water. The humidification chamber and its control volume are diagrammatically shown in Figure 5.2.5.1. Moist air specific entropy values are extracted from the same source used in the preheating process described above. Now, the evaporator was not instrumented to measure feed-water inlet and exit flow rates and temperatures - parameters that must be known in order to quantify the

entropy changes during the evaporation process. These quantities will be approximated by the investigator in the following manner. Since the feed-water is not preheated and is continually circulated through the humidification chamber, it will be assumed that it does not remain in contact with the process air long enough to experience an appreciable change in temperature. Therefore, feed-water will be assumed to be at the saturated liquid state at the system operating pressure. Finally, exit mass flow rate of the feed water will be assumed to be 60% of the entering mass flow rate (i.e. 40% of the entering feed-water evaporates into the air, remains on the CEM or sits in the chamber's sump). The entropy generation for the humidification process is expressed as[10]:

$$\dot{S}_{gen,h} = \dot{m}_a (s_{a,exit} - s_{a,in}) - 0.40\dot{m}_{w,in} s_w \tag{5.12}$$

The condenser entropy generation considers inlet and exit mass flows of process air and cooling water. Air and fluid side temperature and mass flow data were readily available and all the parameters of the following entropy generation equation were determined:

$$\dot{S}_{gen,cond} = \dot{m}_{cw} (s_{cw,exit} - s_{cw,in}) + \dot{m}_a (s_{a,exit} - s_{a,in}) + \dot{m}_{pw} s_{pw} \tag{5.13}$$

Air side entropy changes were determined as stated in the previous paragraphs while fluid side temperature and pressure data were used for entropy calculations.

5.3 Summary and Remarks

A set of experiments were designed in order to collect data to assess the performance and production capabilities of the HVAC based HDH desalination test unit. Two types of experiment sequences were conducted, Types I and II, testing the system in a one and two stage configuration, respectively. Both experiment sets shared the same experimental variables, namely the thickness of the CEM and air volumetric flow rate. The data demonstrated that there is no significant advantage for water production in increasing the thickness of the evaporative media or air volumetric flow rate past a

[10] The subscript *w* in the context of the system entropy equations refers to saturated liquid water.

particular point. This was useful in establishing a so called preferred system operational region (PSOR) for the current test system design. Fresh water production data and thermal heats load calculations for every experiment conducted were used for computing three system performance metrics, i.e. the performance and gained output ratios and a modified system thermal efficiency. It was found that the experimental unit exhibits GOR values below 1.0. The low GORs are likely caused by high thermal losses and zero heat recovery from the condensation process. A conservative thermodynamic entropy analysis of the three main HDH processes was conducted in an effort to identify highly entropic system processes that could be improved. The full spectrum of results is discussed in detail and interpreted in the following chapter.

Chapter 6: Results and Discussion

The purpose of this investigation was to determine the functionality of the HVAC-HDH desalination cycle and its production capabilities. Therefore, the experimental work and corresponding analysis were limited in their scope. Both were designed and executed to meet the end purposes of this study. System water production, energy consumption, conventional desalination plant performance metrics and water quality were quantified. Additionally, preferred operational configurations specific to this system were identified.

Theoretical development and discussion were limited to a generalized entropy analysis of the three main processes of the HDH cycle. The entropy analysis was intended to liberally quantify the entropy generation rates of the HVAC-HDH cycle in an attempt to identify probable areas of thermodynamic improvement. System optimization, simulation and parametric analysis were all beyond the scope of this investigation, though may be undertaken in future studies.

This chapter contains the results, discussion and interpretation of the analyses described in Chapter 5. The different analysis areas discussed in Chapter 5 will be reviewed and thoroughly discussed. The chapter concludes with an overall summary and concluding remarks.

6.1 Results and discussion of Type I and II Experiments

Type I experiments were conducted with the experimental system's basic configuration consisting of a single stage and the dehumidification process. Recall that a stage in the context of this investigation's HDH system is comprised of an air preheating and humidification phase. The experimental variables were CEM thickness and air volumetric flow rate – namely the same variables for Type II experiments. The results of this set of experiments established baseline values that were used to compare Type II results against.

Plots of the test unit's water production were generated for an initial exploratory visual analysis. Their purpose was to identify general trends in the system's water production capabilities and to loosely define the system's PSOR. Two variants of the water production plots were produced. The first kind illustrated the relationship between system water output and air volumetric flow rate for all thicknesses tested. Figure 6.1.1 shows cumulative plots of the different configurations and their water production for both experiment types. Plots for individual configurations and their curve fits are shown in Figures 6.1.2 and 6.1.3. The errors bars ascribed to the data points in the individual water production plots represent a range of values within a 95% confidence interval. Uncertainty analysis was performed according to Kline and McClintock's method [49] and verified using perturbation methods described by Moffat [50, 51]. Further literature was thoroughly reviewed to insure correct methods of computing experimental uncertainty [40, 52, 53]

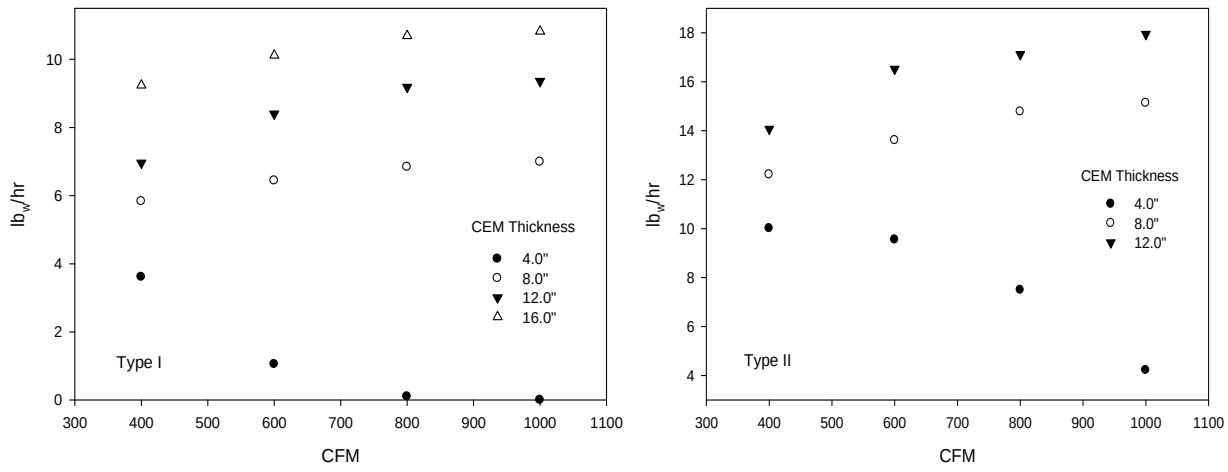

Figure 6.1.1: Cumulative water production plots for (a) Type I and (b) Type II experiments

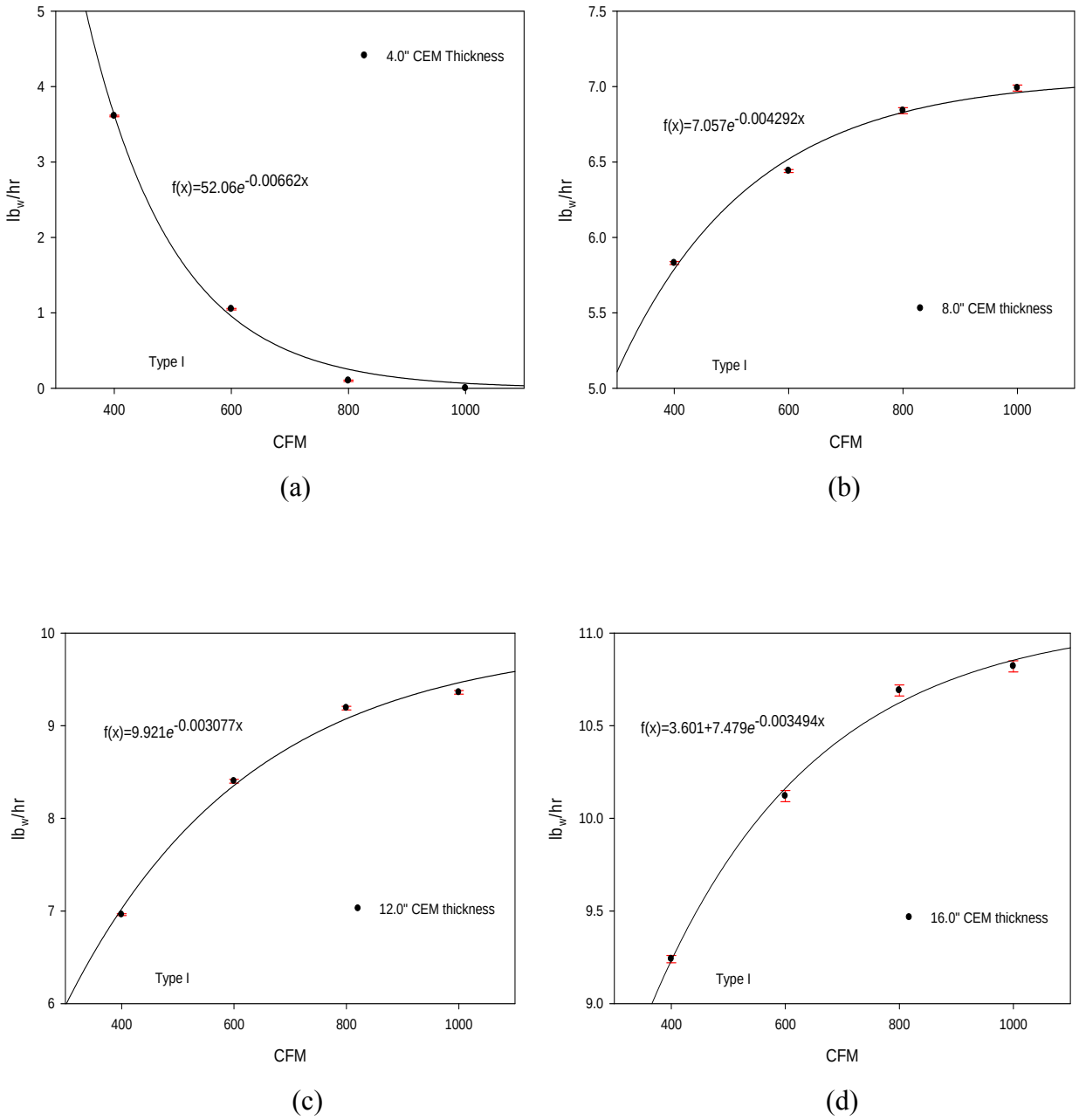

Figure 6.1.2: Individual Type I water production plots for CEM thickness: (a) 4.0” (b) 8.0” (c) 12.0” and (d) 16.0”

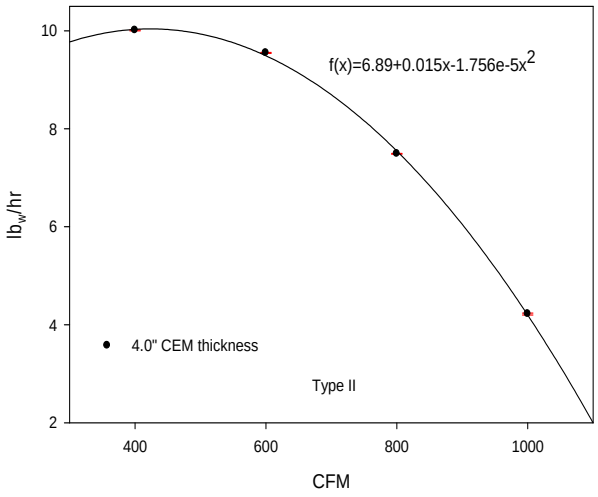

(a)

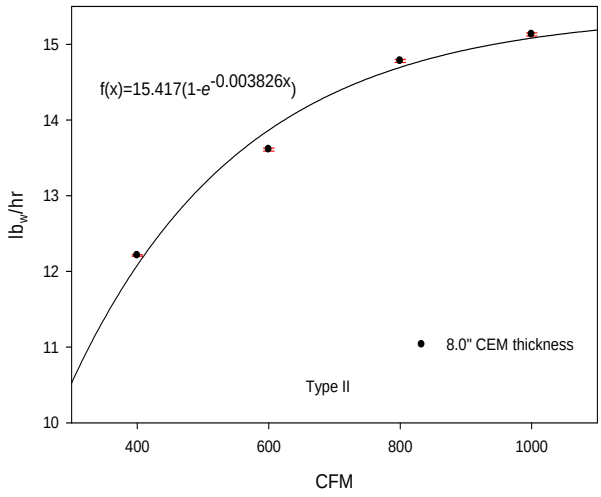

(b)

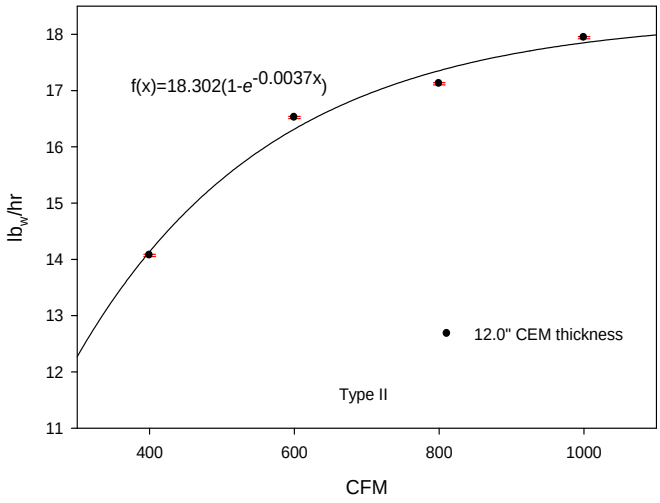

(c)

Figure 6.1.3: Individual Type II water production plots for CEM thickness: (a) 4.0” (b) 8.0” (c) 12.0”

General trends in the system water production with respect to air flow were observed in Figure 6.1.1. Examination of the plots and data for CEM thicknesses exceeding 4.0" reveals that water production rates increase with escalating values of CEM thickness and air volumetric flow rate. This behavior in water production was expected. The turbulent mixing within the CEM as air passes through it enhances the transport phenomena between the air and downward flowing water film. This results in the increased evaporator and CEM saturation efficiencies observed in Figures 6.1.4 and 6.1.5, respectively.

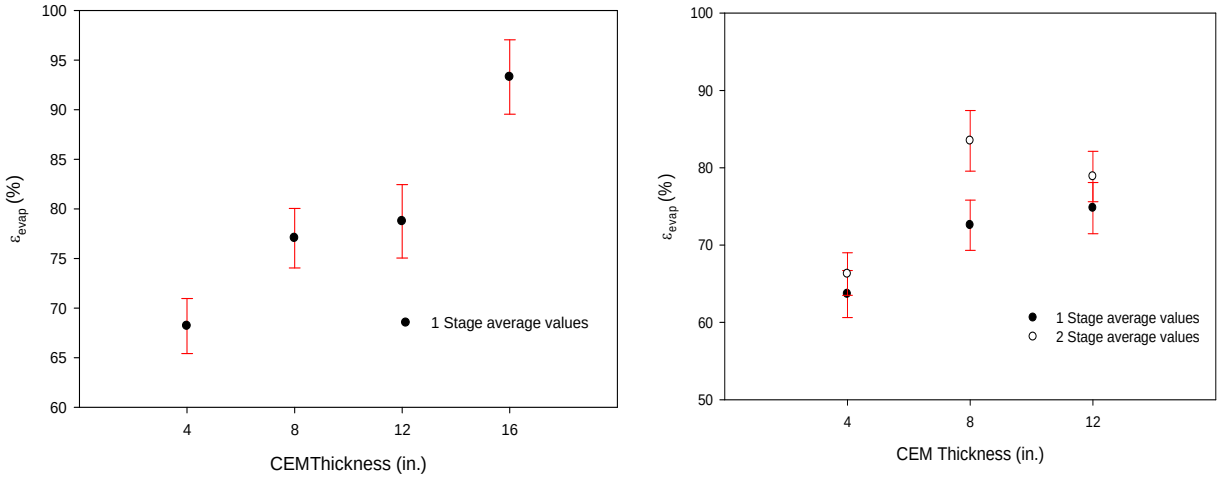

(a) (b)

Figure 6.1.4: Average (a) Type I and (b) Type II evaporator efficiencies

Efficiency calculations indicated insensitivity to increasing face velocities at these magnitudes. Thus, Figures 6.1.4 and 6.1.5 display average efficiency values for each experiment. Calculated CEM efficiencies compared favorably with visually determined values from manufacturer provided data [54] shown in Figure 6.1.6. The average difference between the calculated and manufacturer value was 5.24%. and 7.61% for Type I and II experiments, respectively. As a result, the observed trend in the saturation efficiency remains unaltered with manufacturer values. Increased saturation efficiencies

represent improved water vapor mass transfer into the air; by extension implying higher amounts of water production.

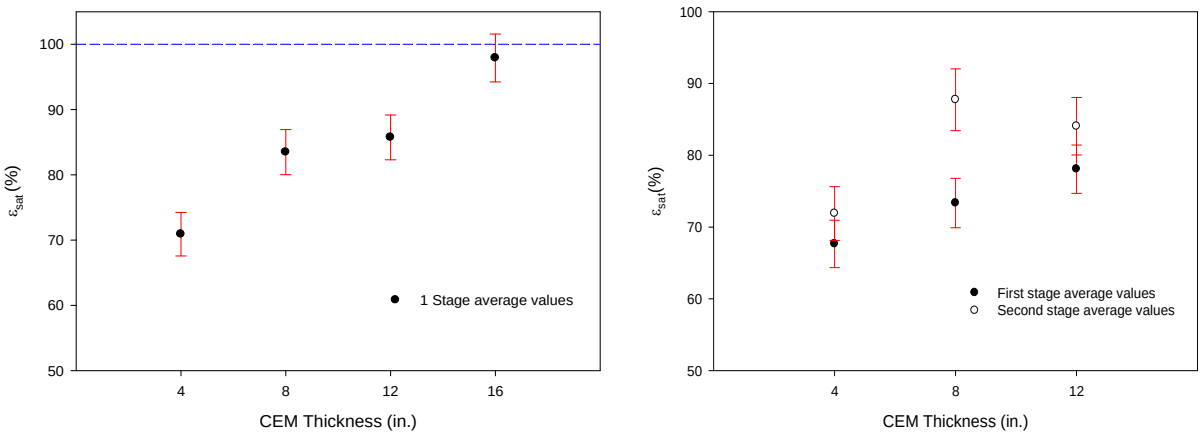

(a) (b)

Figure 6.1.5: Average (a) Type I and (b) Type II CEM efficiencies for different thicknesses

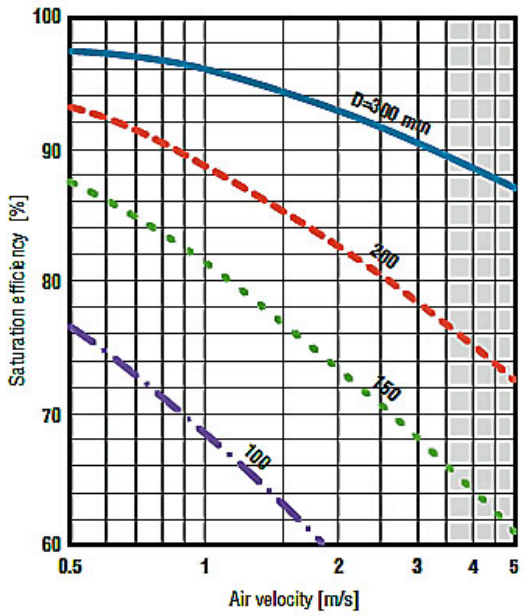

Figure 6.1.6: CELdek® 7060-15 CEM saturation efficiency curves [54]

Despite the overall increasing trends in water production, the relative difference in water extraction rates between incremental air CFM values actually diminishes. The differences are such that

each water production curve exhibits an exponential rise to an asymptotic maximum value. This behavior for the water production seemed counter intuitive, considering the increasing quasi-linear behavior observed in the evaporator and CEM efficiency plots. Thus, an increasing linear trend was also expected for the system water production.

The behavior of the water extraction rates described in the previous paragraph is likely due to the condenser's inability to extract the latent heat necessary to maintain linearly escalating extraction rates with increased system airflow. The condenser cooling water flow rate was kept at a constant 12.9 gpm. This value was determined with proprietary software provided by the heat exchanger manufacturer [39]. Enough water flow was maintained in the cooling circuit to reduce the incoming air temperature to the ambient dew-point temperature of 68°F with a maximum airside velocity of 444.44 fpm (i.e. 1000 CFM). As explained in §4.2.1, the condenser fluid side volumetric flow rate was kept constant to reduce experimental variables. Though the cooling water flow rate was set at a calculated value adequate for establishing the necessary conditions for condensation, the possibility of calculation or experimental errors does exist. It is highly probable that the nominal flow rate value was not correctly established, hindering the latent heat removal from the air.

Figure 6.1.7 shows comparative plots of system water production for every CEM thickness tested for both Type I and II experiments. Type II experiments for a CEM thickness of 16.0" were not conducted due to time constraints, resulting in a single Type I water production curve for this configuration. Examination of all the production plots illustrates similar water production trends for both Type I and II experiments. Water production for Type I experiments varied from 0 – 10.82 lb_w/hr for 4.0" and 16.0" CEM thicknesses, respectively, at 1000 CFM. Similarly, at 1000 CFM, Type II experiments' water production varied from 4.22 – 17.94 lb_w/hr, for 4.0" and 16.0" CEM thicknesses, respectively. The empirical relationships for each configuration tested will predict the system fresh water production for different air volumetric flow rates (cf. Figures 6.1.2-6.1.3).

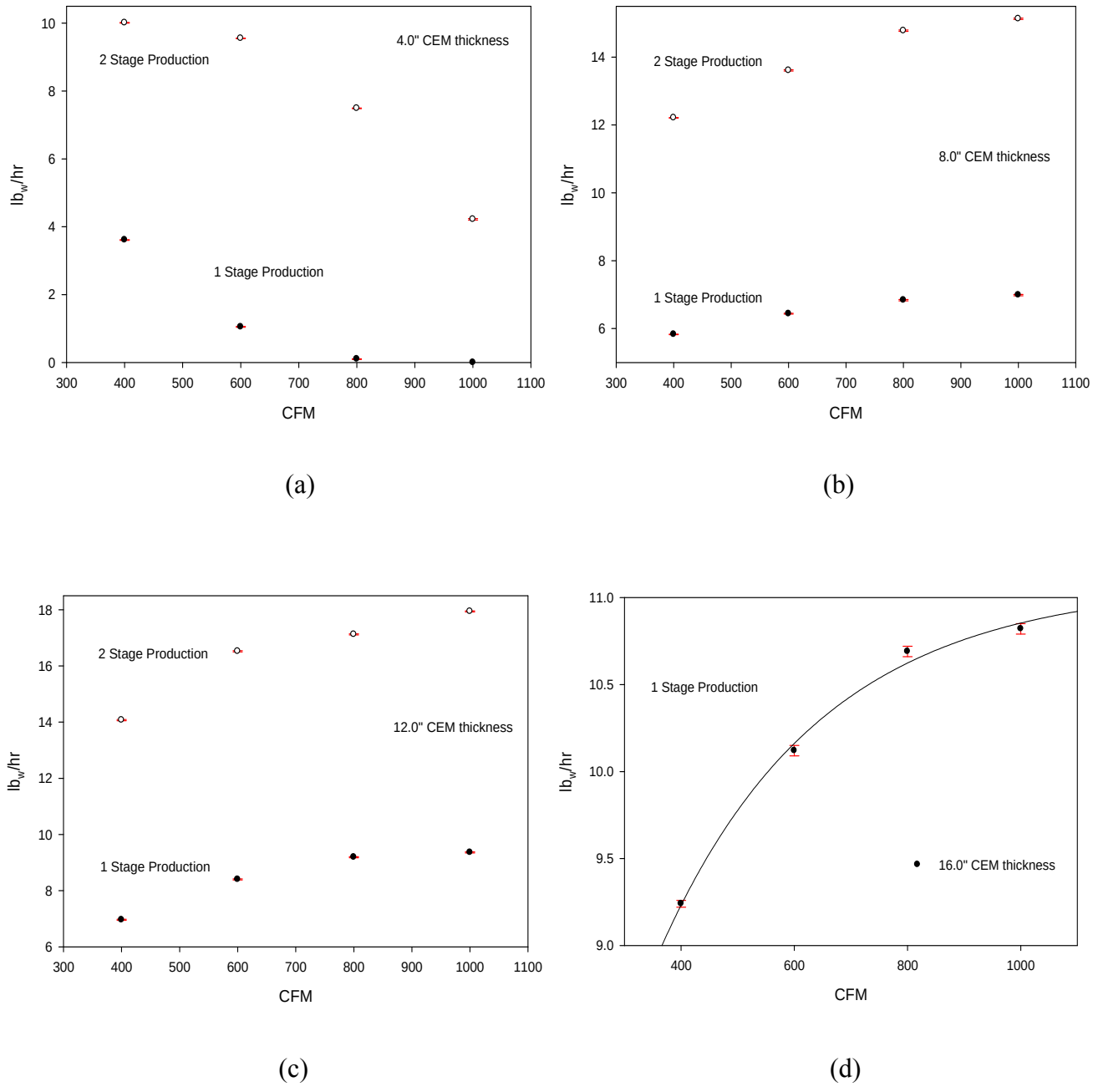

Figure 6.1.7: Type I and II comparative water production plots for CEM thickness: (a) 4.0" (b) 8.0" (c) 12.0" and (d) 16.0"

Type II production curves are shifted in the positive ordinate direction but follow a very similar trend as its Type I counterpart. This behavior was to be expected. Higher production values for Type II experiments are due to augmented CEM thicknesses in the evaporators. Since the condenser operational parameters remained unchanged for both experiment types, its water extraction capabilities were also expected to remain unchanged – hence the similarity in water production plots. The investigator postulates that a Type II water production curve for the 16.0" CEM configuration would have resembled its Type I counterpart had the pertinent data been collected.

In general, a distinct behavior is seen in both types of production curves for the 4.0" CEM thickness configuration. Both curves display a decaying production trend with escalating values of air volumetric flow rate. This production trend is likely caused by the low 70.90% and 72.58% CEM evaporative efficiency for Type I and II experiments, respectively. The elevated 444.44 fpm air velocity through the evaporative media minimizes water to air interfacial contact time, hindering water vapor mass transfer to the air. Low CEM saturation during an experiment due to insufficient feed-water flow could potentially be the problem, as well. High air velocities in conjunction with small CEM surface area (only 4.0" CEM thickness) could have caused the media to dry, thus reducing fresh water production with escalating air flow rates. Any of these characteristics operating in tandem could be the probable root causes for the observed behavior. These anomalies in the production trends could have been further explored by conducting additional experiments. Unfortunately, the experimental unit was decommissioned and further experimentation was no longer possible.

Another curious anomaly is seen in the decaying behavior of both Type I and II, 4.0" CEM production curves. The Type I curve is a decaying exponential while Type II is best represented by a negative polynomial (cf. Figures 6.1.2 and 6.1.3). This is unusual as both curves were expected to exhibit similar behavior, as seen with the other plots. There is no clear explanation for this. It is possible that the additional water vapor mass transfer to the air in the second evaporation stage causes

water extraction rates to decay less rapidly, as exemplified by the Type II curve. Further experimentation could have provided more information to explain this behavior.

A plot illustrating water production capabilities with respect to CEM thickness for each tested air volume flow rate was generated. Four curves, one for each CFM setting, were generated as shown in Figures 6.1.8 and 6.1.10. These plots have much practical utility for system analysis. They clearly demonstrate the variation of water production with respect to CEM thickness for constant values of airflow. Visual or numerical comparison of water production for differing air flow rates was facilitated by consolidating all production curves into a single plot for a particular experiment type. Moreover, this plot enables an initial visual evaluation for determining the system PSOR, as described in §5.2.2.

Visual inspection of Figures 6.1.8 and 6.1.10 shows some interesting features. The values for the 800 and 1000 CFM curves appear extremely close through the range of CEM thicknesses. This implies that there is no real benefit in operating the system at an air volumetric flow rate exceeding 800 CFM. Mathematical expressions were necessary to accurately evaluate and predict water production values. These formulations were generated with a regression analysis for each data set and were also used to numerically establish the system PSOR. Figure 6.1.10, displaying the production curves for Type II experiments, does not show the trend seen in Type I experiments. There is an appreciable difference in water production between escalating CFM values and the system should be operated through the complete range of air flow rates.

The production curves shown in Figures 6.1.9 and 6.1.11 were generated using curve fit equations from a data regression analysis.[11] Mathcad™ 15 was used for a basic numerical analysis of the mathematical fits using the regression equations. For Type I experiments, an average 0.12 lb_w/hr difference in water production between the 800 and 1000 CFM settings was observed – a marginal difference evident from the initial visual inspection. As a result, an upper limit of 800 CFM was

[11] Regression analysis was performed with Sigmaplot 10™

implemented for a single stage system configuration. The water production curves in blue are recommended to be included within the PSOR limits. There was no upper bound for the air volumetric flow rate for Type II experiments, as previously discussed.

The lateral limits of the system PSOR where determined by examining the relative difference in water production with respect to CEM thickness. The upper PSOR limits were established as follows. Visual inspection of Figure 6.1.9(a) reveals no significant increase in the water extraction rate for the 600 and 800 CFM curves for CEM thicknesses exceeding 20.0". Higher CEM thickness represents additional air side pressure drop without any increase in water production. Thus, there is no benefit in using more than 20.0" of CEM for a 1 stage cycle. Inspecting Figure 6.1.11(a), for Type II experiments, reveals an intersection of the 600 and 800 CFM curves at a CEM thickness value circa 16.0". Past this point, the 600 CFM curve overtakes the 800 CFM production. There is no benefit in operating the system at 800 CFM with 16.0" of CEM past this junction. The upper bound of the PSOR is therefore established at 16.0" for Type II experiments. However, due to lack of experimental data, the Type II curve fits are subject to some fluctuation and speculation.

The lower lateral PSOR limit was established at an abscissa value where all three curves exhibited unique and non-collinear water production values; i.e. no curves were superimposed. This value was established at a CEM thickness of 4.0" and 7.0" for Type I and II configurations, respectively. Ascending values of water production are seen with ascending values of air CFM past these established points. Both Figures 6.1.9(b) and 6.1.11 (b) show the production curves within the established system PSOR. It is important to note that the PSOR is a liberally established system operational window. An optimization and parametric study, beyond the scope of this investigation, is needed to establish an "optimal" system operational region. This type of numerical analysis can be undertaken as part of a separate investigation which would require the collection of more data in order to establish mathematical models faithful to the experimental data.

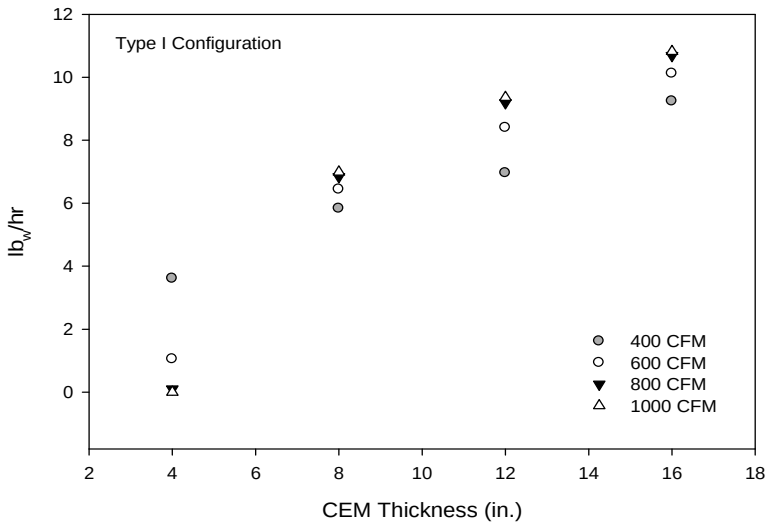

Figure 6.1.8: Type I water production rates with respect to thickness

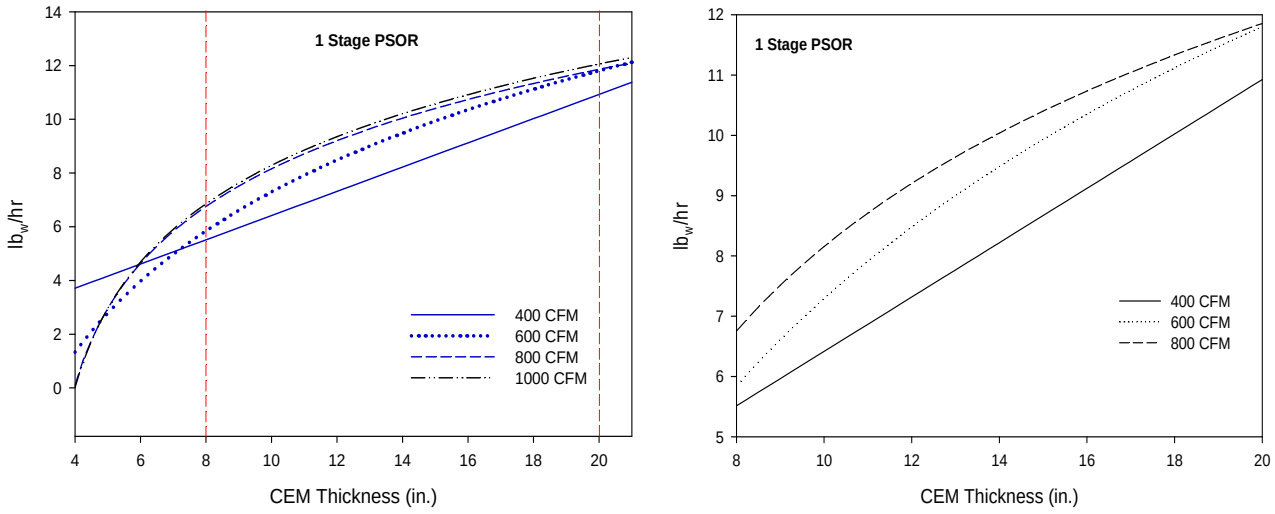

(a) (b)

Figure 6.1.9: Type I (a) mathematical fits of system PSOR and (b) system detail PSOR window

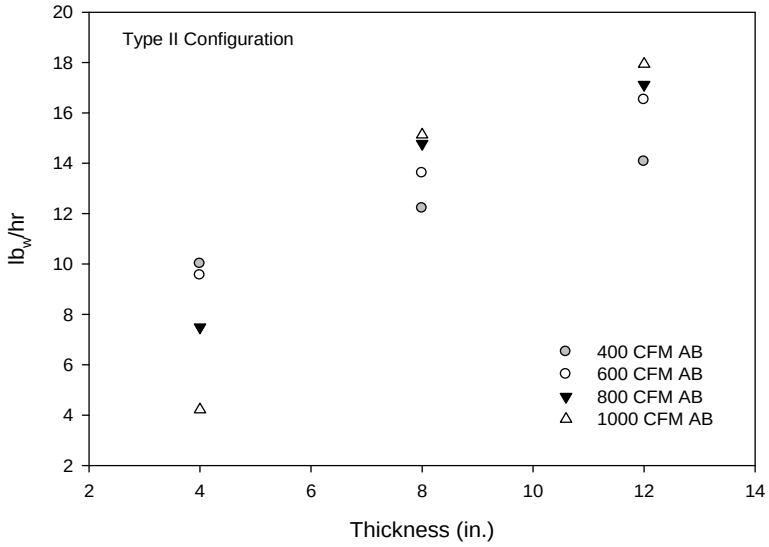

Figure 6.1.10: Type II water production rates with respect to thickness

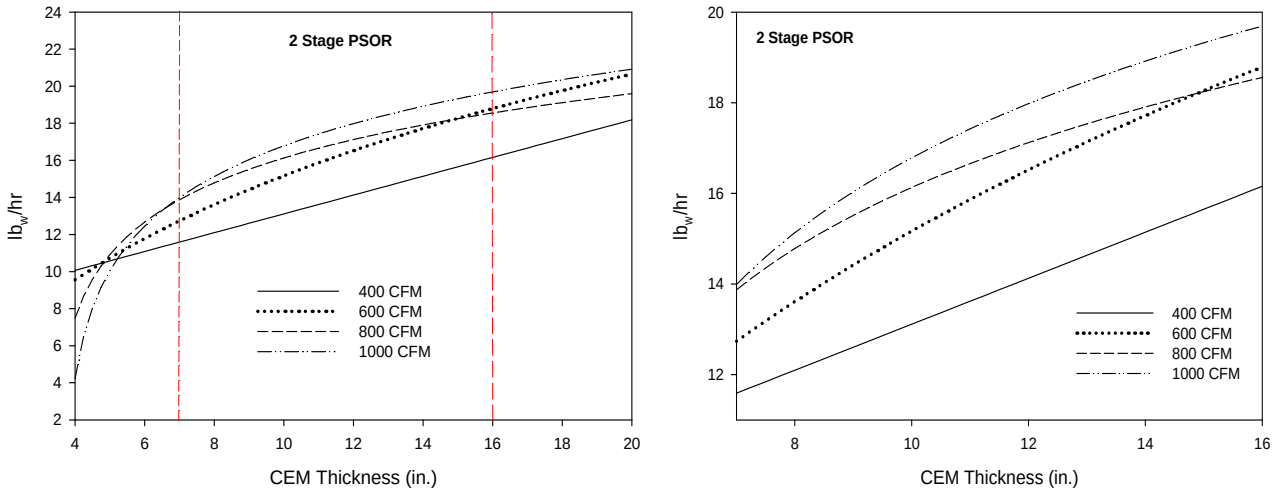

(a) (b)

Figure 6.1.11: Type II (a) mathematical fits of system PSOR and (b) system detail PSOR window

6.2 System Performance Metrics

Three system performance metrics were quantified for this investigation: performance ratio, gained output ratio and adjusted desalination thermal efficiency. The definitions and practical significance of each of these metrics are discussed in detail in §5.2.4. Figure 6.2.1 displays the performance ratios for all experiments. PR plots showing error bars for individual CEM thicknesses are shown in Figures 6.2.2 and 6.2.3.

The 4.0" CEM performance ratio plots exhibit a clear exponential decaying behavior as air volumetric flow rate increases. The PR behavior becomes more linear in nature (with a negative line slope) as the CEM thickness increases. This trend is observed in both Type I and II experiments. This presents an interesting and counterintuitive trend in the PR curves that merits further discussion.

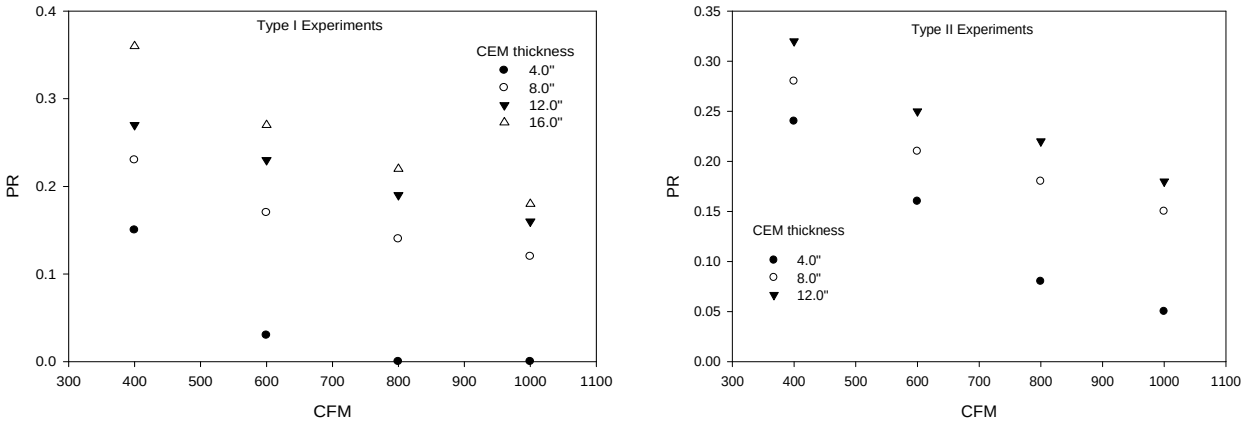

(a) (b)

Figure 6.2.1: Cumulative plots of (a) Type I and (b) Type II experiment performance ratios

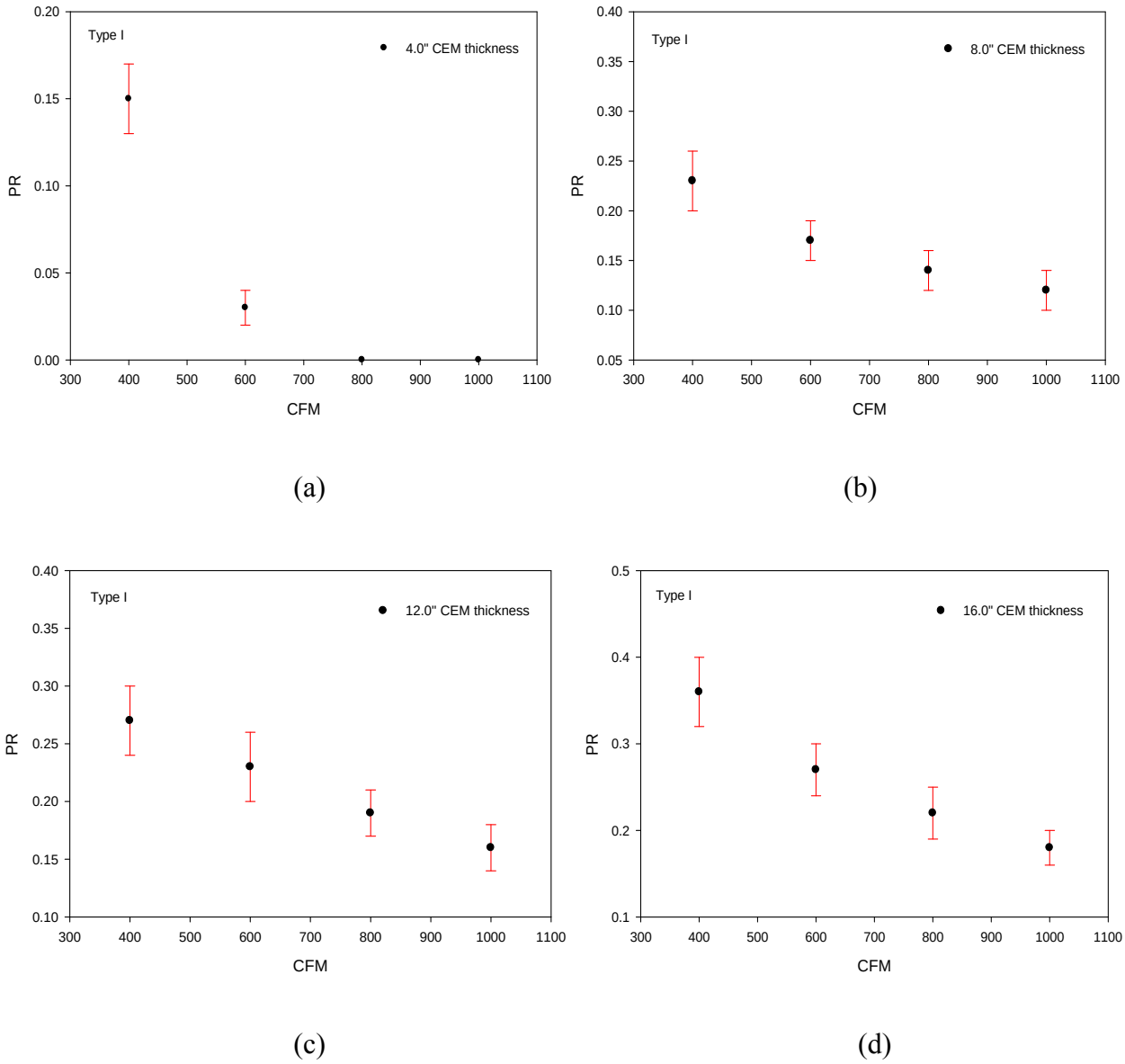

Figure 6.2.2: Individual Type I PR plots for CEM thickness: (a) 4.0” (b) 8.0” (c) 12.0” and (d) 16.0”

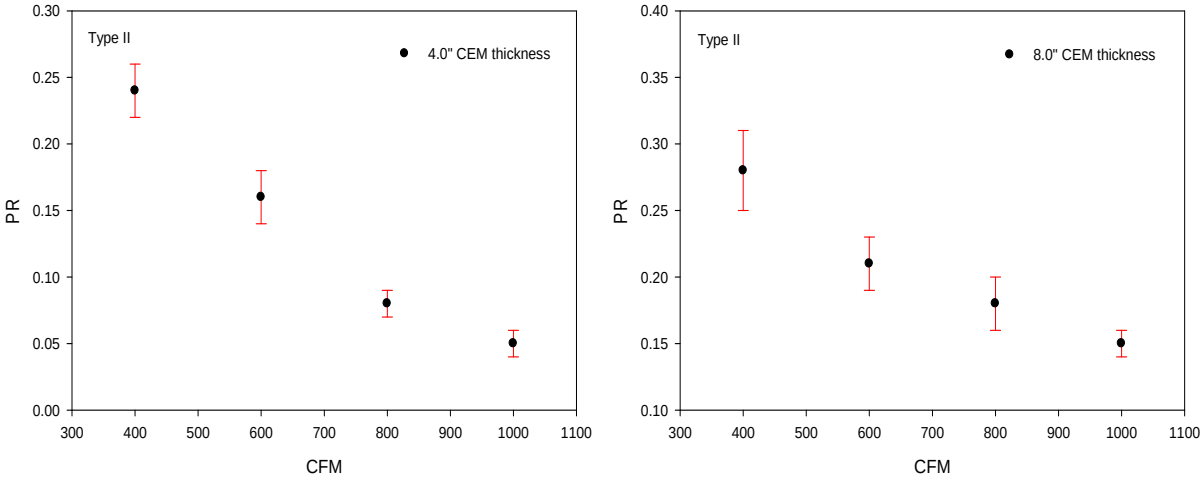

(a)

(b)

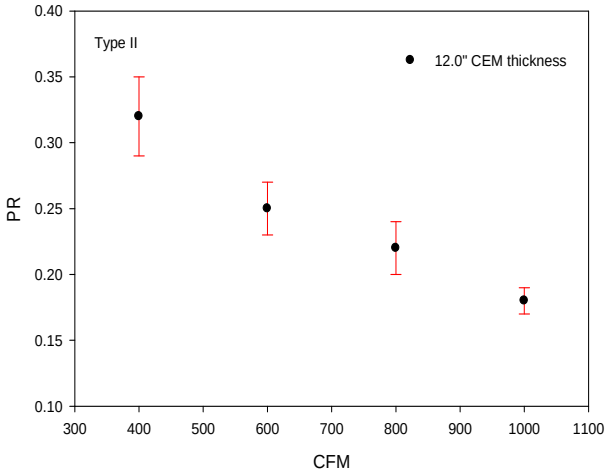

(c)

Figure 6.2.3: Individual Type II PR plots for CEM thickness: (a) 4.0” (b) 8.0” (c) 12.0”

A similar trend was certainly expected for the gained output ratio plots, shown in an analogous manner to its PR counterparts in Figures 6.2.4 - 6.2.6. The definition of the GOR is very similar to that of the PR (cf. §5.2.4); only differing in the multiplicative constant of the water production to heat input ratio. Its ratio is multiplied by the enthalpy of vaporization of water at the system operating pressure, as defined by equation (5.9). Since the experimental unit was a CWOA system, operating pressure was assumed to be 12.82 psi; the local atmospheric pressure at an altitude of 3740 ft.

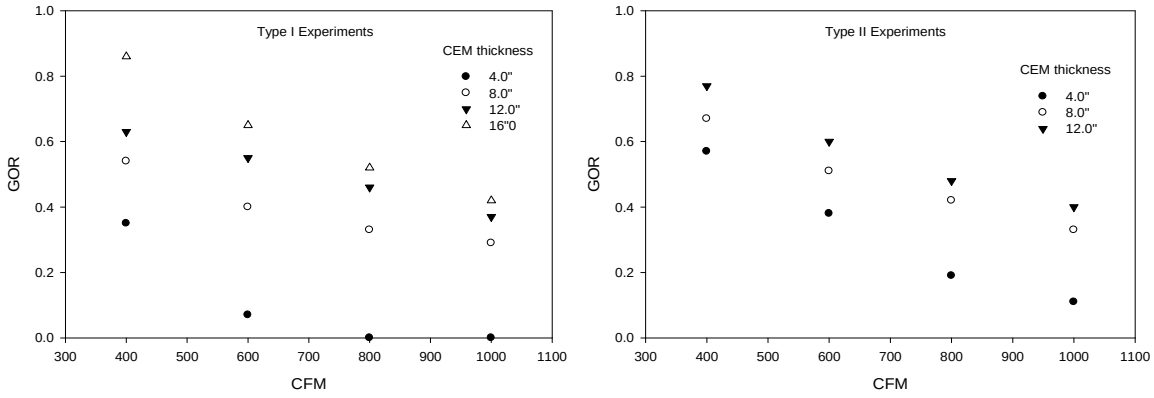

(a) (b)

Figure 6.2.4: Cumulative plots of (a) Type I and (b) Type II experiment gained output ratios

THE REST OF THIS PAGE LEFT INTENTIONALLY BLANK

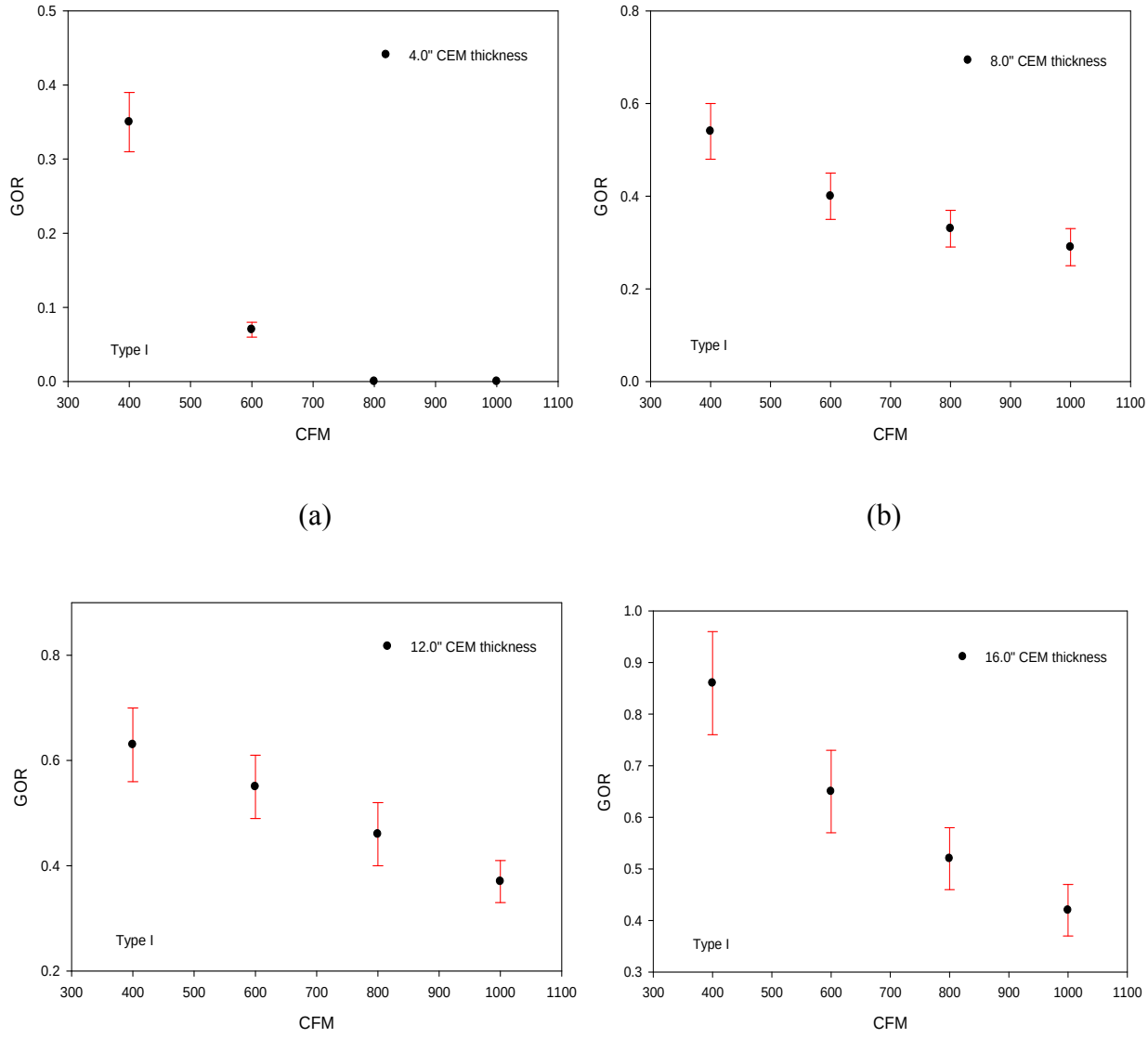

Figure 6.2.5: Individual Type I GOR plots for CEM thickness: (a) 4.0” (b) 8.0” (c) 12.0” & (d) 16.0”

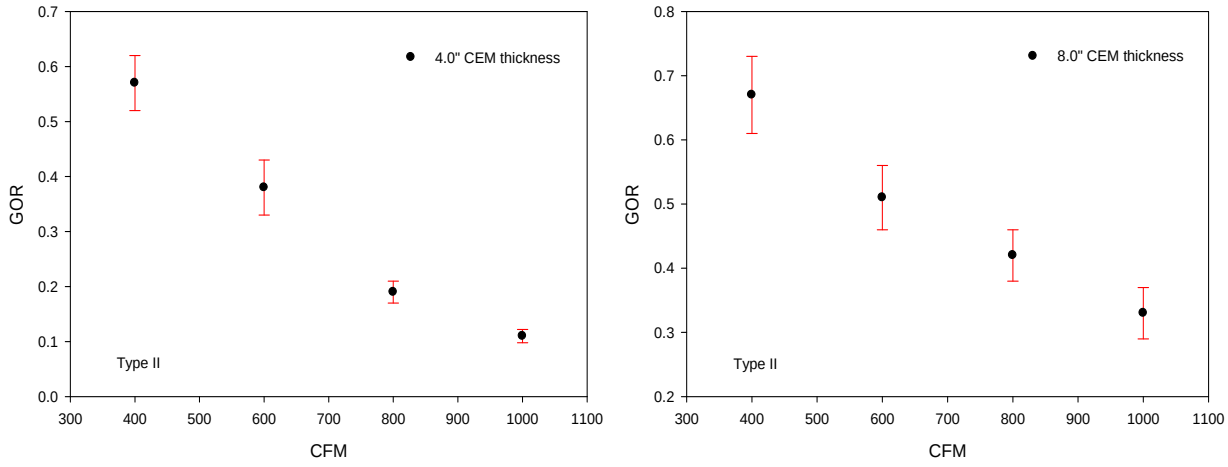

(a)

(b)

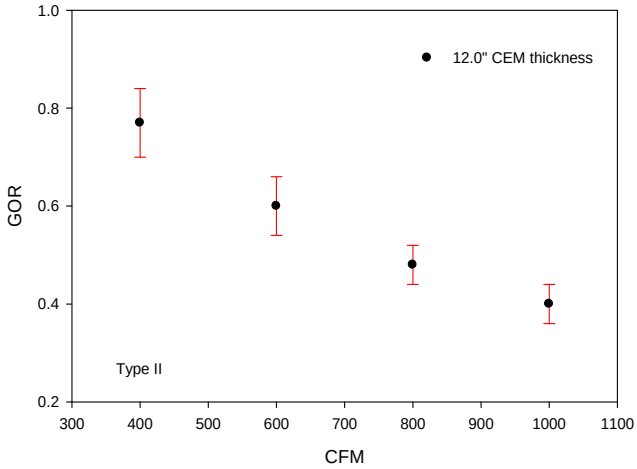

(c)

Figure 6.2.6: Individual Type II GOR plots for CEM thickness: (a) 4.0” (b) 8.0” (c) 12.0”

Examination of the data presented in Figures 6.2.4 - 6.2.6 indicates GOR values below 1.0. The data reveal that the maximum system GOR was 0.86 and 0.77 for a Type I and Type II configuration, respectively. The low values of GOR are indicative of poor thermal efficiency, particularly since the experimental system was not designed for latent heat recovery from the condensation process. Most conventional systems use recovered heat for feed-water or air preheating, potentially increasing water production and reducing the thermal load requirements.

However, low values of GOR are rather typical for this kind of desalination process. Solar stills, for example, exhibit average GOR values below 0.5 [1] while most air HDH cycles have GORs that vary from 0.78-3.5 [23]. The GORs for this system compare favorably with values reported in the open literature. Air HDH systems operating at atmospheric pressures are known to be highly thermally inefficient. This is frequently reported in scholarly literature and determined in the previous feasibility analysis for this system [5]. This HVAC-HDH unit is unable to compete with conventional desalination systems (e.g. RO, MSF, MED) in terms of efficiency – and it was never intended to do so. This system is ultimately designed to be coupled with a salinity-gradient solar pond for its energy requirements. The "free", low-grade thermal energy obtained from the solar pond is adequate for powering the system and driving the thermal processes. Thus, thermal efficiency is not of primary concern for this experimental unit.

The most curious trend in both PR and GOR plots is the apparent transition from an evident exponential decay at 4.0" CEM thickness to a decreasing linear trend for increasing values of thickness. There is some speculation by the investigator as to the actual mathematical trend at CEM thicknesses exceeding 4.0". The very apparent linear behavior of these plots can also be a very slowly decaying exponential function. This is a plausible argument, considering that all the water production curves exhibit exponential or logarithmic behavior. Water production plots all exhibit relatively small, negative exponential constants of similar magnitudes (cf. Figure 6.1.2 and 6.1.3). It would seem logical that any

multiplicative variation of a basic water production ratio, as defined by the PR and GOR, would also be exponential in nature.

Both the PR and GOR are defined as ratios of water production to useful system heat input multiplied by a constant. Examination of heat input data revealed that total system heat transfer rate increased linearly as air CFM increased. Thus, the relationship of a ratio between a generic exponential function of the form $f_e(x) = Ae^{-Bx}$ (e.g. Figures 6.1.2-6.1.3) and a conventional positive linear function, $f_L(x) = y_o + mx$, was briefly explored in an effort to identify the behavior of this functional ratio. It was found that the ratio maintained a decaying exponential behavior when plotted using various integer values for constants A ,B, y_o and m – as was expected. However, as the exponential constant become smaller in magnitude, i.e. $0 < B \leq 1$, the exponential decay in the plot became less pronounced. As B was reduced and the linear constant values increased, the plot became less exponential in nature, eventually resembling a decreasing linear function.

Proper characterization of the PR and GOR behavior would require a detailed and in-depth numerical and functional analysis of the data, which is beyond the scope of this investigation. It was important, however, to superficially examine the functional behavior of this data at a minimum. This was done in an effort to identify any anomalies in the experimental data or numerical analysis that would merit further scrutiny. Though the possibility of experimental error still exists, the general trends exhibited by the PR and GOR are favorably within the confines of the expected mathematical functional behavior.

The adjusted desalination thermal efficiency, as defined in §5.2.4, is similar in form to the GOR. This performance parameter accounts for the mechanical power expended by the system in addition to the total useful heat input for the HVAC-HDH cycle. Both air-side and fluid-side system losses were estimated. A detailed system loss analysis was not performed due to the limited scope of this investigation. An analysis of this detail would be applicable to an optimization or parametric study of

the process – both not within the scope of the project. A liberal calculation of the losses was executed for completeness.

Fluid-side system losses were considered to remain the same for every experiment configuration since the volumetric flow rate of the cooling water was kept at a constant 12.9 gpm. The water was considered incompressible and any density changes due to temperature were considered negligible. The rubber conduit used for the water circulation was considered hydrodynamically smooth for the determination of the friction factor and major losses. Minor losses included a sharp re-entry, sudden expansion, fully open globe valve, venturi pressure loss and a 90° threaded elbow. Finally, the heat exchanger fluid-side losses were calculated with its proprietary software suite [39]. Assuming a 75% operational efficiency for the pump, the total shaft power totaled 532 Btu/hr (0.20 HP).

Air-side pressure losses considered major frictional losses due to ductwork, CEM pressure drop and heat exchanger air side pressure drop. Specific volume was computed for every experiment performed for use in experimental uncertainty calculations. Air was assumed to behave as a perfect gas at an ambient operating pressure of 12.82 psi. Using an average air temperature, the specific volume was computed for each experiment using the perfect gas equation. Only small variations in air density were noticed under the operational temperature ranges. Therefore, the average value of air specific volume, 16.29 ft^3/lb_{mda}, was deemed accurate for purposes of this analysis. CEM pressure drops were obtained from manufacturer provided data [54] shown in Figure 6.2.7. As with the fluid-side pressure losses, the condenser air-side pressure drop for each experiment was computed with the same proprietary software [39]. Air-side power requirements ranged from 22.34 – 272.12 Btu/hr.

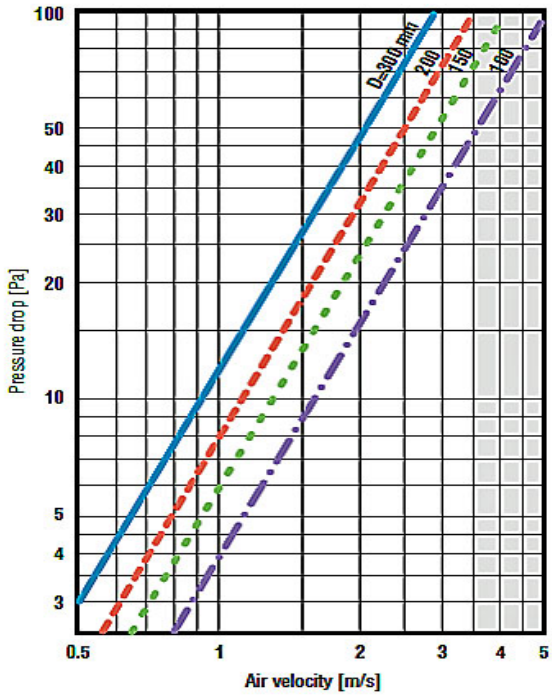

Figure 6.2.7: CELdek® 7060-15 pressure drop curve [54]

The computed power estimates for both air and fluid sides were used in the computation of the ADTE for each experiment. The GOR was used as a basis for comparison due to its similarity to the ADTE. Values of the ADTE and GOR were nearly identical; the ADTE was 100 times larger due to the fact that it is reported as a percentage rather than a ratio. The actual ADTE ratio differed from the GOR by a maximum of 0.01 in a few instances. For all practical purposes the ADTE ratio and GOR are identical, which was expected. The system mechanical power is several orders of magnitude smaller than the useful heat input. As a result, the end ADTE calculations were insensitive to the addition of this term.

Uncertainty calculations were not performed for the ADTE in part due to the complicated form of the turbulent flow, Darcy-Weisbach and Chen equations used for computing system major losses. The non-product form of the Bernoulli equation for the system would require the investigator to use a complex Kline-McClintock mathematical formulation [49] or an elaborate perturbation method [51] to compute experimental uncertainty. Since loss calculations were liberally quantified, there was no

compelling reason to incorporate such level of detail. Tables 6.2.1 and 6.2.2 show the values of the ADTE for Type I and II experiments, respectively.

Table 6.2.1: Adjusted Desalination Thermal Efficiency (%) for Type I experiments

CFM	**4.0”**	**8.0”**	**12.0”**	**16.0”**
400	34.37	52.83	61.77	84.55
600	6.98	39.77	53.69	64.10
800	0.12	32.45	44.99	51.79
1000	0	28.82	36.71	41.67

Table 6.2.2: Adjusted Desalination Thermal Efficiency (%) for Type II experiments

CFM	**4.0”**	**8.0”**	**12.0”**
400	55.98	66.16	76.24
600	37.90	50.52	59.46
800	18.67	41.57	47.22
1000	11.26	35.87	40.17

The final area of experimental analysis was a very general and liberal calculation of entropy. As mentioned in §5.2.5, the entropy analysis was performed for thoroughness in analysis and to identify any highly entropic system processes. Like the ADTE, quantification of experimental uncertainty was not computed. The entropy analysis is extremely general and is based on several assumptions since the system was not instrumented to record data pertinent to entropy analysis. Entropy generation values were found to behave as expected – they increased with higher system air flow rates and with additional stages, inherent of Type II experiments.

The condensation process was found to be the most entropic. This was expected since the condenser control volume (cf. Figure 5.2.5.1) has several potential sources for entropy generation. Practically interpreted, the condenser removes a large amount of entropy from the incoming sources. It could be postulated that this particular system component/process is the HVAC-HDH cycle's primary "entropy sink". It can possibly be used to divert system entropy and increase availability. Though the system is not power generating, increased system availability and reduced entropy generation makes it thermodynamically attractive and efficient. Entropy generation for each system process was calculated according the methods in §5.2.5 for each experiment performed. Entropy was quantified for each experiment within a selected value of air CFM (cf. §4.2.1 for test matrix details). The computed values were averaged and are reported in Tables 6.2.3 and 6.2.4 for both experiment types.

Table 6.2.3: Average entropy generation values (Btu/s°F) for Type I experiments

CFM	**Heater**	**Evaporator**	**Condenser**
400	0.011	0.017	0.062
600	0.016	0.025	0.074
800	0.020	0.036	0.077
1000	0.026	0.042	0.080

THE REST OF THIS PAGE LEFT INTENTIONALLY BLANK

Table 6.2.4: Average entropy generation values (Btu/s°F) for Type II experiments

CFM	Stage 1 Heater	Stage 2 Heater	Stage 1 Evaporator	Stage 2 Evaporator	Condenser
400	0.011	0.026	0.025	0.024	0.096
600	0.016	0.038	0.036	0.038	0.103
800	0.021	0.053	0.051	0.055	0.112
1000	0.025	0.060	0.059	0.061	0.125

6.3 Water quality of HVAC-HDH desalination process

The conductivity of the experimental unit's product water is an essential performance metric, as it designates the unit's efficacy in desalinating the saline feed-water. As previously discussed, high water conductivity values indicate an electrolytic solution with the ability to conduct electrical current. Low conductivity values, by extension, would represent a solution low in "salt" concentration ("salt" is used as a generic umbrella term indicating the various types of salts found in water). Typical conductivity values associated with certain grades of water are listed in Table 5.2.1.1. Figure 6.3.1 shows the measured conductivity of samples taken from the experimental unit's water production. Sixteen samples were collected from the test unit's production. The samples had a calculated mean of 19±2 μS/cm (20:1), with a standard deviation and error of 3.04 and 0.76 μS/cm, respectively. Laboratory tap water was used as the feed-water for the all experiments in this investigation. An electronic communication between Dr. A.J. Tarquin and Dr. J.A. Dowdy, faculty members at The University of Texas at El Paso, indicated that the typical conductance of laboratory tap water was approximately 800 μS/cm [55]. The product water from the experimental setup was 2.35% of the stated nominal conductivity of the utilized tap water. This represents a 97.65% reduction in water conductivity as a result of the HVAC-HDH desalination cycle.

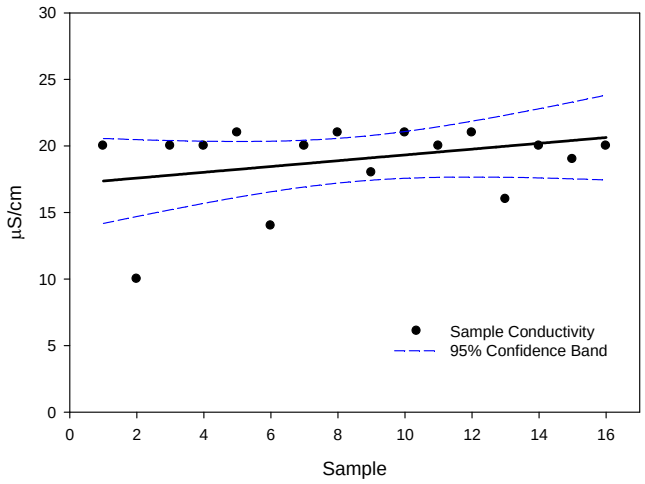

Figure 6.3.1: Desalinated water quality of experimental HVAC-HDH unit

6.4 Theoretical unit versus experimental unit: a brief discussion

This investigation was the experimental extension of a feasibility analysis performed by the investigator, Love and Enriquez [5]. The theoretical system consisted of a five stage HDH cycle and slightly different components. Suitable substitutions were made in the design and construction of the experimental two stage system so as to not affect the overall function of the original HDH process. Moreover, the feasibility analysis only incorporated 8.0" of CEM in each humidification chamber.

In order to properly compare the theoretical unit's performance to its experimental counterpart, it was necessary to adjust the production data of the theoretical unit to reflect that of a two stage system. Data from the feasibility analysis was examined and adjusted to reflect this change. Figure 6.4.1 displays production data for both theoretical and experimental units using an 8.0" CEM thickness. Examination of Figure 6.4.1 indicates that the theoretical unit's production capabilities exceed those of the experimental system, particularly with escalating values of air volumetric flow rate. This is mathematically caused by the theoretical unit's positive linear trend for water production. Theoretical water production curves exhibit linear regression fitted slopes of 0.0223 and 0.0715 $lb_w/(hr \cdot CFM)$ for a single and two stage system, respectively.

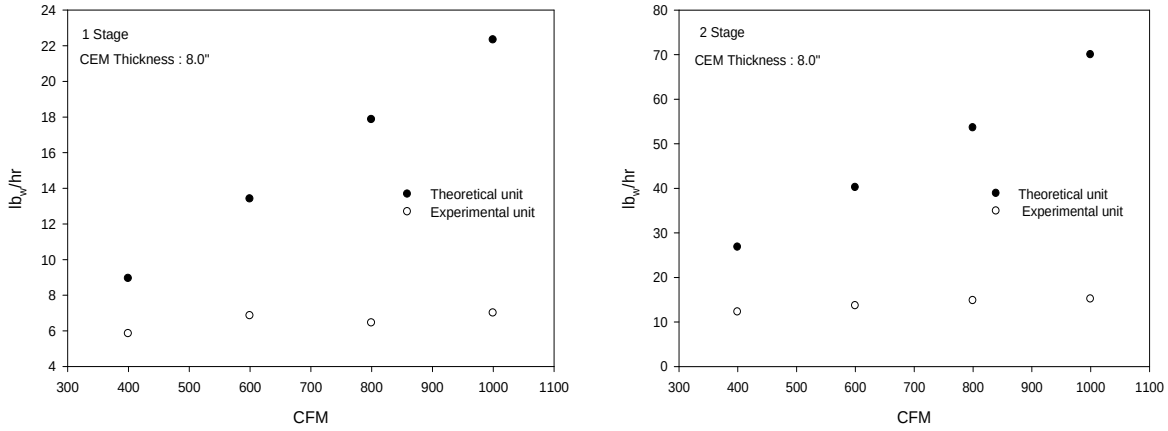

(a) (b)

Figure 6.4.1: Water production comparative plots between theoretical & experimental units for (a) 1 Stage and (b) 2 Stage configurations

As a result the theoretical system shows an average 26% increase in water production with each incremental setting of air CFM. On average the differences in water production rates between theoretical and experimental systems were 9.10 lb_w/hr and 33.69 lb_w/hr for 1 and 2 stage configurations respectively. Finally, GORs were computed for both systems. The calculations indicated that theoretical system exhibits average values of 1.06 and 2.51 for 1 and 2 stage systems, respectively. The actual experimental unit has average GOR values of 0.39 and 0.49 for 1 and 2 stage systems of the same configuration.

We recall the experimental unit's water production curves exponentially increase to an asymptotic maximum value. The system's production capabilities are quickly bounded with escalating air flow, unlike its theoretical counterpart, due to the functional nature of the equations modeling its water production rates. However, at these graphical scales, water production rates for the test unit seem nearly constant when directly compared to the theoretical values. The exponential behavior of the test system for these experimental conditions is evident in Figures 6.1.2 and 6.1.3.

The difference between the production capabilities of the compared units are likely primarily rooted in the condenser performance and the maximum target air temperature of the heating stages. The

elevated heating stage air temperatures of the theoretical unit, 157 °F on average, could potentially allow the air to carry higher amounts of water vapor (cf. §3.4). The experimental system was constrained by its use of electrical heaters, instead of heat exchangers, which could only raise the air temperature to an average maximum temperature of 134 °F. Moreover, the theoretical condensation stage was specifically designed to maximize the water extraction rate from the moist air. Condenser fluid side volumetric flow rate and operating temperature were set to insure that optimal conditions for film condensation were met. The numerical, thermodynamic and fluid mechanics analyses of the theoretical unit were also generally idealized and did not consider any system losses or sources of experimental error.

Finally, the calculated solar pond size for full a sized theoretical system was 0.71 acres. The solar pond size for the experimental system was calculated using the same ambient incident solar radiation conditions and solar pond efficiency as the theoretical analysis [5], 5.7 kWh/m^2/day and 12%, respectively. The maximum thermal heat load of the experimental unit was 105738 Btu/hr (Type II configuration, 12.0" CEM thickness and 1000 air CFM). The following equation was used to compute the solar pond size [56]:

$$\dot{Q} = \eta A I \tag{6.1}$$

where $\dot{Q}$ is the total heat load, η is the solar pond efficiency, A is the solar pond area and I is the incident solar radiation. Using the maximum heat load for the actual experimental process, a solar pond with a minimum area of 11700 ft^2, or 0.27 acre, would be required to successfully power the experimental HVAC-HDH unit investigated. This solar pond size is considerably smaller than the 0.75 acre solar pond once operated by The University of Texas at El Paso. An analogous theoretical unit would require a solar pond area of 13286 ft^2, or 0.31 acre, which was expected due to the higher target air temperatures of the heating stages.

6.5 Summary and concluding remarks

A comprehensive analysis and discussion of the experimental results was presented in this chapter. Data for Type I and II experiments were graphically and numerically examined. Except for two anomalies present in the same experimental configuration for both experiment types, graphical analysis of the experimental data demonstrates similar mathematical trends between Type I and II experiments. Numerical and thermodynamic analyses of the data indicate that the HVAC-HDH process investigated is highly thermally inefficient. This claim is substantiated by the system's low values of GOR. Regardless, the computed GORs compare favorably with values reported in the open literature for similar systems.

The chapter concludes by comparing a two-stage theoretical system, investigated in a previous feasibility study and the actual experimental unit. The comparison demonstrates that the theoretical system has higher production capabilities and GORs due to its positive linear water production trends as opposed to the asymptotic exponential behavior of the test unit. However, the experimental unit requires a smaller solar pond size of 0.27 acre when compared to the 0.31 acre pond required by an analogous two stage theoretical system. The solar pond size required is quite reasonable and feasible for construction, considering The University of Texas at El Paso successfully operated a 0.75 acre solar pond for several years [24].

This investigation was successful. The production capabilities and thermal efficiency of the studied desalination method are unable to compete with conventional desalination systems. However, the thermodynamic analysis indicates that this HVAC-HDH system can be successfully coupled with a salinity-gradient solar pond of a reasonable size. Implementation of this system on a larger scale is feasible only if coupled with a salinity-gradient solar pond capable of providing low grade thermal heat. Its modest production capabilities, technologically "light" design and modular structure make it an excellent candidate for implementation in arid, decentralized areas with water shortages and no technical

personnel. The unit would essentially be a "zero discharge" system, as discussed in Lu et al [24], since the salt recovered by the HDH desalination process could potentially be used for further expansion or maintenance of the coupled solar pond. The investigated HDH system also reveals a novel application of HVAC technology, water desalination, which certainly merits further research and development.

Chapter 7: Conclusions and Recommendations

This chapter reviews the conclusions reached as a result of the investigation and ensuing analysis. Recommendations for follow-up or alternative research for the experimental facility will also be discussed. Based on the results of this study the following conclusions are made:

1. The HVAC-HDH experimental system was effective in desalinating the laboratory feed-water used in the experiments. Laboratory tap water at The University of Texas at El Paso typically has a conductivity of 800 μS/cm [55]. Samples from the test unit's water production had an average conductivity of 19±2 μS/cm (20:1).
2. The experimental unit's performance and production capabilities were compared to an analogous, two-stage version of the theoretical unit. The analysis indicated that in comparison to the test unit, the theoretical system shows an average 26% *increase* in water production with each incremental setting of air CFM. This is due to its monotonically increasing linear trend for water production as opposed to the asymptotic exponential trend of the experimental unit. The average differences in water production between theoretical and experimental units were 9.10 lb_w/hr and 33.69 lb_w/hr for 1 and 2 stage configurations, respectively.
3. Energy consumption for the desalination process was elevated for the prototype HVAC-HDH unit. This was certainly expected as the theoretical unit was also a thermal energy intensive system. In terms of GOR, an analogous two-stage theoretical system exhibits average values of 1.06 and 2.51 for 1 and 2 stage configurations, respectively. The test unit has average GOR values of 0.39 and 0.49 for 1 and 2 stage configurations. The higher GOR values of the theoretical system are due to its higher water production. Regardless, both systems are highly inefficient when compared to conventional desalination processes. The advantage of the investigated HDH cycle is that all thermal processes can be driven by low-grade heat supplied by

a salinity gradient solar pond. A 0.27 acre solar pond is adequate for providing the thermal energy loads for the tested experimental unit. An analogous theoretical system would require a larger 0.31 acre solar pond due to its higher energy demands.

4. Corrugated cellulose evaporative media (CEM), i.e. CELdek® 7060-15, was effective when used in the HDH desalination process. Its commercial availability, ease of implementation and proven cooling effectiveness make it a good candidate for this type of desalination. Furthermore, the ample available wetted surface area of CELdek® not only makes it effective for air humidification but it also provides more surface area for the deposition of suspended solids from the brackish feed water. However, use of this type of evaporative media for this particular desalination process is not without its disadvantages. Excessive fouling of this media with cyclic use will result in diminished airflow, larger pressure drops, lower evaporative efficiency and overall poor humidification ability. Moreover, corrugated cellulose media does not offer a feasible removal method of deposited suspended solids. As a result, this evaporative media must be replaced once it has been rendered inefficient due to ongoing cyclic use. This can incur higher costs as desalination units are expanded to accommodate higher desalination capabilities. Recovery of salt from this evaporative media for potential reuse in salinity gradient solar ponds is possible but only if the evaporative media is essentially destroyed.

We arrive at certain recommendations that could potentially improve the operational capabilities of the experimental unit or direct future investigations with the unit in innovative directions. The following are recommendations based on observations, experiments and results of this research:

1. One of the primary problems throughout the experimental portion of the investigation was the lack of specialized measurement instrumentation. Of particular interest was the ability to accurately measure wet-bulb temperature or air humidity. Dedicated hygrometers at each location will allow for more accurate determination of the psychrometric state of the process air

permitting a better analysis of the desalination process and pilot plant operation and production capabilities.

2. The original prototype system employed cross flow heat exchangers to provide the heat loads needed for all of the constant ω air heating processes. Due to space and laboratory constraints, it was necessary to use electrical heaters to impart the thermal heat load on the process air. This limited the maximum dry bulb temperature that the air could reach during the heating process. If the air were heated to a higher dry bulb temperature, it could essentially allow the air to absorb a higher amount of water vapor; potentially improving the pilot plant's desalinating capacity.
3. Modification of the primary thermal loading components, as previously suggested, could potentially improve the overall thermal performance. Heating components responsible for providing thermal loads for air preheating are the primary consumers of energy. Use of cross flow heat exchangers will facilitate the use of waste heat for this end. Waste heat from the condensation process can be reused to preheat the air at the beginning of the HDH process. The amount of thermal energy needed to heat the air to the desired dry-bulb temperature would eventually be reduced. This modification could translate into energy savings improving the thermal efficiency of the process.
4. The number of heating and humidification components was limited due to research funding availability. However, the theoretical plant design in the feasibility analysis included five heating and humidification stages as opposed to only two implemented in the prototype unit. The experimental unit's modular design allows both easy access to components and system modification by either addition or removal of system components. Additional stages could potentially improve the production capability of the experimental unit. The effect of multiple heating stages on plant yield capacity can be further examined to determine if there is an optimal quantity of heating and evaporation stages for maximum water production.

5. Humidification chambers were designed in such a fashion that they could accommodate different types of evaporative media or humidification devices. As discussed previously, CEM has to be replaced once it has fouled to the extent where the evaporative efficiency is severely hindered. Furthermore, salt collection that results from deposition of the suspended solids during the evaporation process is essentially accomplished by destroying the CELdek® pads. However, different types of evaporative media can be designed and tested in the humidification chambers of the pilot plant. Evaporative media that facilitates the removal and collection of deposited solids by some practical method (e.g. vibration) can be designed and tested. Design and use of evaporative media that is more resistant to mineral fouling or implementation of fine mist generators for air humidification within the custom designed evaporators can be considered. As a result this prototype system can be used for interdisciplinary environmental and sustainability research encompassing materials science and mechanical engineering technology.
6. The experimental unit was constructed and tested inside a controlled laboratory setting. This facilitated environmental control allowing for uniform experimental conditions. However a pilot plant such as the one tested, or one potentially larger, could potentially be constructed and tested in an outdoor setting. This type of investigation would allow us to better understand pilot plant operation and production capabilities in its intended environment. Investigating the system in an outdoor setting will permit the evaluation of the system's durability and robustness. The test system will need to undergo certain modifications for proper operation in an outdoor environment (primarily instrumentation protection and secure sealing of the evaporator covers preventing their opening during system operation or high wind conditions).
7. Outdoor installation of an experimental unit also allows it to be coupled with a salinity-gradient solar pond. This investigation proved that a 0.27 acre solar pond can effectively provide the necessary thermal loads to drive the heating processes. The solar pond could also provide a

means to generate electricity needed for the operation of smaller equipment such as water pumps, instrumentation and perhaps power to the main centrifugal or cooling tower fan. Since the salinity gradient solar pond can provide the thermal energy required by the pilot plant, the system would essentially be a self-sustaining desalination unit that could be implemented in decentralized locations far removed from conventional municipal power grids.

The experimental desalination plant with its modular design, low technology components requiring minimal technical expertise, and modest production capabilities, is well suited for implementation in areas where both potable water and technical personnel are limited. The pilot plant studied has potential for optimization, expansion and for implementation of innovative technology. The interdisciplinary nature of the research can generate knowledge of broad impact in diverse engineering fields.

References

[1] Narayan, G. P., Sharqawy, M. H., Summers, E. K., Lienhard, J. H., Zubair, S. M., and Antar, M. A., 2010, "The potential of solar-driven humidification-dehumidification desalination for small-scale decentralized water production," Renewable & Sustainable Energy Reviews, 14(4), pp. 1187-1201.

[2] Qiblawey, H. M., and Banat, F., 2008, "Solar thermal desalination technologies," Desalination, 220(1-3), pp. 633-644.

[3] Fath, H. E. S., and Ghazy, A., 2002, "Solar desalination using humidification-dehumidification technology," Desalination, 142(2), pp. 119-133.

[4] Goosen, M. F. A., Sablani, S. S., Shayya, W. H., Paton, C., and Al-Hinai, H., 2000, "Thermodynamic and economic considerations in solar desalination," Desalination, 129(1), pp. 63-89.

[5] Cornejo, J. A., Enriquez, G and Love, N.D., 2003, "Report on the Desalination of Water through the Humidification and Dehumidification of Air with the use of HVAC Systems and Solar Pond Technology,"Undergraduate Thesis, The University of Texas at El Paso, El Paso, TX.

[6] Yuan, G. F., Zhang, L. X., and Zhang, H. F., 2005, "Experimental research of an integrative unit for air-conditioning and desalination," Desalination, 182(1-3), pp. 511-516.

[7] 2005, "Desalination - a snapshot," Filtration Industry Analyst, 2005(3), pp. 5-7.

[8] Delyannis, E., and Belessiotis, V., 2010, "Desalination The recent development path," Desalination, 264(3), pp. 206-213.

[9] Lattemann, S., and Hopner, T., 2008, "Environmental impact and impact assessment of seawater desalination," Desalination, 220(1-3), pp. 1-15.

[10] Bouchekima, B., Gros, B., Ouahes, R., and Diboun, M., 2001, "Brackish water desalination with heat recovery," Desalination, 138(1-3), pp. 147-155.

[11] Mathioulakis, E., Belessiotis, V., and Delyannis, E., 2007, "Desalination by using alternative energy: Review and state-of-the-art," Desalination, 203(1-3), pp. 346-365.

[12] Mezher, T., Fath, H., Abbas, Z., and Khaled, A., 2011, "Techno-economic assessment and environmental impacts of desalination technologies," Desalination, 266(1-3), pp. 263-273.

[13] Wade, N. M., 2001, "Distillation plant development and cost update," Desalination, 136(1-3), pp. 3-12.

[14] Abou Rayan, M., and Khaled, I., 2003, "Seawater desalination by reverse osmosis (case study)," Desalination, 153(1-3), pp. 245-251.

[15] Van der Bruggen, B., and Vandecasteele, C., 2002, "Distillation vs. membrane filtration: overview of process evolutions in seawater desalination," Desalination, 143(3), pp. 207-218.

[16] Ahmed, M., Arakel, A., Hoey, D., Thumarukudy, M. R., Goosen, M. F. A., Al-Haddabi, M., and Al-Belushi, A., 2003, "Feasibility of salt production from inland RO desalination plant reject brine: a case study," Desalination, 158(1-3), pp. 109-117.

[17] Ahmed, M., Shayya, W. H., Hoey, D., Mahendran, A., Morris, R., and Al-Handaly, J., 2000, "Use of evaporation ponds for brine disposal in desalination plants," Desalination, 130(2), pp. 155-168.

[18] Vedavyasan, C. V., 2001, "Combating brine disposal under various scenario," Desalination, 139(1-3), pp. 419-421.

[19] Al-Hallaj, S., Farid, M. M., and Tamimi, A. R., 1998, "Solar desalination with a humidification-dehumidification cycle: performance of the unit," Desalination, 120(3), pp. 273-280.

[20] Parekh, S., Farid, M. M., Selman, J. R., and Al-Hallaj, S., 2004, "Solar desalination with a humidification-dehumidification technique - a comprehensive technical review," Desalination, 160(2), pp. 167-186.

[21] Al-Sahali, M., and Ettouney, H., 2007, "Developments in thermal desalination processes: Design, energy, and costing aspects," Desalination, 214(1-3), pp. 227-240.

[22] Bourouni, K., Chaibi, M. T., and Tadrist, L., 2001, "Water desalination by humidification and dehumidification of air: state of the art," Desalination, 137(1-3), pp. 167-176.

[23] Narayan, G. P., Sharqawy, M. H., Lienhard, J. H., and Zubair, S. M., 2010, "Thermodynamic analysis of humidification dehumidification desalination cycles," Desalination and Water Treatment, 16(1-3), pp. 339-353.

[24] Lu, H. M., Walton, J. C., and Swift, A. H. P., 2001, "Desalination coupled with salinity-gradient solar ponds," Desalination, 136(1-3), pp. 13-23.

[25] Dai, Y. J., and Zhang, H. F., 2000, "Experimental investigation of a solar desalination unit with humidification and dehumidification," Desalination, 130(2), pp. 169-175.

[26] El-Agouz, S. A., 2010, "Desalination based on humidification-dehumidification by air bubbles passing through brackish water," Chemical Engineering Journal, 165(2), pp. 413-419.

[27] Kassim, M. A., Benhamou, B., and Harmand, S., 2011, "Effect of air humidity at the entrance on heat and mass transfers in a humidifier intended for a desalination system," Applied Thermal Engineering, 31(11-12), pp. 1906-1914.

[28] Yamali, C., and Solmus, I., 2008, "A solar desalination system using humidification-dehumidification process: experimental study and comparison with the theoretical results," Desalination, 220(1-3), pp. 538-551.

[29] Karagiannis, I. C., and Soldatos, P. G., 2008, "Water desalination cost literature: review and assessment," Desalination, 223(1-3), pp. 448-456.

[30] Al-Hallaj, S., Parekh, S., Farid, M. M., and Selman, J. R., 2006, "Solar desalination with humidification-dehumidification cycle: Review of economics," Desalination, 195(1-3), pp. 169-186.

[31] American Society of Heating, Refrigerating and Air Conditioning Engineers, 2009, ASHRAE Handbook: Fundamentals. Inch-Pound Ed., ASHRAE, Atlanta, Chap. 1-3.

[32] McQuiston, F. C., Parker, J.S. and Spitler, J.D., 2000, Heating, Ventilating and Air Conditioning Analysis and Design, John Wiley & Sons, New York, Chap. 3.

[33] Trane Company, 1996, Trane Air Conditioning Manual, The Trane Company, La Crosse, Chap IV.

[34] Watt, J. R. and Brown, W.K., 1997, Evaporative Air Conditioning Handbook, Fairmont Press, Lilburn, Chap. III,VII.

[35] Howell, R. H., Sauer Jr., H.J. and Coad, W.J., 2005, Principles of Heating Ventilating and Air Conditioning, ASHRAE, Atlanta, Chap. 2.

[36] Moran, M. J., Shapiro, H., 2000, Fundamentals of Engineering Thermodynamics, John Wiley & Sons, New York, Chap. 4.

[37] Van Wylen, G. J. and Sonntag, R.E., 1986, Fundamentals of Classical Thermodynamics, John Wiley & Sons, New York, Chap. 3, 5-7.

[38] 2011, "HD PsyChart Suite Professional 7.3 ™ ", Hands Down Software.

[39] 2012, "Coil Selection Program and Electronic Catalogue," USA Coil and Air.

[40] Taylor, J. R., 1997, An Introduction to Error Analysis, University Science Books, Sausalito, Chap. 3,7.

[41] "Common Water Measurements," http://ga.water.usgs.gov/edu/characteristics.html.

[42] 2004, "Electrical conductivity/salinity Fact Sheet, FS-3.1.3.0 (EC)," The Clean Water Team Guidance Compendium for Watershed Monitoring and Assessment, D. o. W. Q. California State Water Resources Control Board, ed.

[43] 2012, "Conductivity," http://water.epa.gov/type/rsl/monitoring/vms59.cfm.

[44] Lide, D. R., 2011, CRC Handbook of Chemistry and Physics, CRC Press, Boca Raton.

[45] Chafik, E., 2003, "A new type of seawater desalination plants using solar energy," Desalination, 156(1-3), pp. 333-348.

[46] Singh, D., and Sharma, S. K., 1989, "Performance Ratio, Area Economy and Economic Return for an Integrated Solar Energy Multi-Stage Flash Desalination Plant," Desalination, 73(1-3), pp. 191-195.

[47] Summers, L. J., 1995, "Desalination Processes and Performance," Lawrence Livermore National Laboratory.

[48] Mistry, K. H., Lienhard, J. H., and Zubair, S. M., 2010, "Effect of entropy generation on the performance of humidification-dehumidification desalination cycles," International Journal of Thermal Sciences, 49(9), pp. 1837-1847.

[49] Kline, S. J. and McClintock, F.A., 1953, "Describing Uncertainties in Single Sample Experiments," Mechanical Engineering, 75(1), pp. 3-8.

[50] Moffat, R. J., 1985, "Using Uncertainty Analysis in the Planning of an Experiment," Journal of Fluids Engineering, 107(2), pp. 173-178.

[51] Moffat, R. J., 1988, "Describing the uncertainties in experimental results," Experimental Thermal and Fluid Science, 1(1), pp. 3-17.

[52] Kline, S. J., 1985, "The Purposes of Uncertainty Analysis," Journal of Fluids Engineering, 107(2), pp. 153-160.

[53] Kline, S. J., 1985, "1983 Symposium on Uncertainty Analysis Closure," Journal of Fluids Engineering, 107(2), pp. 181-182.

[54] Munters, 2005, "CELdek 7060-15 Evaporative Cooling Pad," Munters Europe HumiCool Division, Sollentuna, Sweden.

[55] Tarquin, A. J., 2012, "Conductivity of UTEP lab water," Dowdy, J.A., Cornejo, J.A., The University of Texas at El Paso, Personal Communication, p. 1.

[56] Hull, J. R., Nielsen, C.E. and Golding. P., 1988, Salinity Gradient Solar Ponds, CRC Press, Boca Raton.

Appendix A: Concentration Fundamentals

This appendix reviews fundamental concepts useful for understanding several key psychrometric relationships. Fundamental relationships of mass and molar concentrations in addition to partial pressure equations will be reviewed.

A.1 Mass concentration relationships

Consider a unit control volume $\Delta\forall$ containing molecules from an arbitrary species, *i*, as illustrated in the following figure:

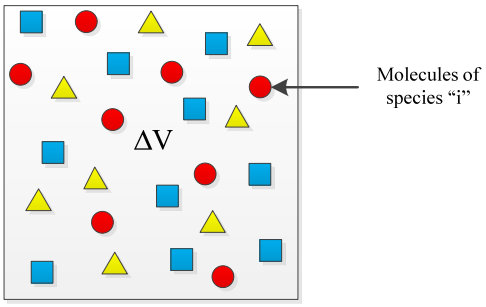

Figure A.1.1: Unit control volume containing different species.

Several useful relationships for describing the concentration of the particular species within its control volume will be developed. Let us define the number density, N_i, which is defined as the number of molecules of the species *i* found in the unit volume $\Delta\forall$, i.e.:

$$N_i \equiv \frac{molecules\ of\ i}{\Delta\forall} \tag{A.1}$$

If the total number of molecules in the unit volume is represented by N, the number fraction n_i is defined as follows:

$$n_i \equiv \frac{N_i}{N} \tag{A.2}$$

where:

$$N = \sum N_i \tag{A.3}$$

Another important term used for describing composition is the mass concentration, ρ_i, of a species. The mass concentration is defined as the partial density of a species within a specified volume. By definition, density is the ratio of mass to volume, or:

$$\rho \equiv [m][L]^{-3} \tag{A.4}$$

Therefore the mass concentration of species *i* equals the partial density of species *i* or:

$$\rho_i = \frac{m_i}{\cancel{V}} \tag{A.5}$$

where the total mass concentration is the total mass per unit volume, i.e. total density of the sample:

$$\rho_{total} = \rho = \sum \rho_i \tag{A.6}$$

Finally, the mass fraction of a species is defined as the ratio of partial to total density. In an analogous manner to the mass concentration, the following definition and relationship apply to the mass fraction:

$$\bar{m}_i \equiv \frac{\rho_i}{\rho} \tag{A.7}$$

$$m_{total} = m = \sum \bar{m}_i \tag{A.8}$$

$$\sum \bar{m}_i = 1 \tag{A.9}$$

A.2 Molar concentration relationships

Molar concentration relationships that are analogous to those for mass concentration will be reviewed. These relationships are directly related to several psychrometric parameters and physical properties of a mixture (e.g. partial pressure). We begin with the basic relationship of molar concentration c_i, which by definition is the number of moles of a species *i* per unit volume $\Delta\cancel{V}$:

$$c_i \equiv \frac{mol\ of\ i}{\Delta \forall} \tag{A.10}$$

Now if M_i is the molecular weight of this arbitrary species, the molar concentration can also be expressed as:

$$c_i = \frac{\rho_i}{M_i} \tag{A.11}$$

where the total molar concentration *c* is defined as:

$$c = \sum c_i \tag{A.12}$$

The mole fraction x_i, is defined in a similar fashion to its counterpart the mass fraction; i.e. the ratio of the molar concentration of *i* to the total concentration:

$$x_i \equiv \frac{c_i}{c} \tag{A.13}$$

Analogous to (A.9):

$$\sum x_i = 1 \tag{A.14}$$

Some useful relationships using the previously reviewed definitions of mass and molar concentration will now be developed. For instance, the mean molecular weight $\overline{M}$ of a mixture or solution is expressed as:

$$\overline{M} = \frac{\rho}{c} = \sum x_i M_i \tag{A.15}$$

We arrive at this key relationship by realizing that this is a sum of all the mass concentrations, i.e. the total density, divided by the total molar concentration of the mixture or solution. From (A.11) we express the partial density of the species *i* as:

$$\rho_i = c_i M_i \tag{A.16}$$

by (A.6) we arrive at:

$$\rho = \sum \rho_i = \sum c_i M_i \tag{A.17}$$

However if:

$$\overline{M} = \frac{\rho}{c} = \frac{\sum \rho_i}{c}$$

and

$$\frac{\sum \rho_i}{c} = \frac{1}{c} \sum c_i M_i$$

we proceed to:

$$\frac{1}{c} \sum c_i M_i = \sum \frac{c_i}{c} M_i$$

recalling the definition of mole fraction from (A.13) we arrive at equation (A.15):

$$\overline{M} = \sum x_i M_i \tag{A.15}$$

Another term of interest is the inverse of the mean molecular weight $\frac{1}{\overline{M}}$. From equation (A.15):

$$\frac{1}{\overline{M}} = \frac{c}{\rho}$$

Referring to (A.11) and (A.12):

$$c = \sum c_i = \sum \frac{\rho_i}{M_i}$$

thus:

$$\frac{1}{\overline{M}} = \frac{1}{\rho} \sum \frac{\rho_i}{M_i}$$

which can be rewritten as:

$$\frac{1}{\rho} \sum \frac{\rho_i}{M_i} = \sum \frac{\rho_i}{\rho} \frac{1}{M_i}$$

Using definition (A.7) we can state:

$$\frac{1}{\overline{M}} = \sum \frac{m_i}{M_i} \tag{A.18}$$

A.3 Partial pressure relationships

There are some curious relationships that exist between concentrations and pressure that are quite useful for calculations and for psychrometric analysis. Let us examine partial pressure and total pressure. According to Dalton's Law of Partial Pressures for a multicomponent system, the total pressure is the sum of all partial pressures exerted by the system constituents:

$$P_{total} = P = \sum P_i \tag{A.19}$$

The ideal gas equation of state is applicable assuming the components behave as perfect gases. The ideal gas law on a molar basis is expressed as:

$$PV = n\overline{R}T \tag{A.20}$$

Now the partial pressure of a species *i* can be defined by the following representation of (A.20):

$$P_i = \rho_i R_i T \tag{A.21}$$

where the gas constant for a specific component is defined by dividing the Universal Gas Constant $\overline{R}$ [12] by the molecular weight, M_i, of the component:

$$R_i = \frac{\overline{R}}{M_i} \tag{A.22}$$

The ratio of partial pressure to total pressure will be defined by using (A.21) and (A.22):

$$\frac{P_i}{P} = \left(\rho_i \frac{\overline{R}}{M_i} T\right)\left(\frac{1}{P}\right) = \frac{\rho_i}{M_i}\overline{R}T\left(\frac{1}{P}\right)$$

Recalling the definition of molar concentration (A.11):

$$\frac{P_i}{P} = c_i \overline{R}T\left(\frac{1}{P}\right)$$

[12] $\overline{R}$ =1545.32 (ft lb_f)·(lb_{mol} °R)$^{-1}$; cf. [31]

Using the definition of mole fraction (A.13) the molar concentration of a component *i* is expressed as:

$$c_i = x_i c \tag{A.23}$$

leading to the following expression:

$$\frac{P_i}{P} = x_i c \bar{R} T \left(\frac{1}{P} \right) \tag{A.24}$$

With (A.20) the pressure P can be expressed as follows:

$$P = \frac{n \bar{R} T}{V} = c \bar{R} T \tag{A.25}$$

Substitution of (A.25) into (A.24) we arrive at the following important relationship between pressure and mole fraction:

$$\frac{P_i}{P} = x_i \tag{A.26}$$

Appendix B: Psychrometric Process Charts: Type I & II Experiments

This appendix contains psychrometric process charts of Type I and II experiments for a 12.0" CEM thickness configuration. A psychrometric process chart was generated for each experiment conducted. However, the 12.0" CEM experimental configuration was selected since it more clearly represents the HDH desalination cycle examined in this investigation. All psychometric charts were generated with HD PsyChart Suite Professional 7.3™ [38], a specialized HVAC software package. This software was used to calculate head loads, computationally verify water production for each experiment and facilitate the graphic psychrometric analysis of each conducted experiment.

B.1 Type I Experiments

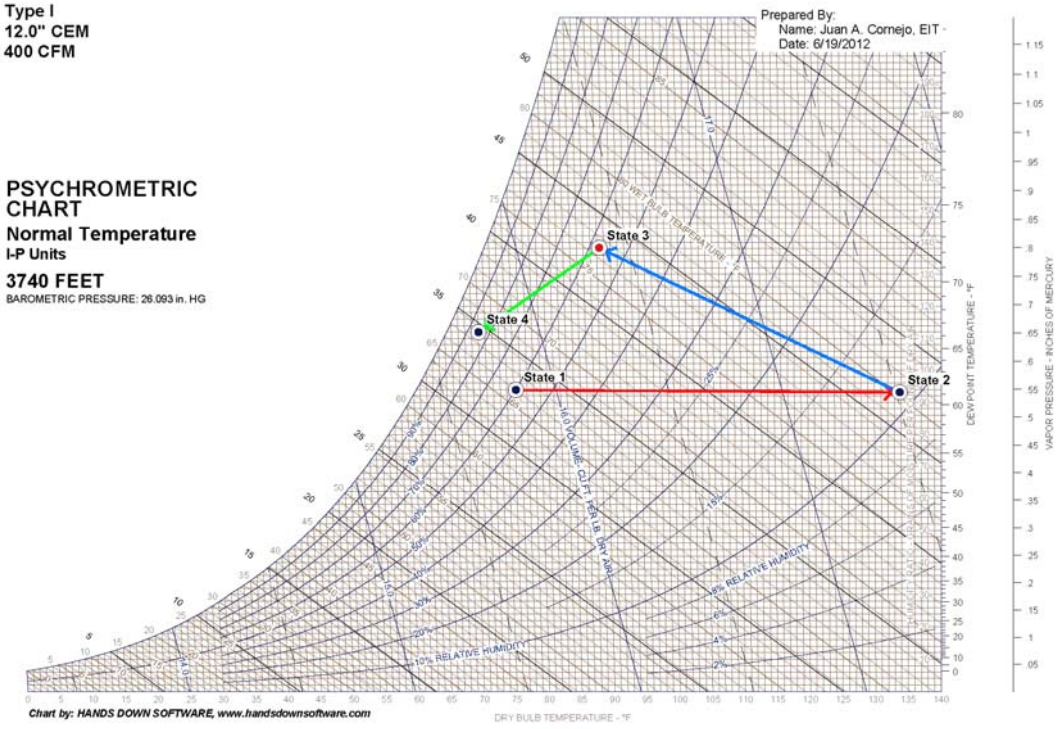

Figure B.1.1: Type I, 12.0" CEM psychrometric chart: 400 CFM

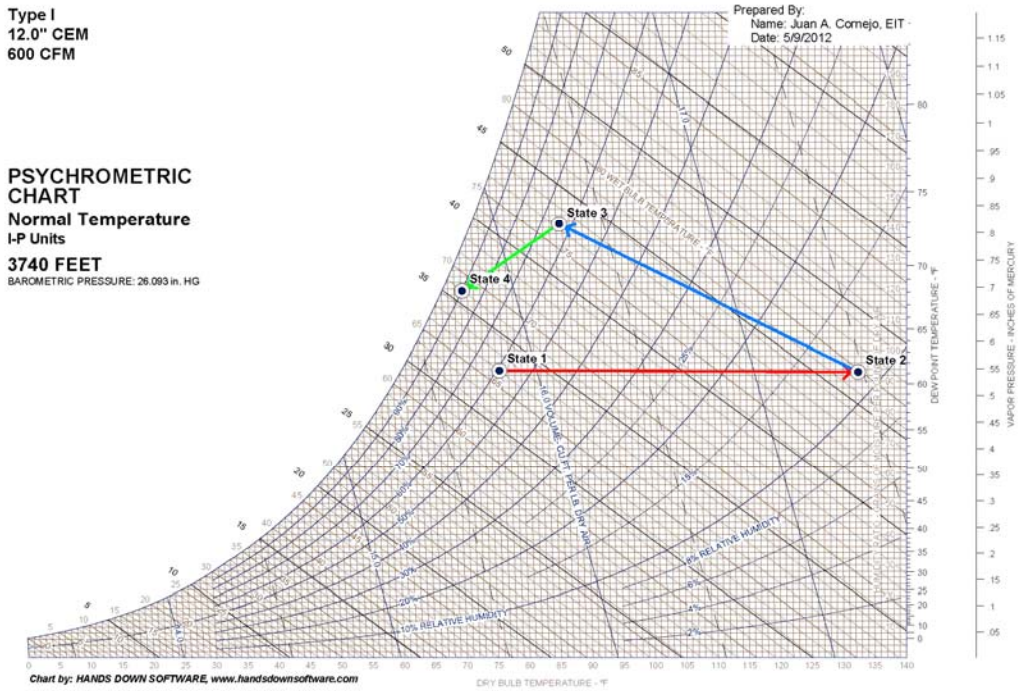

Figure B.1.2: Type I, 12.0” CEM psychrometric chart: 600 CFM

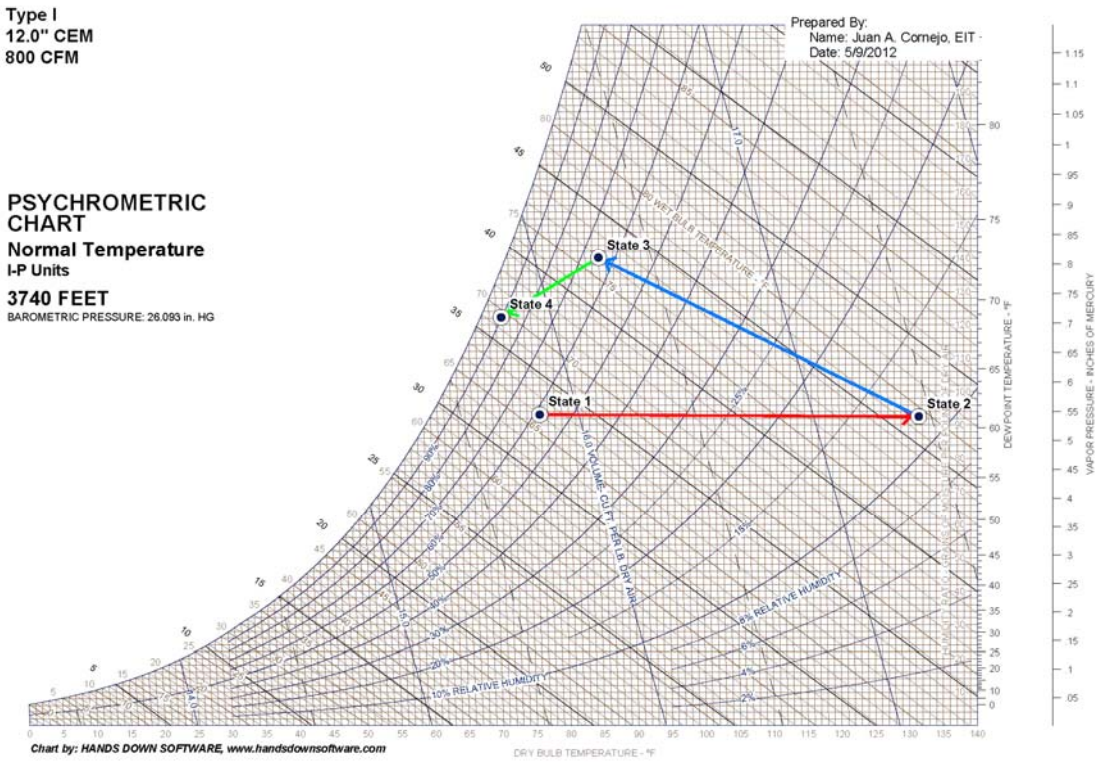

Figure B.1.3: Type I, 12.0” CEM psychrometric chart: 800 CFM

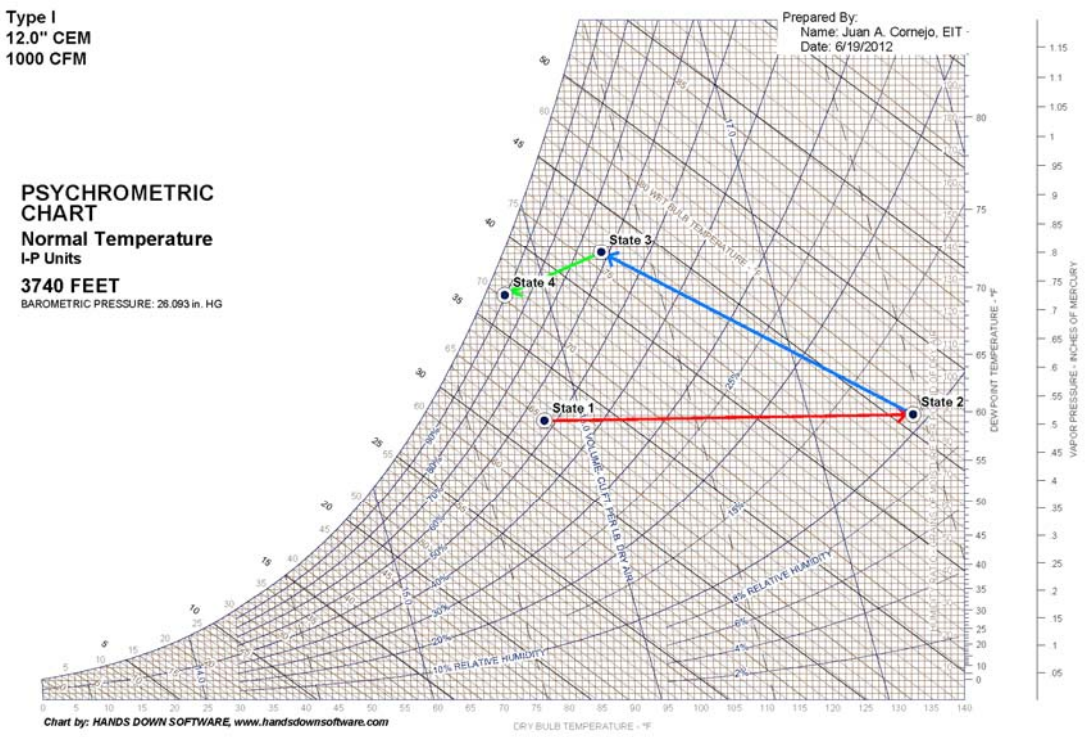

Figure B.1.4: Type I, 12.0” CEM psychrometric chart: 1000 CFM

THE REST OF THIS PAGE LEFT INTENTIONALLY BLANK

B.2 Type II Experiments

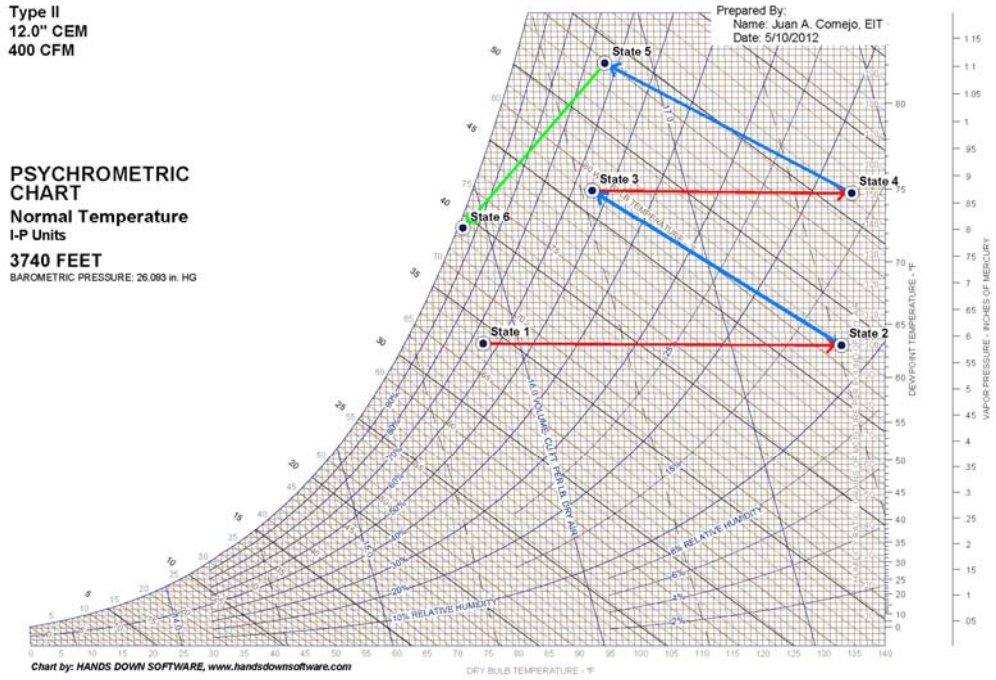

Figure B.2.1: Type II, 12.0” CEM psychrometric chart: 400 CFM

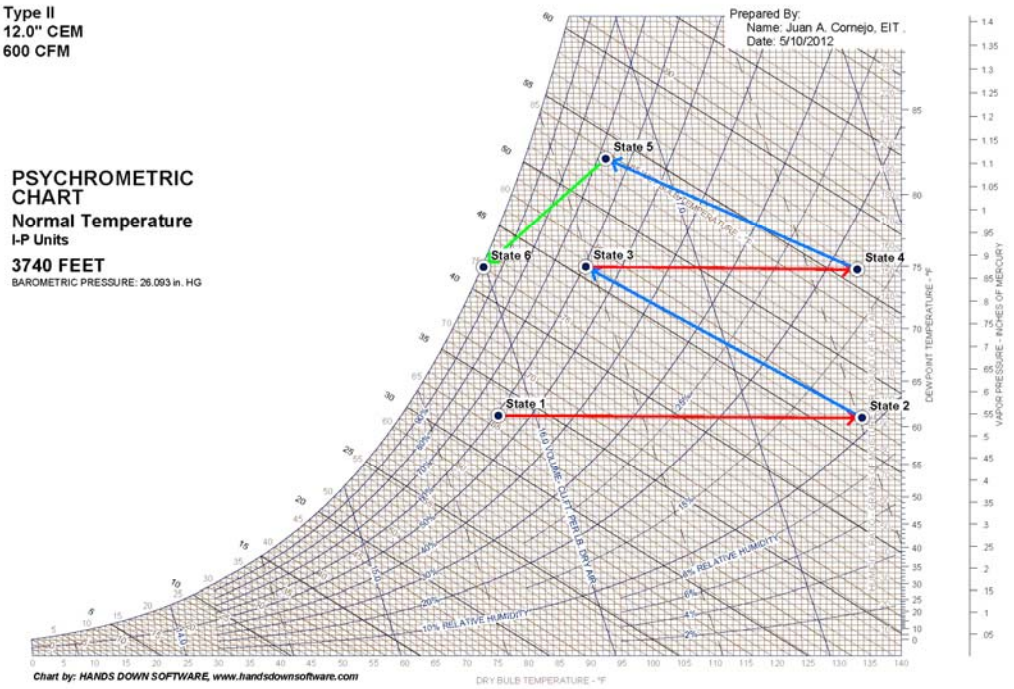

Figure B.2.2: Type II, 12.0” CEM psychrometric chart: 600 CFM

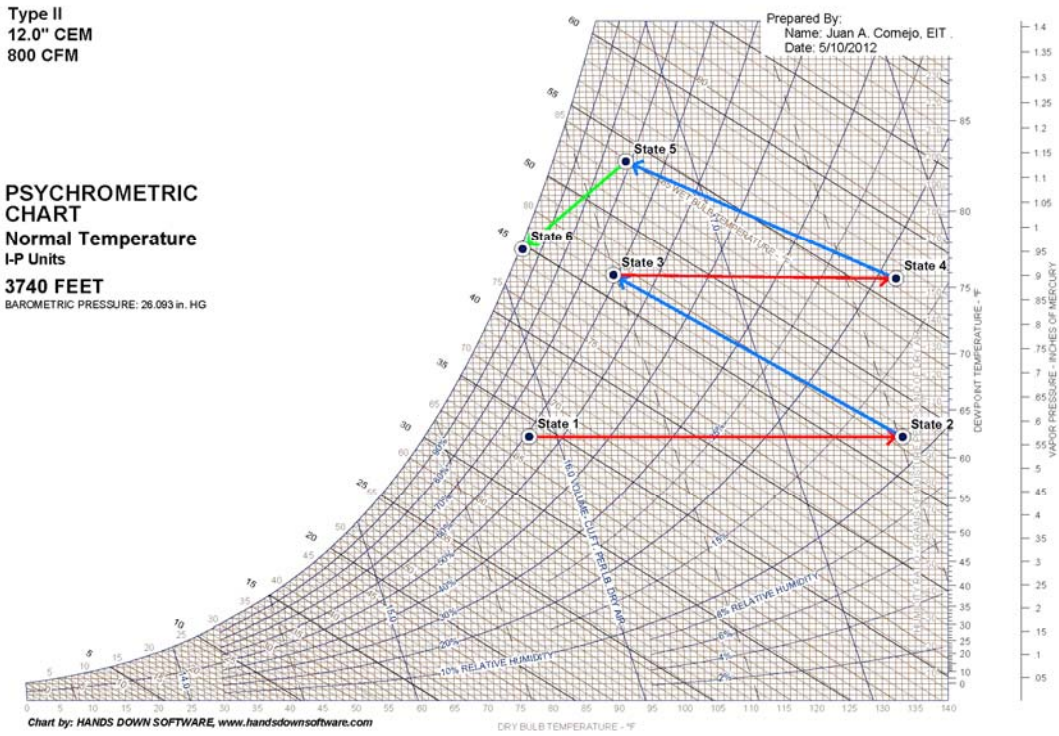

Figure B.2.3: Type II, 12.0" CEM psychrometric chart: 800 CFM

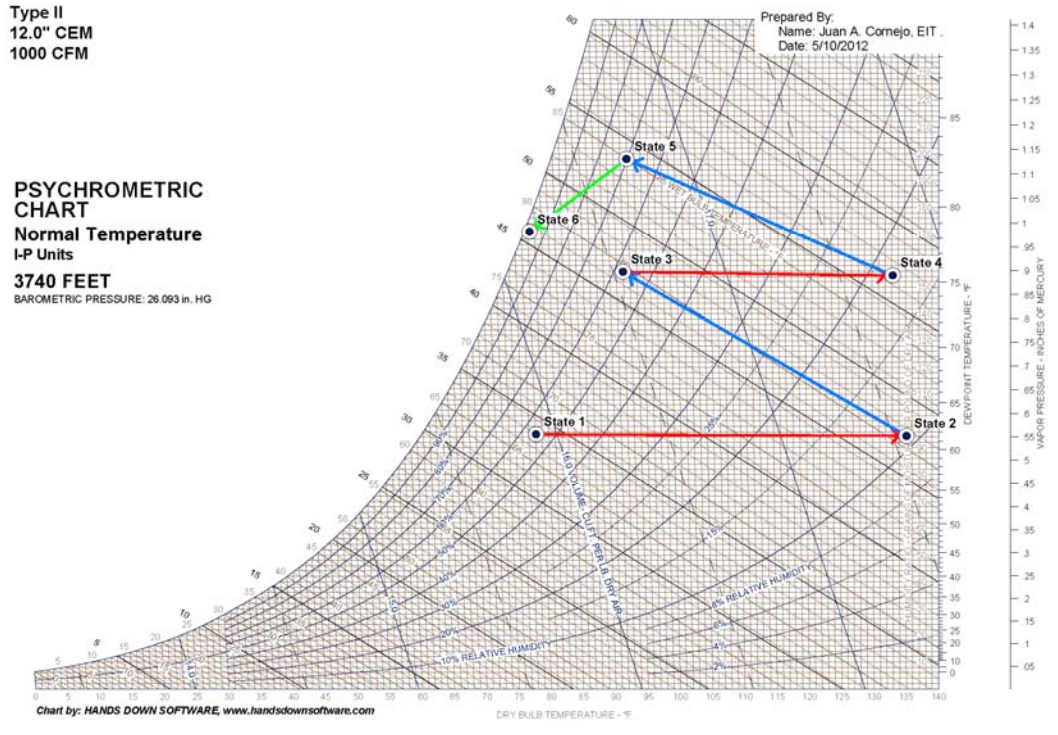

Figure B.2.4: Type II, 12.0" CEM psychrometric chart: 1000 CFM

Vita

Juan Antonio Cornejo was born on April 5, 1979 in Ciudad Juarez, Chihuahua, Mexico. He was raised in El Paso, Texas and became a naturalized United States citizen in 1996. Cornejo graduated from Ysleta High School, El Paso, Texas in 1997. In 2003 he graduated from The University of Texas at El Paso with a Bachelor of Science degree in mechanical engineering. He began graduate studies at The University of Texas at El Paso earning a Master of Science in Mechanical Engineering degree in 2012. During his tenure at UTEP he gained instructional experience serving as a teaching assistant for a variety of lecture and laboratory courses in the mechanical engineering department. In 2008, he moved to College Station, Texas to pursue a doctoral degree in the same discipline at Texas A&M University while completing his master's thesis in tandem.

Cornejo currently conducts research in the area of frost formation on surfaces as the topic of his doctoral research. He has also conducted research in HVAC systems and water desalination techniques. In 2006 he served as an engineering consultant and head plant engineer at Freus Inc. in Vinton, Texas. He has taught classes in thermodynamics, fluid mechanics, heat transfer, compressible flow and numerical methods. His research interests include heat transfer, thermodynamics, interfacial and phase change phenomena and applied mathematics. He is a member of the American Society of Mechanical Engineers (ASME), the American Society of Heating, Refrigerating and Air-Conditioning Engineers (ASHRAE) and the American Physical Society (APS).

He can be reached via Dr. Jack Dowdy, professor at The University of Texas at El Paso, Mechanical Engineering Dept., El Paso, TX 79968.

The typist for this thesis was Juan Antonio Cornejo.